INFORMATION TO USERS

This manuscript has been reproduced from the microfilm master. UMI films the text directly from the original or copy submitted. Thus, some thesis and dissertation copies are in typewriter face, while others may be from any type of computer printer.

The quality of this reproduction is dependent upon the quality of the copy submitted. Broken or indistinct print, colored or poor quality illustrations and photographs, print bleedthrough, substandard margins, and improper alignment can adversely affect reproduction.

In the unlikely event that the author did not send UMI a complete manuscript and there are missing pages, these will be noted. Also, if unauthorized copyright material had to be removed, a note will indicate the deletion.

Oversize materials (e.g., maps, drawings, charts) are reproduced by sectioning the original, beginning at the upper left-hand corner and continuing from left to right in equal sections with small overlaps.

Photographs included in the original manuscript have been reproduced xerographically in this copy. Higher quality 6" x 9" black and white photographic prints are available for any photographs or illustrations appearing in this copy for an additional charge. Contact UMI directly to order.
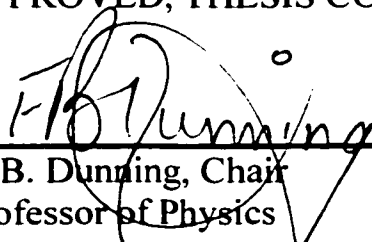
RICE UNIVERSITY

DISSOCIATIVE AND NON-DISSOCIATIVE ELECTRON
ATTACHMENT PROCESSES STUDIED USING RYDBERG ATOM
TECHNIQUES

by

CARLA D. FINCH

A THESIS SUBMITTED IN PARTIAL FULFILLMENT OF THE
REQUIREMENTS FOR THE DEGREE
DOCTOR OF PHILOSOPHY

APPROVED, THESIS COMMITTEE

F. B. Dunning, Chair
Professor of Physics

G. K. Walters
Professor of Physics

P. R. Brooks
Professor of Chemistry

Houston, TX
November, 1999

ABSTRACT

Dissociative and Non-dissociative Electron Attachment Processes Studied

Using Rydberg Atom Techniques

by

Carla D. Finch

Dissociative and non-dissociative electron attachment processes are investigated via electron transfer in collisions between velocity selected Rydberg atoms and target molecules. Measurements of the velocity distribution of the reaction products and of the decay of product negative ions during passage to the detector provide information about the energetics of the interactions and about the lifetime of the intermediate negative ion formed. Collisions with $CBrCl_3$ result in a dissociative process producing Br^- and Cl^- as products. Br^- production occurs through two reaction channels. The intermediate negative ion dissociates immediately in one channel, but the second channel involves a long-lived intermediate having a lifetime of ~ 5 ps. A single reaction channel produces Cl^-, but it is uncertain if the process is immediate or if it occurs after a few vibrational periods of the intermediate ion. Non-dissociative electron attachment occurs with C_7F_{14} and with C_6F_6. Collisions with C_7F_{14} lead to the production of free electrons and of long-lived ($\tau > 100$ μs) $C_7F_{14}^-$ ions. The free electrons, which result from autodetachment, are all created within a very short time period ($\tau \lesssim 5$ ps) following initial electron capture. Collisions with C_6F_6 result in the formation of $C_6F_6^{-*}$ ions that have a broad range of lifetimes against autodetachment. Data analysis and model calculations are discussed in addition to possible theoretical models explaining the results. Future experimental studies are also proposed.

Acknowledgements

Every worthwhile endeavor supplied by life is riddled with obstacles. As with many physical obstacles, the challenges encountered on the path leading to a Ph.D. are insurmountable without the help and support of a cohesive team. A group of specialists working together can accomplish goals that no individual could begin to achieve. I would like to take this opportunity to thank the group of specialists that accompanied me on this adventure. My research colleagues who are all travelling similar paths deserve recognition for the daily intellectual and emotional support that they provide to each other. Shannon and Bridget, I thank you both specifically for the endless brainstorming sessions you endured with me in the process of solving or, perhaps, creating experimental problems. Priya, I wish you the best of luck in controlling the gremlins. You have been an integral part of research progress. Thank you for the countless hours of data taking, problem solving, brainstorming, and design help, but most of all thank you for your friendship. I also owe a great deal to my advisor, Barry Dunning, for allowing me to learn from my own mistakes, while helping me to progress with the research. The remaining members of my team have specialized in emotional support and have been an essential part of my success. Chet Farmer, my love, thank you for enduring the pessimistic outlook of a graduate student and for filling my life with a happiness I would have never believed possible. Finally, and most importantly, I must thank my family. I owe this degree to them and to them alone. They provided me with opportunities by making sacrifices. They taught me to value myself and always to do my best. This achievement is founded on their love, support, and encouragement. Mom, Dad, Joe, thank you for believing in me.

Table of Contents

Chapter 1
Introduction

1.1 Electron Attachment Processes

Electron attachment processes have evoked much interest over the last several years. Molecules which attach electrons are important in atmospheric studies of ozone[1], in biological studies involving toxicity[2,3] and photosynthesis[4], in development of plasma discharges and gas lasers[5], and in environmental impact studies[6], to name a few. Most electron attachment processes involve a Negative Ion Resonance State (NIRS) in which the incident electron attaches to the neutral target molecule for times greater than that required to travel through the molecule. Such resonances are considered non-stationary states of the electron-molecule system and will decay by electron emission after some characteristic lifetime.

A resonance occurs when the incident electron becomes trapped in a potential well created by the interaction of the electron and the neutral target molecule. Figure 1.1 illustrates the potentials present as the electron approaches the molecule. The effective potential (V_{eff}) shown arises from the Coulombic attraction (V_a) between the electron and the target, which becomes polarized as the electron approaches, and from the centrifugal repulsion (V_r) due to the relative motion of the two bodies. V_r is proportional to $\frac{\ell(\ell+1)}{2r}$ where ℓ is the angular momentum of the target and r is the electron-molecule separation. V_{eff} forms a potential well-barrier combination. Negative energy states in the well are considered bound states of the molecule, but the existence of the barrier allows unbound, positive

(a)

V_repulsive

E_b

|R⟩

V_effective

V_attractive

ENERGY

RADIAL DISTANCE OF INCIDENT ELECTRON ρ
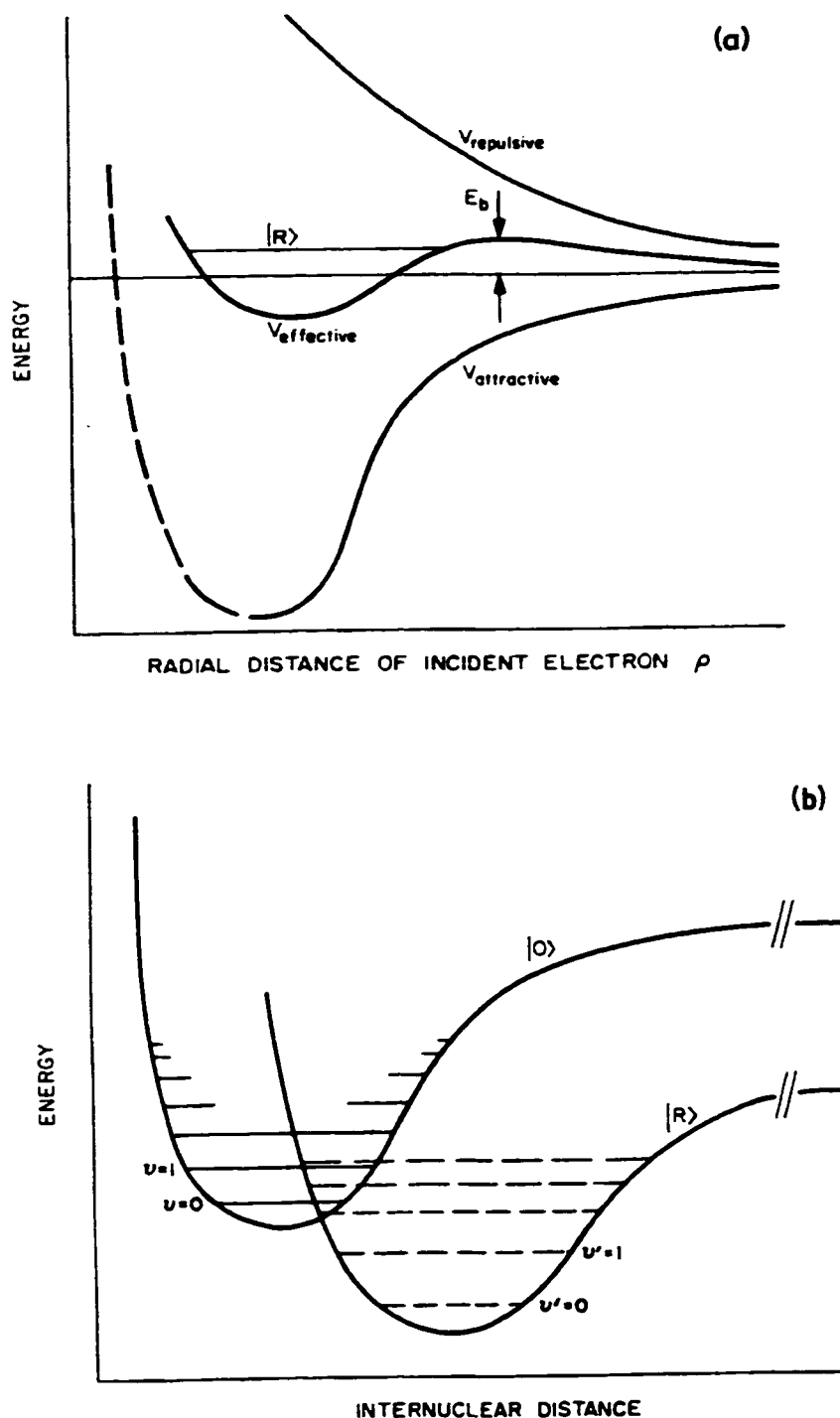
(b)

|0⟩

|R⟩

ENERGY

v=1
v=0

v'=1
v'=0

INTERNUCLEAR DISTANCE

Figure 1.1 Schematic illustration of (a) shape and (b) nuclear-excited Feshbach resonances. The symbols |0⟩ and |R⟩ designate, respectively, the electronic ground state of the neutral molecule and the NIRS.

energy states to exist also. Resonance occurs when the incident electron is trapped in a positive energy state from which it can escape by tunneling through the potential barrier.

NIRSs can be classified into four types: shape resonances, core-excited shape resonances, nuclear-excited Feshbach resonances, and electron-excited Feshbach resonances. Essentially, the origin of the potential well that traps the electron distinguishes the four types. Shape resonances result directly from the interaction of the incident electron and the target molecule, as illustrated in figure 1.1a. In a simple shape resonance, the effective potential arises from the attractive interaction between the electron and the ground state of the target molecule. Core-excited shape resonances, on the other hand, involve the attractive interaction between the electron and an excited electronic state of the target molecule. Energetically, shape resonances usually lie above the potential energy curve of the neutral molecule (parent state), as seen in figure 1.1a. These NIRSs preferentially decay through autodetachment, in which the electron is ejected, with a lifetime in the range $\sim 10^{-15}$ to $\geq 10^{-10}$ s. If energetically possible, dissociative attachment, in which the intermediate negative ion dissociates into a product ion and a neutral particle, can also occur.

Feshbach resonances involve the coupling of the kinetic energy of the captured electron to the molecular vibrations of the target. If the target molecule is in its ground electronic state the resonance is a nuclear-excited Feshbach resonance, shown schematically in figure 1.1b; an electronically excited target results in an electron-excited Feshbach resonance. The NIRSs initially lie in a vibrational level at or above the lowest vibrational level of the parent state. Decay into the parent state can, therefore, occur through

autoionization or autodissociation, but the characteristic lifetimes of these states are typically long, often $\geq 10^{-6}$ s. NIRSs that exist for very long lifetimes can stabilize to form negative ions. (Autoionization is a two step process in which the captured electron is ejected leaving a highly excited neutral state, which subsequently ejects another electron to return to the ground state energy level. Autodissociation also occurs as a two step process, but after the captured electron is ejected, the highly excited neutral dissociates into positive and negative particles to reach the parent state energy level.) [7,8]

Not all electron attachment processes involve NIRSs. Another class of negative ions exists in which the electron is captured via a three-body process. The electron is attracted to the nonisotropic charge distribution in the neutral target molecule. A third body carries away the excess kinetic energy, thereby allowing the electron to remain bound. For target molecules with large dipole (≥ 2 Debye) or quadrupole moments the negatively charged electron can be "trapped" in an orbit about the positively charged end of the molecule. Another possibility for target molecules with a high polarizability is that the electron will be attracted to its own image charge. In this case, the target molecule becomes polarized as the negatively charged electron approaches, and subsequently the electron remains loosely bound to the induced dipole. These bizarre species of negative ions — dipole-bound, quadrupole-bound, image charge-bound — share similar properties. In each species, the electron is loosely bound in a diffuse orbital about one end of the molecule. The negative ion, therefore, can easily return to the neutral parent state through collisional or field-induced ionization.

Low-energy electron attachment processes are studied using several different experimental approaches. Quantities of interest in these studies include the total electron attachment cross sections, reaction rate constants, final energy and angular distributions of the product ions, and lifetimes of the excited intermediate ions. In order to fully understand the interaction between the electron and the target molecule it is important to be able to control or to measure the initial and final states of the reactants and the products. The most direct approaches use a source of free electrons to collide with the neutral target molecules. This can be accomplished, for example, either in a crossed-beam orientation or using the Flowing Afterglow-Langmuir Probe (FALP) technique.

Crossed-beam experiments involve generating collimated beams of electrons and target molecules and intersecting them at a well-defined angle under low ambient pressure conditions. The collision region is confined by the intersection of the beams, and the reactions occur as single, binary collisions at a well-known center-of-mass energy, determined by the energy of the two beams. The total electron attachment cross-section is determined by observing either the decrease in intensity of the reactant beams or the number of reaction products. Reaction rate constants can then be determined from the cross sections. Further, changing the interaction angle and observing the distribution of the products as a function of angle provides information about the dynamics of the interactions. A disadvantage of crossed-beam techniques is that the accuracy of determining rate constants at low energies is quite poor. Generating a beam of electrons at energies much less than 1 eV with high precision is difficult at best. Electron monochromators have greatly improved the energy resolution of low-energy

electron beams. However, problems associated with space-charge effects still exist and limit the current density obtainable in the electron beam.

It is possible to use a merged beam technique to compensate for the low-energy imprecision of the crossed-beam method. In a merged-beam experiment, the electron beam runs collinear with the beam of target molecules so the center-of-mass energy of the system is governed by the difference between the velocities of the two beams. This allows much higher energy beams to be used but gives rise to a number of other difficulties. The degree of collinearity of the beams becomes an important experimental variable, which is difficult to measure. Further, the merged-beam technique does nothing to correct for other problems, like noise created by interaction of the beams with the background gas. The collisional spreading due to interaction with the background can enhance the space-charge effects of the electron beam on the target beam. Questions about the exact internal energy states of the reactants also remain unanswered.[9, 10]

The FALP technique differs from beam experiments in that, instead of a single collision occurring at one energy, there are multiple collisions with a spread of interaction energies due to a Maxwell-Boltzman distribution of electron velocities at the temperature of a buffer gas. An ensemble of electrons with a known number density is created in a fast-flowing buffer gas, which has a number density much greater than that of the electrons. During transport down a flow tube, multiple collisions between the electrons and the buffer gas randomize the electron velocities and thermalize the mean electron energies to those of the buffer gas at a known temperature. The target molecules are introduced with a specific, controlled number density that is much less than the number density of the buffer gas. The Langmuir

probe measures the electron, anion, and cation number densities along the axis of the flow tube to a spatial accuracy of ~1 mm. The reaction rate can then be directly obtained by observing the spatial rate of change in electron number density as a function of the target molecule density.

The FALP process requires great care to avoid the possible loss of electrons through spurious reaction channels. Control of the number densities of the buffer gas, the electrons, and the attaching molecules minimizes this loss but does not eliminate it. The FALP technique does incorporate the ability to study electron attachment at a range of energies by preheating or precooling the buffer gas. However, regardless of the temperature, the electrons have a spread of energies concordant with a Maxwell-Boltzman distribution.[11]

A less direct approach to studying electron attachment reactions utilizes atoms in high-lying Rydberg states as a source of essentially-free electrons. Typically, the atoms are photoexcited into a high principal quantum state and allowed to interact with the target molecules. The target molecule views the highly excited atom as two independent scatterers, the excited electron and the core ion, around which the electron orbits. The binary interaction between the target molecule and the Rydberg electron is the reaction of interest.

Studies using highly excited atoms provide several advantages over free-electron techniques. Extremely low energy electrons, from a few millivolts down to microvolts, can be produced with high precision, since the electron energy is equivalent to its binding energy on the atom, which can be adjusted by changing the principal quantum number of the atom. The velocity of the electron in its orbit about the atom is high compared to the

relative velocity of the atom and the target molecule at thermal temperatures and, thus, the energy of the electron dominates the interaction. In addition, the core ion can act as a probe of the dynamics of the electron-target molecule interaction. Rydberg atom experiments operate on a single collision basis, and the use of time-of-flight mass spectrometry provides information about the initial (final) states of the reactants (products). Absolute rate constants are determined directly from the measurements, and information about the lifetime of the intermediate product ions and the reaction energetics is obtained.

Though indirect, the Rydberg atom collision technique proves more powerful than free-electron experiments for studying thermal-energy or subthermal-energy electron attachment processes. The advantage of precisely controlling the electron energy, in conjunction with, the ability to know more accurately the states of the particles involved provides a deeper insight into the nature of the reactions studied. The specifics of the experiments including the apparatus, Monte Carlo simulations, and results will be discussed in detail throughout this work.

1.2 Rydberg Atom Properties

Neutral atoms in high-lying Rydberg states, henceforward referred to as Rydberg atoms, provide a novel source of essentially-free electrons for studying attachment processes. Rydberg atoms are formed by exciting the outermost electron of an atom, usually an alkali atom, into a high-lying energy state with principal quantum numbers in the range $14 \lesssim n \lesssim 55$, for the current studies. Rydberg atoms have many unusual properties. Table 1.1

lists a number of basic atomic parameters, along with their dependence on principal quantum number and typical values for a low-n Rydberg atom with n = 14 and a high-n Rydberg atom with n = 55.

TABLE 1.1

Property	n-dependence	n = 1	n = 14	n = 55
Mean radius	$n^2 a_0$	$5.3 \cdot 10^{-9}$ cm	10 nm	160 nm
Binding Energy	R/n^2	13.6 eV	69 meV	4 meV
Orbital period of electron	$\tau_1 n^3$	$1.5 \cdot 10^{-16}$ s	0.41 ps	25 ps
Radiative lifetime for $\ell = 1$	$\tau_0 n^3$	1 ns	2.7 μs	0.17 ms

The large size of the Rydberg atom, as described by the mean radius in table 1.1, indicates a large separation between the excited electron and the core ion (nucleus and remaining electrons). The range of interaction between an electron and a neutral molecule is typically much smaller than the average separation between the electron and the core ion of a Rydberg atom, even at low n. This suggests that, during a collision with a target molecule, the Rydberg core and the electron act as independent scatterers. Such behavior forms the basis of the nearly-free electron model, which suggests that the target molecule sees the Rydberg electron as, essentially, a low-

energy, free electron. The time-averaged kinetic energy of the nearly-free electron corresponds to its binding energy, also shown in table 1.1.
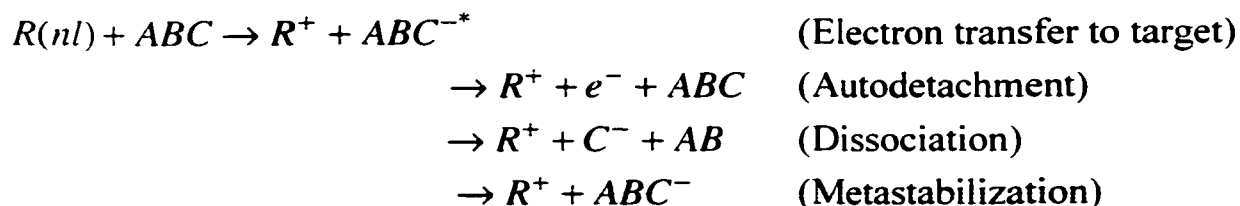
While the radius of the atom scales as n^2, the binding energy of the excited electron scales as n^{-2}. Thus, as the principal quantum number increases the atoms become physically quite large and have a very weakly bound electron. Because of this, Rydberg atoms are easily perturbed in thermal energy collisions with neutral target molecules, resulting in either collisional population of other n,ℓ states (state changing) or ionization. If the neutral target molecules have a high electron affinity, collisions can result in electron attachment. Further, because of their low binding energy the existence of very weak external electric fields may be sufficient to perturb, if not ionize, high-n Rydberg atoms. Though the atoms seem so fragile, they are remarkably stable against radiative decay. For an $\ell = 1$ Rydberg atom, the radiative lifetime scales as n^3, which implies that high-n Rydberg atoms can live for tens of microseconds or even milliseconds.

Because of their unusual physical properties, Rydberg atoms are extraordinarily useful in collision studies. As noted previously, thermal energy collisions with neutral molecules can result in direct collisional ionization or state changing of the Rydberg atom.

$$R(nl) + ABC \rightarrow R^+ + e^- + ABC \qquad \text{(Direct collisional ionization)}$$
$$\rightarrow R(n'l') + ABC \qquad \text{(State changing)}$$

In collisions with electron-attaching targets electron transfer to the target can also occur forming an excited intermediate ion that subsequently either autodetaches the electron, dissociates into a stable ion and a neutral

molecule, or is temporarily stabilized, having a lifetime long enough to be detected as a product. These processes are represented by the following equations:

$$R(nl) + ABC \rightarrow R^+ + ABC^{-*} \qquad \text{(Electron transfer to target)}$$
$$\rightarrow R^+ + e^- + ABC \qquad \text{(Autodetachment)}$$
$$\rightarrow R^+ + C^- + AB \qquad \text{(Dissociation)}$$
$$\rightarrow R^+ + ABC^- \qquad \text{(Metastabilization)}$$

Predominantly these reactions result from binary Rydberg electron-target interactions.

The remainder of this text will discuss electron attachment studies performed using potassium Rydberg atoms. The apparatus used to perform the experiments is described along with the model used to analyze the results. The experiments performed demonstrate the power of the method. Dissociative electron attachment to bromotrichloromethane ($CBrCl_3$) is discussed including future studies of the effects of increased target temperatures. Non-dissociative electron attachment reactions with hexafluorobenzene (C_6F_6) and with perfluoromethylcyclohexane (C_7F_{14}) are also discussed. In the present experiments the basic energetics of the interactions and the lifetimes of the intermediate ions are determined.

Chapter 2
Apparatus

The present work is performed in a differentially pumped vacuum system containing the apparatus shown in figure 2.1. Potassium atoms contained in a collimated beam (formed by an effusive oven) are excited to high Rydberg states using the UV output of an intra-cavity doubled ring-dye laser. The laser beam is incident at an angle of ~2° off normal to allow velocity selection of the Rydberg atoms via Doppler tuning. Experiments are run in pulsed mode to incorporate time-of-flight techniques. An acousto-optic modulator chops the laser output into pulses of ~1 μs duration with a repetition frequency of ~5 kHz. Excitation occurs at the center of an interaction region defined by two parallel plates containing fine-mesh copper grids. After excitation, a short time delay allows the Rydberg atoms to interact with the target molecules, which exist as an ambient gas in the vacuum chamber. Then, an electric field is applied to the plates to extract collision products into two time-of-flight mass spectrometers (TOFMS) located symmetrically above and below the interaction region. Each TOFMS terminates in a position sensitive detector (PSD), which records both the arrival time and position of the product ions. Data acquisition, analysis, and modeling are accomplished using Macintosh computer systems. To perform a variety of different experiments, parts of the TOFMSs can be replaced with pieces designed for specific tasks. For example, a heated interaction region is available to increase the internal energy of target molecules, as will be discussed for future temperature dependence studies involving $CBrCl_3$. Future work will also include a Penning trap which can be substituted for one of the drift regions in figure 2.1. The trap design will be discussed in chapter 6 along with a set of possible future experiments.
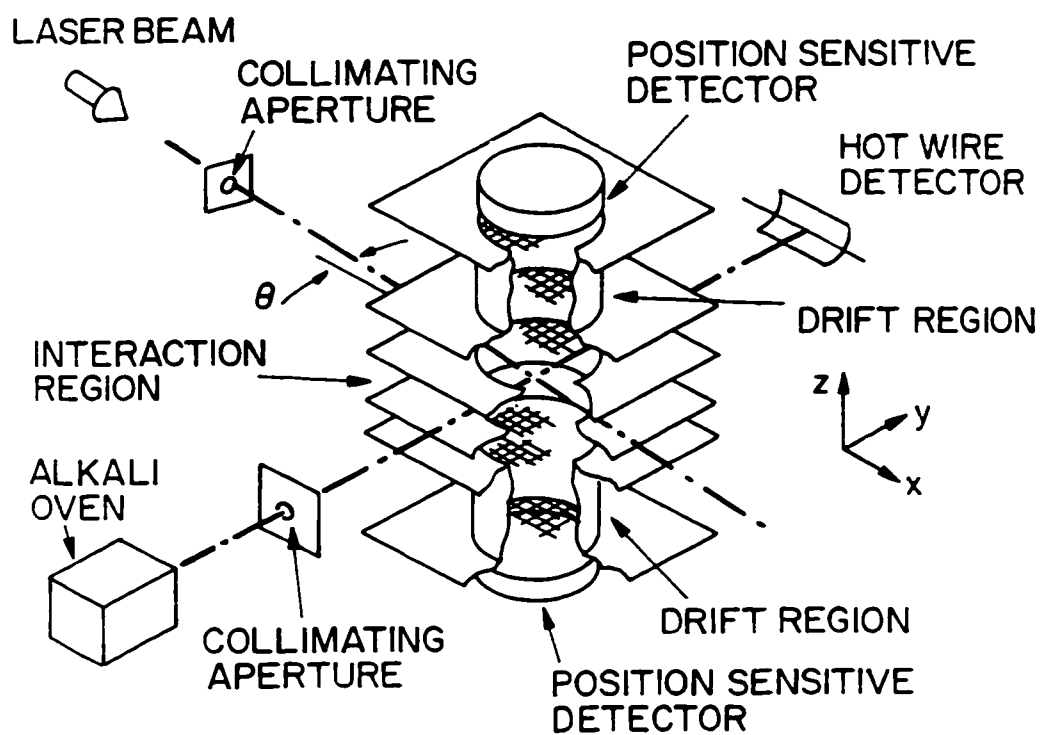
Figure 2.1 Schematic diagram of the apparatus.

2.1 Vacuum System

Performing experiments in a high vacuum environment minimizes the influence of collisions with background gas. The background pressure is typically $\sim 2 \cdot 10^{-7}$ Torr. A gas manifold allows the introduction of the target gas at a pressure that can be precisely controlled using a needle valve. Target gas pressures are limited to $\leq 5 \cdot 10^{-5}$ Torr by the capabilities of the diffusion pumps that evacuate the main experimental region. The vacuum chamber consists of two differentially pumped regions connected by a heated aperture assembly, described below. A single 4" diffusion pump, which provides a pumping speed of 820 liters per second, evacuates the oven region, and the main experimental region is pumped by two 6" diffusion pumps with pumping speeds of 1500 liters per second each.

The smaller chamber contains a stainless steel oven which heats solid potassium to $\sim 300°$ C, well above its melting point of 63.2° C. Alkali atoms effuse through a 0.5 mm aperture in the oven nose and are collimated by a heated aperture assembly before entering the adjoining region to create a beam of potassium atoms. The aperture assembly has two openings separated by ~ 5 cm, the first aperture is ~ 1.6 mm in diameter and the beam-defining exit aperture has a diameter of ~ 0.3 mm. Tungsten wire wound about a macor core heats the assembly to ensure that potassium will not condense on and, thereby, clog the aperture. The assembly's design permits separate biasing of the beam-defining aperture if needed.

The beam width at the center of the interaction region is calculated as follows. The nose aperture, 0.5 mm, and the final defining aperture, 0.3 mm, are separated by ~ 6.27 cm. The beam width, w, at some distance, y, from the

defining aperture depends on the angle formed by the apertures, θ, according to the equation:

$$w = 2 \cdot y \cdot \tan\left(\tfrac{\theta}{2}\right) + 0.3 \qquad (2.1)$$

where 0.3 is the width of the defining aperture in millimeters. The angle can be found through the simple geometry shown in the diagram below.
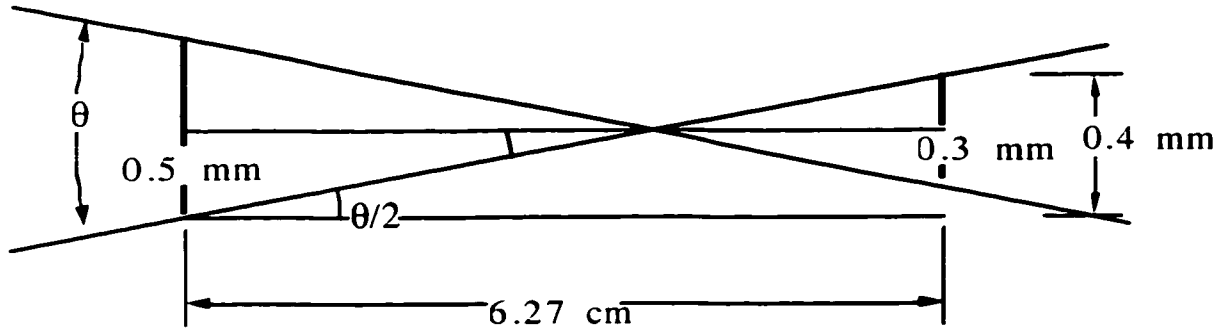
$$\tan \tfrac{\theta}{2} = \tfrac{0.04}{6.27} \Rightarrow \theta \approx 0.7°$$

Using equation 2.1 with a distance y = 73.0 mm, equal to that from the defining aperture to the center of the interaction region, the potassium beam width is found to be w ≈ 1.2 mm.

The alkali beam flux is monitored using a hot-wire detector. The detector consists of a high-resistance tungsten filament fixed to a rotatable arm, protruding through an ultraTorr fitting in one chamber flange. The arm moves the hot filament, heated by an external power supply, into or out of the potassium beam. The potassium atoms ionize on the wire, and the current produced by ionization is monitored using a sensitive electrometer. The current is, therefore, directly proportional to the potassium beam density.

2.2 Dual Mass Spectrometer Assembly

The two mass spectrometers are symmetrically opposed on either side of the interaction region, which is defined by two fine mesh grids separated by ~19 mm. One of the grids is grounded and the other is supplied with a pulsed extraction ramp. Each spectrometer consists of a series of parallel copper grids that can be individually biased to create a series of acceleration and drift regions for the product ions. The spectrometers each end in a position sensitive detector (PSD) that records the arrival times and the impact positions of the ions. The detectors consist of two microchannel plates (MCP) followed by a resistive anode. A bias network circuit divides the voltages applied to the microchannel plates such that no more than a 1000 volt differential exists between the front and back of a single plate. Further, the time of flight of the ions is determined by observing the current pulse from the back of the second MCP. The position of ion impact is determined by measuring, at each of the four corners of the square anode, the current caused by an electron shower striking the PSD surface. Using the four current values, the detector calculates the distance of the impact location from each corner and translates the data into a distinct position. With the detector operating in analog mode the position calculation takes ~8 μs, or ~14 μs in digital mode. These are considered the dead time values for the detector.

The pulse applied to the interaction region causes significant electrical pickup problems at the detectors. This can be minimized by capacitively coupling the drift region grids adjacent to the interaction region to ground.

2.3 Laser System

The central laser system consists of a Coherent CR-699 intra-cavity doubled, ring dye laser pumped by a Coherent I-400 Ar ion laser. This combination provides the flexibility necessary to excite a significant range of Rydberg energy states. Using Rhodamine-6G dye, the CR-699 has a visible output ranging from 565 nm to 625 nm. The visible light in the cavity of the dye laser passes through a Potassium Diphosphate (KDP) doubling crystal, which produces the ultraviolet light necessary to excite potassium atoms to Rydberg states from $n = 10$ up to at least $n = 100$. The UV output is continuous wave, but since the present experiments are conducted in pulsed mode, an acousto-optic modulator (AOM) chops the output into pulses of ~1 µs in length.

The excitation of Rydberg atoms requires a high degree of frequency stability in the laser system. The CR-699 is internally stabilized against short-term jitter by a temperature stabilized reference cavity and has a natural linewidth of ~200 kHz. The dye laser is, however, still subject to long-term drift. To minimize this problem two commercially available, temperature stabilized HeNe lasers are used to monitor and to control the CR-699. One of the HeNe lasers operates as part of an interferometer used to monitor the exact frequency of the dye laser output, to an accuracy of ~0.01 Å in wavelength. The other HeNe laser functions as part of a stabilization system termed Superlock, which limits long-term frequency drift in the dye laser output to less than ~±2 MHz (UV) per day. Superlock is a feedback system that uses an interferometer to constantly compare the difference in wavelength between the stabilized HeNe and the visible output of the CR-699. If the dye laser wavelength begins to drift Superlock detects

a change and sends a signal to the CR-699 internal reference cavity, which adjusts piezo-electric elements within the dye laser cavity to correct the drift.

The UV laser light enters the vacuum system after passing through a lens and a window oriented at Brewster's angle. The lens has a focal length of 50 cm, and the center of the interaction region is slightly less than 50 cm away from the lens. The beamwaist of the laser at the center of the interaction region is estimated to be $\lesssim 150$ μm. For a more detailed description of the dye laser system and the theory of its operation, see reference 5.

2.4 Electronics and Computer System

The timing of the experiment is managed by an electronics/computer interface system. This CAMAC (Computer Automated Measurement and Control) system allows the user to control the start time, several important electronic delays, the stop time, and how the data are recorded. Each experiment described here requires somewhat different experimental procedures so the setup for each will be described separately. The important elements of the electronics include a master pulse generator with an external triggering capability, several commercially available Gate and Delay modules, various signal converters, Analog to Digital converters (ADCs), and a Quad Event Timer (QET) which records the flight time of the ions to each detector. The experiments typically run at ~5 kHz which allows enough time for the electronics and the computer to cycle through reading and storing the data.

A Macintosh Quadra 800 communicates with the CAMAC interface using data acquisition and analysis codes written in the computer language

C. The computer code is written in-house and can be modified as needed to run different experiments and to execute various analyses. A separate computer system is used to perform the model calculations with which the data are compared. A description of the model will be given in the next chapter. The model itself is quite simple; however, the code needed for the simulation is complicated enough to require a faster computer system. Further, having the separate system enables simultaneous acquisition of data and execution of model calculations.

2.5 Heated Interaction Region

The standard interaction region, as described in section 2.2, incorporates two parallel, thin copper plates with inlaid fine mesh copper grids. In order to study the effects of internal temperature on collisional processes, a method of heating the interacting species is necessary. Therefore, the region described below was developed to replace the standard interaction region. The heated interaction region also consists of two parallel copper plates with inlaid grids. However, the diameter of the grids is greatly decreased to minimize the flow rate of the heated species out of the heated interaction region. Because of the decreased size and greater sensitivity to fringing fields, care must be taken to insure that the grids lie flush with the surface of the copper plate to avoid any inhomogeneity in the extraction field which would invalidate the position data. To accomplish such uniformity, a system of two grids per plate is used, one grid flush with the top/outside and one flush with the bottom/inside. Further, a circular barrier projects from the surface of each plate to enclose the centermost area of the interaction region. Four small portals in the barriers allow entrance and exit

of the laser beam and the potassium atom beam. The copper plates are heated using four commercially available 80W, 120V cartridge heaters made by Gaumer, two imbedded into each plate. This heating scheme expands the experimental temperature range from room temperature up to ~250° C. Because the target molecules exist as an ambient gas, a few collisions with the heated plates are sufficient to raise their internal temperatures within the same range. Care must be taken such that the temperature of the PSDs does not change significantly. Thermocouples are installed in front of the bottom detector and on the grounded plate of the heated interaction region. (Attaching the thermocouple to the pulsed interaction region plate caused serious electrical pickup problems, which even capacitive coupling could not overcome.) The thermocouple on the PSD is monitored to avoid overheating, while the one attached to the interaction region acts as input to a temperature controller that uses a feedback loop to maintain the interaction region at a given temperature.

Chapter 3
Model

As mentioned previously, for principal quantum numbers n $\gtrsim 10$ the average separation of the Rydberg electron from the core ion, consisting of the nucleus and interior shell electrons, exceeds the interaction distance of most atom-molecule collisions. The core ion and Rydberg electron can, therefore, be considered as independent scatterers in collisions with neutral target molecules, as described by the free electron model. This allows electron attachment reactions of the form:

$$e^- + ABC \rightarrow ABC^{-*} \tag{3.1}$$

to be considered in terms of a binary interaction between the target and the Rydberg electron, as shown previously.

$$
\begin{aligned}
K(np) + ABC \rightarrow K^+ + ABC^{-*} &\rightarrow K^+ + C^- + AB \\
&\rightarrow K^+ + ABC^- \\
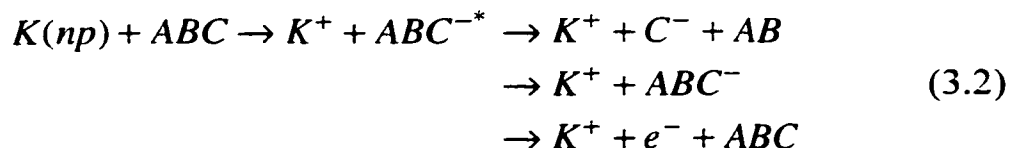&\rightarrow K^+ + e^- + ABC
\end{aligned} \tag{3.2}
$$

Figure 3.1 illustrates the basic steps of the interaction, which can be modeled using Monte Carlo techniques. The model chooses the initial reactant velocities from appropriate distributions and uses the quantum statistical electron probability distribution around the Rydberg core as a distribution of the separations at which the attachment of the Rydberg electron occurs. (Figure 3.1a) Classical orbital mechanics is used to follow the motions of the Rydberg core and the intermediate negative ion interacting under their mutual Coulombic attraction. (Figure 3.1b) Then after
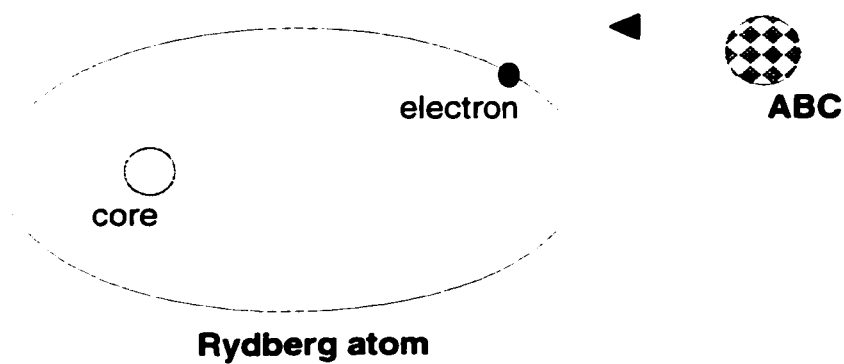
Rydberg atom

Fig. 3.1a   Target attaches Rydberg electron
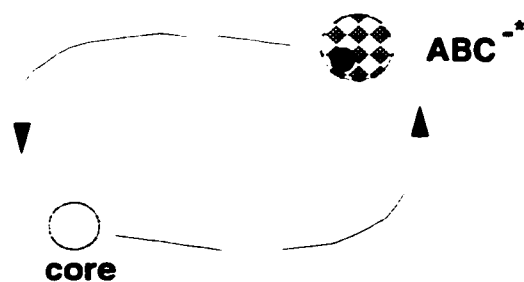

Fig. 3.1b   Post-attachment Coulombic attraction to Rydberg core ion

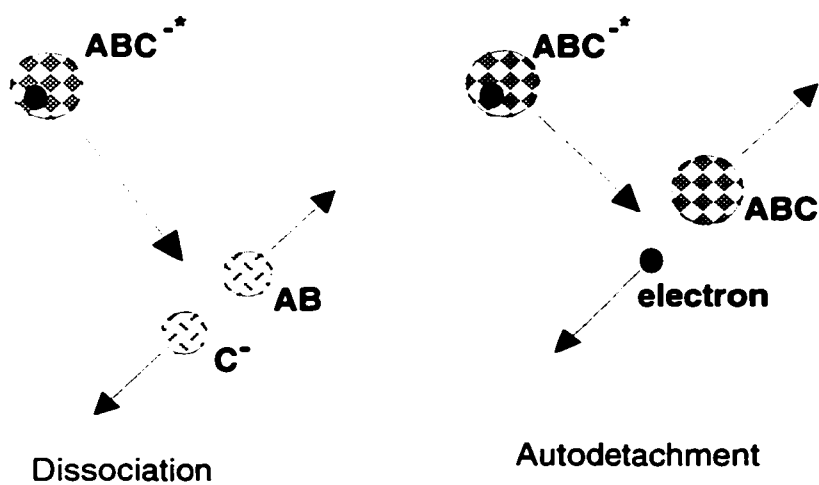Dissociation   Autodetachment

Fig. 3.1c   Possible products formed by intermediate after lifetime

Figure 3.1   Basic steps of Monte Carlo simulation.

some lifetime, τ, the intermediate ion either dissociates forming a neutral particle and a negative ion, or separates from the Rydberg core forming a metastable, which can autodetach the electron within the time scale of the experiment. (Figure 3.1c) In either case, the final distribution of the product ion velocities is used to determine the arrival position distributions at each detector. A more detailed description of the simulation follows.

The model begins by establishing the initial states of the Rydberg atom and the target molecule. The initial velocity of the Rydberg atom is chosen at random from the initial velocity distribution of the atoms in the beam, which in the case of a velocity selected beam is specified by a mean velocity and a standard deviation, i.e. a Gaussian distribution of the form:

$$f(v) \propto e^{-\frac{(v-\bar{v})^2}{2\sigma^2}}$$ (3.3)

where v is the atom velocity, $\bar{v}$ is the mean velocity, and σ is the standard deviation. The program stores the Gaussian distribution in a lookup table divided into bins of equal probability. From this table, the model randomly chooses a velocity for the Rydberg atom. In the absence of velocity selection, the model picks the initial state randomly from a Maxwell-Boltzman distribution. The probability for excitation to a Rydberg state is proportional to velocity; so, a factor of v^{-1} corrects the M-B distribution for an effusive beam giving:

$$f(v) = 4\pi\left(\frac{m}{2kT}\right)^{3/2} v^2 e^{\frac{-mv^2}{2kT}}$$ (3.4)

v = velocity of atoms
m = mass of atoms
k = Boltzman's constant
T = temperature of the atoms

which is stored in a lookup table broken into equal probability bins.

The initial location of the Rydberg atom is determined from the size of the potassium beam and the size of the laser spot at the point of intersection with the potassium beam. Again, the model chooses a random location within the intersection volume and assigns it as the excitation position of the Rydberg atom.

The model allows for target molecules in either a crossbeam or an ambient gas configuration. The initial velocity for the target in a crossbeam configuration is chosen from a Maxwell-Boltzman distribution, as done previously for the Rydberg beam. The velocity distribution in an ambient gas follows the relation between the kinetic energy and the thermal energy:

$$\tfrac{1}{2}m\bar{v}_i^2 = \tfrac{1}{2}kT \tag{3.5}$$

for each of the three dimensions (i = x, y, z), which gives a mean velocity of:

$$\bar{v}_i = \sqrt{\tfrac{kT}{m}} \tag{3.6}$$

A Gaussian distribution is used in each dimension to emulate a molecule moving in a random direction with a velocity spread centered on the most likely value given by equation 3.6. The initial target position at which attachment occurs is taken as a random point in a spherical volume extending from the Rydberg core radius to the maximum effective radius of the Rydberg electron cloud. The model uses the quantum mechanical description of the radial electron density distribution for a one-electron, i.e. hydrogenic, atom to determine the maximum radius of interaction. The normalized radial probability distribution is described by the equation:

$$R(\rho) = C \cdot e^{-\rho} \cdot \rho^{2\ell+2} \cdot L^{2\ell+1}_{n-\ell-1}(\rho) \tag{3.7}$$

where C is a normalization constant, and ρ is proportional to the radial variable, r. Each is defined as follows:

$$C = \frac{Z \cdot (n - \ell - 1)!}{a_0 \cdot n^2 \cdot (n + \ell)!}$$

$$\rho = \frac{2 \cdot Z \cdot r}{a_0 \cdot n}$$

Z is the atomic number, n the principal quantum number, ℓ the angular momentum quantum number, and a_0 the Bohr radius. L in equation 3.7 refers to the Laguerre polynomials.[13] The maximum radius of interaction is then obtained by integrating equation 3.7 out to a radius sufficient to encompass 99.9% of the electron density.

The probability of electron capture depends on the interaction time of the attaching target with the Rydberg atom, and is given by:

$$P(t) = 1 - e^{-\rho k t} \tag{3.8}$$

which can be approximated, when $\rho kt \ll 1$, by:

$$P(t) = \rho kt \tag{3.9}$$

where k is the rate constant for electron capture, ρ is the gas density, and t is the interaction time. Further, the interaction time depends on the experimental timing, where the total time available begins with the laser pulse and ends at extraction of the interaction products. This time increment can be broken into two parts: the width of the laser pulse, t_L, and the delay

time between the end of the laser pulse and the beginning of the extraction pulse, t_D. The Rydberg atom can only form during the laser pulse, but electron attachment is possible anytime after the Rydberg atom formation, at time t_R, until the extraction pulse occurs. In other words, the interaction time is the total time available ($t_L + t_D$) minus the Rydberg formation time (t_R). This time interval can be described by:

$$t(t_R) = \begin{cases} t_L + t_D - t_R & \text{for} \quad 0 \le t_R \le t_L \\ 0 & \text{for} \quad t_R \ge t_L \end{cases} \tag{3.10}$$

where t is the interaction time. The probability of electron attachment for a Rydberg formed at time t_R then becomes:

$$P(t_R) = \rho k(t_L + t_D - t_R) \tag{3.11}$$

The distribution of Rydberg formation times, t_R, leading to electron attachment is given by normalizing equation 3.11 as follows:

$$\rho k \int_0^\infty (t_L + t_D - t_R) dt_R \approx \int_0^{t_L} (t_L + t_D - t_R) dt_R + \int_{t_L}^\infty (t_L + t_D - t_R) dt_R = 1 \tag{3.12}$$

t_R is defined only in the range $0 \le t_R \le t_L$ so the integration for $t_R \ge t_L$ must equal zero. The normalization constant is determined from the integration, and the final distribution is given by:

$$f(t_R) = \frac{2(t_L + t_D - t_R)}{(t_L^2 + 2t_L t_D)} \quad 0 \le t_R \le t_L \tag{3.13}$$

The model determines t_R from equation 3.13. Since the probability of attachment per unit time, $\frac{dP}{dt}$, is constant, as seen in equation 3.9, the ion

formation time is chosen randomly between t_R, the Rydberg formation time, and $t_L + t_D$, the time until extraction.

After establishing all the initial conditions, the time remaining before extraction and the electron probability density at the point of attachment are calculated. The electron density is used to weight the probability that attachment occurs at that point. If dissociation of the intermediate is specified, the time until dissociation is determined by the distribution:

$$f(t) = \tfrac{1}{\tau} e^{-\frac{t}{\tau}}$$

(3.14)

where τ is the mean lifetime, given as a parameter. The time until dissociation is compared with the remaining interaction time to filter events that do not dissociate prior to the extraction pulse. The model then uses classical orbital mechanics to propagate the system to the time of dissociation.

At dissociation, the energy of the product ion is chosen from a distribution representing the assumed dissociation behavior. Two typical cases exist: an intermediate with a short lifetime or a long-lived intermediate. If dissociation occurs after a very short period of time, τ less than one vibrational period, there is little opportunity for the redistribution of the excess energy of reaction among internal vibrational modes of the molecule. This implies that all of the excess energy appears in translation of the product ion, which leads to a narrow energy distribution of width, σ_ε, centered on a mean energy, $\bar{\varepsilon}$, typically, the excess energy of reaction. A Gaussian translational energy release distribution of the form shown below represents such a case:

$$f(\varepsilon) = \frac{1}{\sqrt{2\pi}\sigma_\varepsilon} e^{-\frac{(\varepsilon-\bar{\varepsilon})^2}{2\sigma_\varepsilon^2}} \tag{3.15}$$

In the case of a long-lived intermediate, a significant amount of the available excess energy couples into the internal vibrational modes of the molecule. Very little of the energy, therefore, appears in translation of the product. According to unimolecular decay theory, this results in an exponential translational energy release distribution of the form:

$$f(\varepsilon) = \frac{1}{\bar{\varepsilon}} e^{-\frac{\varepsilon}{\bar{\varepsilon}}} \tag{3.16}$$

After dissociation, a comparison is made between the potential energy of the product anion relative to the Rydberg core ion:

$$PE = \frac{q_1 q_2}{4\pi\varepsilon_0 r} \tag{3.17}$$

q_1, q_2 = charges of ions
ε_0 = permitivity of free space
r = separation of ions

and the relative kinetic energy of the products:

$$KE = \tfrac{1}{2}\mu\dot{r}^2 \tag{3.18}$$

where μ is the reduced mass and $\dot{r}$ is the relative velocity. If the kinetic energy is sufficient to allow the product ion pair to overcome their Coulombic attraction, the path of the product of interest – either the Rydberg core cation or the target anion – is propagated, again using classical orbital mechanics, for the time remaining prior to extraction. Then, the time of

flight through the mass spectrometer is determined, and the arrival position on the detector is calculated, weighted by the electron probability density, as mentioned previously. To obtain a clearer picture of the experimental collisions a range of velocities in the z-direction, as defined in Figure 2.1, can be specified in order to analyze only events happening in a small thickness around the plane of interaction. Only if the event occurs within this velocity window is it recorded. If the product ions are bound, the event is discarded.

For non-dissociating targets, there are two possible processes to model. The intermediate ion either autodetaches the electron or is assumed to have an infinite lifetime, i.e. is metastable on the time scale of the experiment. Autodetachment is modeled in the same way as dissociation, except that the dissociating product's mass is taken to be the mass of an electron. For metastable targets, the model simply checks if the initial Coulombic attraction between the intermediate ion and the Rydberg core results in an elliptical orbit or in a hyperbolic orbit. The elliptic orbits represent bound ion pairs, and the events are discarded. The hyperbolic orbits are propagated until the extraction field is applied and then followed through the mass spectrometer. Again, if events occur within the correct velocity windows the data are recorded.

By iterating through many such events from ion formation through detection of the products, a position/velocity distribution is built up. Additional information can be gleaned from the simulation as needed since the model works on an event by event basis. Further information about the Monte Carlo simulation can be found in reference 14.

Chapter 4
Dissociative Targets

4.1 Introduction

Many molecules with a high electron affinity readily attach electrons but dissociate after some short lifetime. Attachment processes, as described previously, vary and lead to a wide range of stabilities. Dissociative electron attachment by target molecules in collisions with potassium Rydberg atoms are represented by the equation:

$$K(np) + ABC \rightarrow K^+ + ABC^{-*} \rightarrow K^+ + C^- + AB \qquad (4.1)$$

As described previously, after attaching the electron to form an excited intermediate ion, ABC^{-*}, the anion has a Coulombic attraction to the positive Rydberg core. After some lifetime, τ, the intermediate ion dissociates into a neutral, AB, and a negative ion, C^-. For Rydberg atoms with high principal quantum numbers, n $\geq$ 30, post-attachment interactions between the intermediate ion and the Rydberg core are negligible. Therefore, the final arrival position distributions of the product anion and the Rydberg core at high n are governed exclusively by the translational energy release of the products accompanying dissociation. At lower n values, the intermediate ion forms in close enough proximity to the Rydberg core that post-attachment electrostatic interactions between the intermediate and the core become important. The dissociation of the intermediate is an isotropic process on average, and product ions that dissociate travelling in the same direction as the Rydberg core ions will have a high probability of being bound to the Rydberg core because the relative kinetic energy between the two can be

very small. Such bound pairs are undetected. This process is referred to as velocity matching. The extent of this effect depends on the lifetime of the intermediate ion, which determines its interaction time with the Rydberg core ion. Longer interactions between the intermediate ion and the Rydberg core work to reduce the anisotropy of the K^+ distribution. Thus, the longer the lifetime, τ, the less evident velocity matching becomes. The arrival position/velocity distribution of the product ions at low n demonstrate a significant minimum in signal along the direction of the K-beam for small τ, and the effect diminishes as τ is increased. The distributions recorded for low-n interactions, therefore, are used to determine the lifetime of the intermediate ion on a picosecond time scale.

The dissociative target studied in this work is $CBrCl_3$ (bromotrichloromethane). This particular target is chosen because it reacts differently at varying temperatures. Two product ions are observed following electron attachment reactions with $CBrCl_3$, Cl^- and Br^-. Earlier threshold photoelectron spectroscopy studies of electron attachment to $CBrCl_3$ observed only Br^- production, [15] but other measurements, including swarm and crossed-beam techniques, report both Br- and Cl^- formation. [16, 17, 18] It has been suggested that the Cl^- signal is a by-product of Br^- formation via attachment to CCl_3 radicals, but the low Rydberg atom densities used in the present studies precludes such a possibility. [19]

4.2 Low Temperature $CBrCl_3$ Experiment

The present apparatus is shown in figure 2.1 and described in detail previously along with the basic operation of the experiments. To review, the

experiments are run in pulsed mode with an acousto-optic modulator

chopping the laser beam into pulses of 0.5 µs duration. The laser beam

crosses a beam of potassium atoms, created by an alkali oven, at an angle of

~2° off normal incidence. Potassium Rydberg atoms are excited at the center

of an interaction region defined by two parallel fine mesh grids and can be

velocity selected using Doppler tuning. Current measurements are performed

at a Rydberg atom velocity of $6 \cdot 10^4$ cm s^{-1}. The Rydberg atoms are allowed

to interact with background $CBrCl_3$ target gas for a specified interval

(~0.5 µs) before an extraction field is applied between the interaction region

plates. The product ions of the reaction:

$$K(np) + CBrCl_3 \rightarrow K^+ + CBrCl_3^{-*} \rightarrow K^+ + Br^- + CCl_3$$
$$\rightarrow K^+ + Cl^- + CBrCl_2 \qquad (4.2)$$
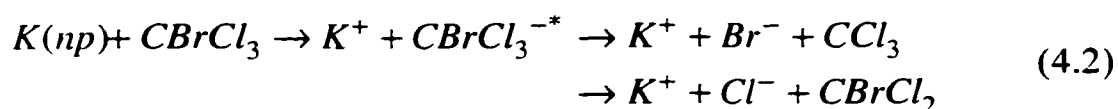
namely K^+, Br^-, and Cl^- are expelled into two time-of-flight mass

spectrometers (TOFMSs), located symmetrically above and below the

interaction region. The ions are accelerated upon exiting the TOFMSs and

detected by position sensitive detectors (PSDs). The products are detected in

coincidence to ensure they come from the reaction of interest. Coincidence

detection refers to recording only data for which a product ion strikes each

of the upper and lower detectors during the same data cycle and at the

expected flight times. Time-of-flight techniques are used to identify the

products. Typical flight times through the TOFMSs are 5-10 µs; this is

sufficient to resolve the two isotopes of each product, $^{81}Br/^{79}Br$ and

$^{35}Cl/^{37}Cl$.

The exact flight time of the ions depends on their initial velocities in the z direction, as defined in figure 2.1. Figure 4.1 shows arrival time distributions for the product ions, K^+ (4.1a), Br^- (4.1b), and Cl^- (4.1c) from reaction 4.2 for Rydberg atoms with n = 45. Notice that the isotopes are clearly separated in 4.1b and 4.1c and that each distribution can be approximately fit with a Gaussian distribution, which implies that there is some width associated with each distribution. The spread of velocities in the z direction causes the width in the time of flight peaks with those ions initially formed travelling in the z direction away from their detector arriving later than those with initial velocities directed toward their detector. Thus, the peak of each distribution represents those ions whose initial z velocities equal zero; i.e. those product ions initially formed traveling in the horizontal x-y plane. Restricting analysis to data falling within a small window around the peak of the distribution (a velocity window) isolates the collisions producing product ions travelling in the plane of interaction and provides a clearer picture of the reaction characteristics.

4.3 Low Temperature $CBrCl_3$ Analysis

Experimental distributions are compared with model calculations obtained using the Monte Carlo simulation described previously. The position distributions, both experimental and calculated, are reconfigured to more clearly illustrate the reaction characteristics. High n data, which
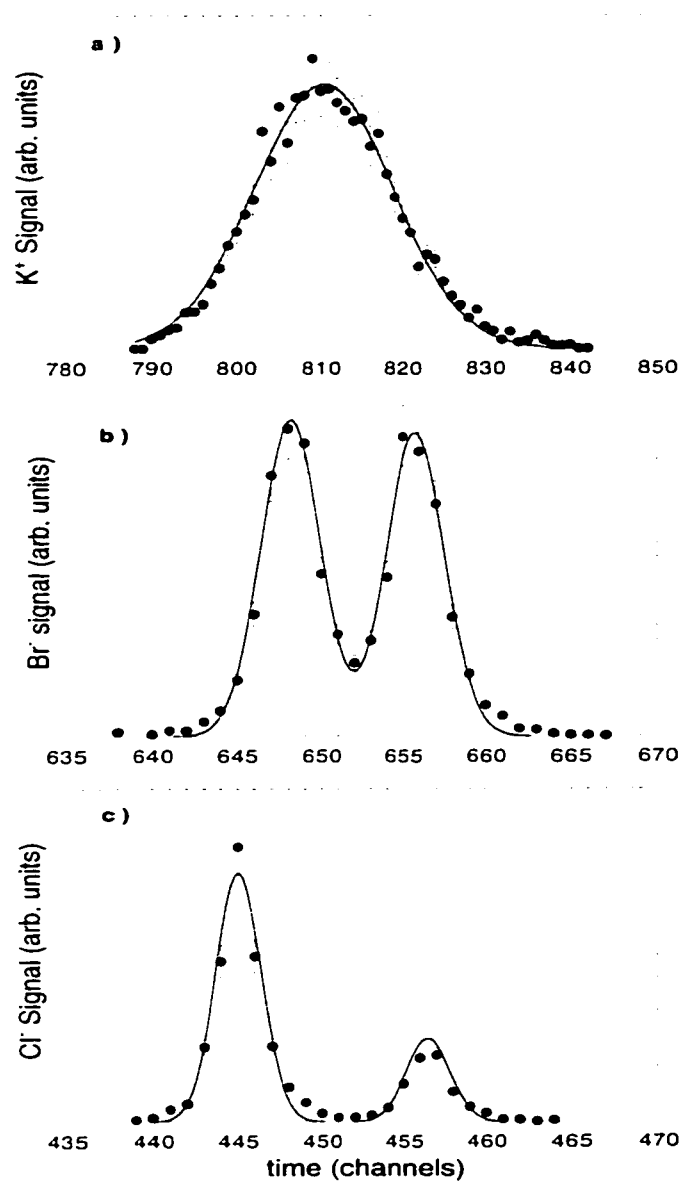
Figure 4.1   Arrival time distributions for product ions (a) K^+, (b) Br^-, (c) Cl^- produced in $K(45p)/CBrCl_3$ collisions. ● represent data with statistical error bars, and the lines represent Gaussian fits to the data (see text).

provide information about the translational energy release, are viewed as radial distributions. A radial distribution is formed by dividing the active, circular PSD surface into concentric circles, summing the signal in each ring, and plotting signal, weighted by the radius, versus average radius from the center of the PSD. For low n data post-attachment electrostatic interactions distort the position distributions and provide intermediate ion lifetime information. Low n data are viewed as angular distributions. An angular distribution is formed by dividing the active PSD surface into pie slices, summing the signal in each slice, and plotting signal versus angle where the forward direction of the K-beam is considered 0°.

Before discussing the $CBrCl_3$ data analysis, it is important to point out some differences in the analysis techniques used with dissociative targets versus corrections necessary for non-dissociative targets, which will be described later. First, for dissociative target molecules there is no background signal to subtract from the data. Background signals, observed with no target gas, result from photoionization of the Rydberg atoms by the omnipresent blackbody radiation and produce K^+ ions and electrons as products. Reactions between potassium Rydberg atoms and $CBrCl_3$ produce no observable excess electron signal. Therefore, since the data are recorded as coincidence events between K^+/Br^- and K^+/Cl^- no reactions between the potassium Rydberg atoms and the blackbody radiation will be recorded. Further, because the data are velocity windowed for analysis, thereby simplifying the use of radial and angular distributions, it is not necessary to ensure that the center of the experimental data coincides with that of the model. The radial and angular distributions are calculated based on the center of each individual position distribution, experimental or calculated.

Comparisons have been done using $CBrCl_3$ and shifting the experimental data center within a reasonable error range to show there is no effect on the final conclusions about the intermediate ion lifetime or reaction energetics.

To aid in the interpretation and understanding of the experimental data, first-principles calculations based on the local-spin-density approximations of the density-functional theory were performed.[20] Table 4.1 provides calculated bond dissociation energies and effective charges for each atom in both the neutral molecule and the molecular negative ion. The effective charges are calculated using Mulliken charge population analysis.[21]

Table 4.1

A. Bond dissociation energies

Species	Neutral Product	Bond dissociation energy (eV)	
		Calculated	Present Work
CCl_3Br	Br	2.67	2.7
	Cl	3.60	≤ 3.5

B. Mulliken effective atomic charges

Species	Site	Charge (a.u.)		
		Neutral molecule	Negative ion	Difference
CCl_3Br	C	+0.165	+0.171	+0.006
	Br	+0.031	-0.197	-0.228
	Cl	-0.065	-0.325	-0.260

The radial distribution of the Br⁻ ions formed via the reaction:

$$K(45p) + CBrCl_3 \rightarrow K^+ + CBrCl_3^{-*} \rightarrow K^+ + Br^- + CCl_3 \qquad (4.3)$$
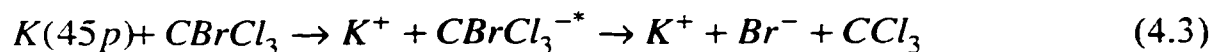
is shown in figure 4.2. The $^{79}Br^-$ and $^{81}Br^-$ signals, which are of approximately equal abundance, are summed to reduce statistical uncertainties. Two distinct peaks are apparent in figure 4.2, which implies that two separate reaction channels are operative. The peak at small r corresponds to reactions in which little energy appears in translation of the product ions. This suggests a reaction associated with a long-lived intermediate ion where much of the excess energy of reaction is transferred to internal motions of the molecule. The peak at larger r characterizes a very short-lived intermediate ion, which dissociates before any redistribution of the energy to internal molecular motions can occur. All of the excess energy of reaction therefore appears in translation of the product ions.

The results of model calculations are also shown in figure 4.2. The fit to the data at large r assumes a Gaussian translational energy release distribution with 75 meV full width half max (FWHM) centered on an energy $\bar{\varepsilon} \sim 0.7$ eV. A Gaussian distribution is appropriate for an interaction associated with a short lifetime intermediate ion in which $\bar{\varepsilon}$ is the mean translational energy release of the product ions. The total excess energy of reaction is given by:

$$\bar{\varepsilon} = EA(Br) - D_0(CCl_3 - Br) + E_{int} + E_K(e^-) \qquad (4.4)$$

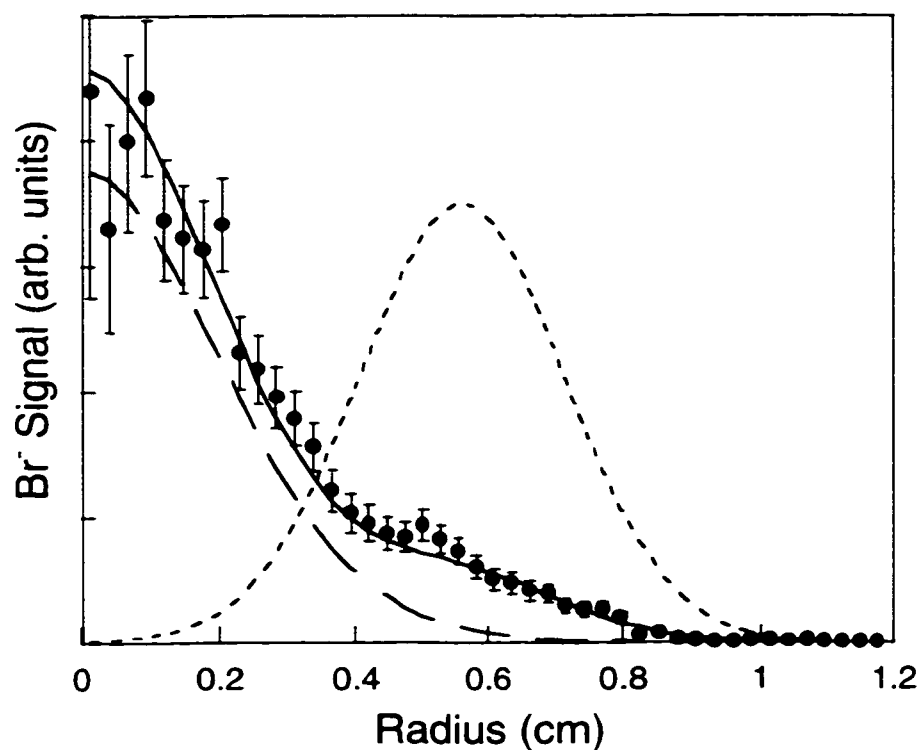**Figure 4.2** Radial distribution of Br⁻ ions produced in K(45p)/CBrCl₃ collisions. • represents data including statistical error bars; the lines represent model calculations assuming: ---- (short dashes) Gaussian distribution with $\bar{\varepsilon}$ ~ 0.7 eV and 75 meV standard deviation, —— (long dashes) two-dimensional Boltzman distribution with $\bar{\varepsilon}$ ~ 0.15 eV, solid line combines the other two calculations for a reaction channel ratio of 50% each.

where EA(Br) is the electron affinity of Br, 3.36 eV, $D_0(CCl_3\text{-}Br)$ is the $CCl_3\text{-}Br$ bond dissociation energy, E_{int} is the available internal energy in the parent molecule, and $E_K(e^-)$ is the median kinetic energy of the attached electron, which is negligible at $n = 45$. Assuming that all the excess energy appears in translation, $E \sim 0.7$ eV, which implies that $D_0(CCl_3\text{-}Br)$ must be $\lesssim 2.7$ eV. This provides an upper limit for the bond dissociation energy because if some of the excess energy is lost to internal motions of the molecule E must be $> \bar{\varepsilon}$, the translational energy release, which requires an even lower value of D_0. This value agrees well with the calculated value shown in table 4.1.

As mentioned earlier, the unimolecular decay theory predicts reactions involving intermediate ions with lifetimes long enough to allow near statistical redistribution of energy into the internal motions of the molecule prior to dissociation can be described by an exponential translational energy release distribution (a two-dimensional Boltzman distribution) of the form:

$$f(\varepsilon) = e^{-\frac{\varepsilon}{\bar{\varepsilon}_B}}$$

(4.5)

where $\bar{\varepsilon}_B$ is the mean translational energy release.[22] This can be seen in figure 4.2. The best fit to the small r data feature assumes a two-dimensional Boltzman distribution with mean energy $\bar{\varepsilon} \sim 0.15$ eV. Simple statistical considerations predict a much lower energy:

$$\bar{\varepsilon}_B = \frac{E}{N}$$

(4.6)

by assuming the excess energy of reaction, E, is evenly distributes over the N internal modes of the intermediate ion prior to dissociation.[23] For a nonlinear molecule with M atoms:

$$N = 3M - 6 \tag{4.7}$$

which gives an expected mean translational energy release of ~ 0.08 eV for $CBrCl_3$. It is not uncommon for the predicted value to underestimate the measured value by as much as a factor of 2, and similar electron attaching targets like CCl_4 and CCl_3F have shown equivalent differences between expected and measured values.[24, 25]

The solid line fit to the data seen in figure 4.2 combines the best fits for the two features in a ratio assuming ~50% of the Br^- signal results from a long-lived intermediate and ~50% from a short-lived intermediate. For the low n studies (n = 14) the ratio between the two reaction channels changes. Figure 4.3 shows the radial distribution for Br^- data obtained in K(14p)/$CBrCl_3$ collisions. The same two features appear, and model calculations suggest that the same fits apply. However, the fit to the overall radial distribution assumes that ~30% (70%) of the collisions are associated with formation of short-lived (long-lived) intermediates. The same mix of reaction channels fits the angular distribution of the Br^- ions obtained at low n, as seen in figure 4.4. The angular distribution is not very sensitive to the lifetime of the long-lived intermediate, but the best fit to the data is obtained for a lifetime of ~ 5 ps.

The second reaction product, Cl^-, is formed via the process:
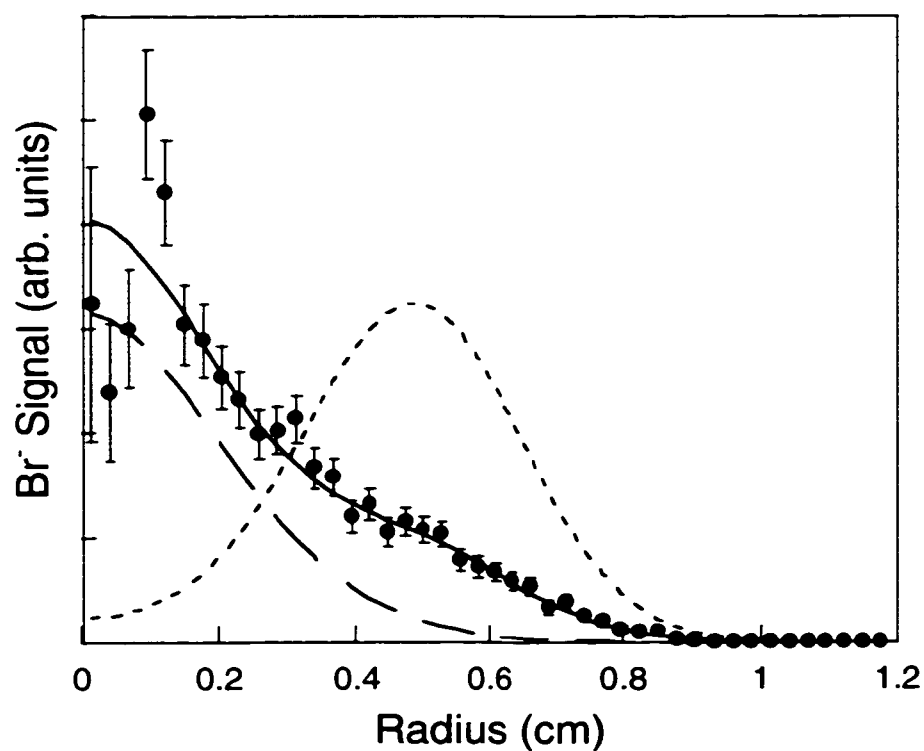
$$K(45p) + CBrCl_3 \rightarrow K^+ + CBrCl_3^{-*} \rightarrow K^+ + Cl^- + CBrCl_2 \tag{4.8}$$
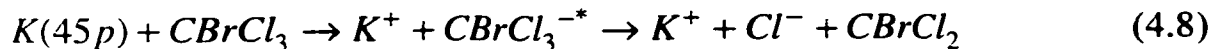
Figure 4.3   Radial distribution of Br⁻ ions produced in K(14p)/CBrCl₃ collisions. ● represents data including statistical error bars; the lines represent model calculations assuming: ---- (short dashes) Gaussian distribution with $\bar{\mathcal{E}}_G \sim 0.7$ eV and 75 meV standard deviation, ——— (long dashes) two-dimensional Boltzman distribution with $\bar{\mathcal{E}}_B \sim 0.15$ eV, solid line combines the other two calculations for a reaction channel ratio of ~30% short-lived/ 70% long-lived intermediate.
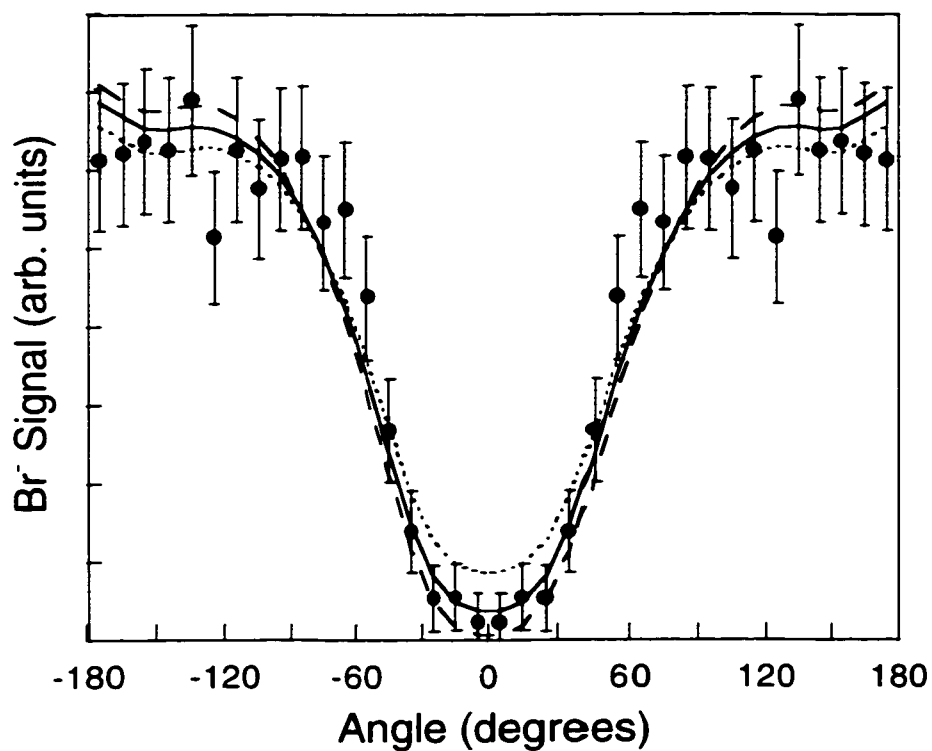
Figure 4.4   Angular distribution of Br⁻ ions produced in K(14p)/CBrCl₃
collisions. ● represents data including statistical error bars; the lines
represent model calculations assuming combinations of energy distributions
described by text and: ---- (short dashes) τ=10 ps, solid line τ=5 ps, — —
(long dashes) τ=0 ps.

but has only ~30% the signal strength of the Br⁻ product at room

temperature. The radial distribution of Cl⁻ ions from reaction 4.8 is presented

in figure 4.5. A single peak at small r comprises the distribution, indicating

one reaction channel with little translational energy release. This agrees well

with the calculations, which predict (see Table 4.1) that $D_0(CBrCl_2-Cl)$ is

much larger than $D_0(CCl_3-Br)$. Given that EA(Cl) is 3.61 eV the excess

energy, E $\lesssim$ 0.1 eV, is much less than that for Br⁻ production. If it is assumed

that the small r feature represents a reaction involving a long-lived

intermediate, as seen before, the data should be fit by a two-dimensional

Boltzman distribution. Figure 4.5 shows, however, that a two-dimensional

Boltzman distribution for any reasonable mean energy — expected to be

$\lesssim$ 0.03 eV — does not fit the data. Instead, the distributions assuming either

a Gaussian translational energy release of 75 meV FWHM centered on

$\bar{\varepsilon}_G$ ~ 0.075 eV or a rectangular translational energy release with

$\bar{\varepsilon}_R$ ~ 0.075 eV fit the data quite well. As before, a Gaussian distribution

implies that the intermediate ion associated with Cl⁻ production has a short

lifetime, insufficient to allow full statistical redistribution of the excess

energy of reaction. A rectangular distribution has no precise physical

interpretation but rather represents a transitional distribution between an

exponential two-dimensional Boltzman and a Gaussian. Thus, it is uncertain

under room temperature conditions whether dissociation leading to Cl⁻ is

immediate or if it occurs after a few vibrational periods. The Cl⁻ signal

produced in low-n collisions was very small and, therefore, insufficient to
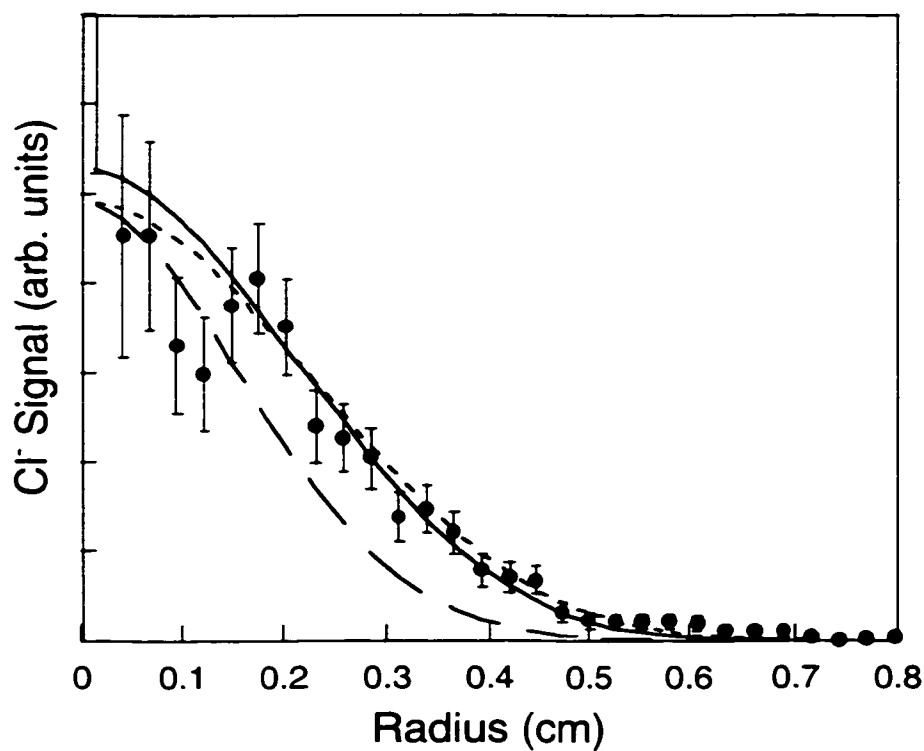
provide accurate ion angular distributions.

Figure 4.5   Radial distribution of Cl⁻ ions produced in K(45p)/CBrCl₃ collisions. ● represents data including statistical error bars; the lines represent model calculations assuming: —— (long dashes) two-dimensional Boltzman distribution with $\bar{\mathcal{E}}_B \sim 0.03$ eV, ---- (short dashes) Gaussian distribution with $\bar{\mathcal{E}}_G \sim 0.075$ eV and 75 meV standard deviation, solid line Rectangular distribution with $\bar{\mathcal{E}}_R \sim 0.075$ eV.

The reaction channels associated with K(np)/CBrCl$_3$ suggest a simple physical interpretation. The charge distribution of the parent negative ion seen in table 4.1 indicates that electron attachment is more likely to occur on the Cl site, but that there is a good probability for electron attachment at the Br site. Also from table 4.1, the Br atom has a lower bond dissociation energy and is, therefore, the more likely ion to detach. Considering this, suppose the electron attaches directly to the Br atom, immediate dissociation is likely to occur. If the electron attaches to the Cl atom it is also reasonable to expect rapid dissociation. The excess energy of reaction for Cl$^-$ production, however, is quite low, and recent studies suggest the presence of an energy barrier of ~50 meV for detachment of the Cl.[26] The energy barrier reduces the probability for direct Cl$^-$ dissociation thereby allowing the electron's energy to redistribute among internal motions. Br$^-$ production is favorable due to its weaker binding and eventually, enough energy can concentrate in a single Br bond to cause detachment. Such a process explains the long-lived reaction channel producing Br$^-$ ions. The energy barrier against detachment implies that Cl$^-$ production is highly dependent on the internal state, i.e. temperature, of the molecule. As the temperature of the CBrCl$_3$ molecules increases the ratio of Cl$^-$: Br$^-$ production is predicted to increase until a statistical distribution of 3:1 is achieved. Other studies observe this increase in signal for temperatures ~250° C.

Chapter 5
Non-Dissociative Targets

5.1 Introduction

Electron attachment does not always lead to dissociation of the intermediate. As discussed previously, the intermediate may decay by autodetachment or can be stabilized through a process called intramolecular vibrational relaxation (IVR), which will be discussed in detail later, leading to interactions of the form:

$$K(20p) + ABC \rightarrow K^+ + ABC^{-*} \rightarrow K^+ + ABC^-$$
$$\rightarrow K^+ + e^- + ABC$$

(5.1)
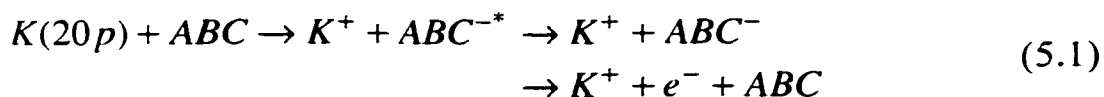
Studies involving non-dissociative targets are approached differently than the dissociative studies described previously. As before, the target molecule attaches the Rydberg electron through a binary interaction, and the resulting intermediate ion interacts with the Rydberg core via Coulombic attraction. After some time the intermediate ion either separates from the Rydberg core ion or undergoes autodetachment. Neither of these processes results in an anion signal providing useful information. The final distribution of the Rydberg core ion velocities, however, reflects the lifetime of the intermediate ion. Because the Rydberg atoms are formed in a beam, their forward momentum designates a preferred direction of travel. Therefore, the Rydberg atoms that either do not interact with a target, for example, those that are blackbody photoionized, or that interact with the target molecules for a very short period of time will be mostly unperturbed. The resulting cations maintain their forward momentum, striking the detector well ahead of the center of interaction. Their flight time in the mass spectrometer

determines the distance of travel seen on the detector. As with the dissociative targets, the longer the interaction between the intermediate ion and the Rydberg core the greater the perturbation of the core ion trajectories. This produces a more isotropic K^+ arrival position distribution at the PSD.

Two non-dissociative targets are studied, C_7F_{14} (perfluoromethylcyclohexane) and C_6F_6 (hexafluorobenzene). The experimental techniques used for each are different due to the different reaction characteristics. Data for C_7F_{14} are recorded in coincidence, as described for the dissociative targets, but the same technique is inappropriate for C_6F_6. The following chapter describes the experimental approach for each target.

5.2 C_7F_{14} Experiment

The reaction between C_7F_{14} and potassium Rydberg atoms results in two negative products, $C_7F_{14}^-$ and free electrons via:

$$K(20p) + C_7F_{14} \rightarrow K^+ + C_7F_{14}^{-*} \rightarrow K^+ + C_7F_{14}^-$$
$$\rightarrow K^+ + e^- + C_7F_{14}$$

(5.2)
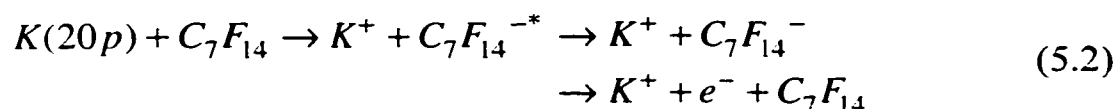
These experiments, like the dissociative studies, operate in a pulsed mode. However, a small DC bias field of ~ 1 Vcm^{-1} is constantly applied in order to draw out all electrons present before the extraction pulse. The small bias field is insufficient to extract the heavier ions in a timely fashion so an extraction field of ~ 5 Vcm^{-1} is pulsed on after a short delay. In the absence of such an extraction pulse, the K^+ and $C_7F_{14}^{-*}$ ion flight times through the mass spectrometers are sufficiently long that the transverse velocity (in the x-y plane of figure 2.1) of the ions causes them to miss the PSD. The

additional extraction voltage decreases their flight times and minimizes the losses off the PSD. The extraction voltage of ~5 Vcm^{-1} is chosen to maximize the K$^+$ flight time, while minimizing the losses. With a voltage on the top drift region of -13 V, the K$^+$ ions arrive at the detector after a drift time of approximately 27 μs. This allows adequate time for the K$^+$ position distribution to fill much of the detector, making its essential features easily recognizable.

The timing for this experiment is set up to maximize the signal strength while maintaining localization of the reactants during the interaction. The signal strength depends on the attachment rate constant, the pressure of the target gas in the chamber, and the number of Rydberg atoms available for interaction. The rate constant for attachment is an intrinsic characteristic of each particular target gas. The maximum operating pressure of the vacuum system limits the target gas pressure, and the power of the laser, as well as, the length of the laser pulse determines the number of Rydberg atoms available. Maximizing these variables will, therefore, maximize the signal strength. Keeping the reaction localized requires minimizing the total amount of time the target and Rydberg atom interact, i.e. the time from the beginning of the laser pulse to the beginning of the extraction pulse. Both the laser pulse length and the delay time between the laser pulse and the extraction ramp are experimentally adjustable parameters.

In this experiment, the laser pulse width is 1 μs and the extraction pulse begins immediately after the laser pulse ends. The attachment rate for perfluoromethylcyclohexane is ~6·10^{-8} cm^3 s^{-1},[27] a factor of two lower than that of C$_6$F$_6$. The laser power is adjustable up to some daily maximum value — typically ~2-3 mW in the ultraviolet wavelengths used for Rydberg

excitation. Using a 1 μs laser pulse instead of the typical 0.5 μs laser pulse maximizes the signal strength. A longer laser pulse would increase the number of interactions, but diminish the localization of the reactants. The delay before the extraction pulse is set to zero. This preserves the same total interaction time, 1 μs, for each of the non-dissociating targets.

5.3 C_7F_{14} Analysis

Before comparing the final data set with the model, several corrections must be made. The data are taken in coincidence, as described for the dissociative targets, to ensure that the products recorded result from the reactions of interest. However, the background signal due to blackbody photoionization of the Rydberg atoms must be subtracted from the data, which include ion signals due to both Rydberg atom collisions with the target, as well as interactions with the blackbody radiation. The K^+ signal recorded in coincidence with the $C_7F_{14}^-$ ions will be unaffected by the background signal, but those reactions that produce electrons as a product will be indistinguishable from a blackbody photoionization event. In order to correct for the background signal, data sets are recorded with gas-in and with gas-out in immediate succession. Several sets of gas-in/gas-out measurements are subsequently summed to create the entire data set.

The gas-in measurements are conducted with a C_7F_{14} pressure of $\sim$2.0·10^{-5} Torr, as measured by the Bayard-Alpert ion gauge. The actual gas pressure corresponds to the ion gauge pressure multiplied by a sensitivity factor, which accounts for the ionization efficiency of a particular gas. For C_7F_{14} the sensitivity factor is $\sim$0.15, which implies the actual gas pressure is $\sim$3.1·10^{-6} Torr.

The gas-out measurements require further correction before subtraction from the data. One correction factor incorporates the ratio of the number of laser shots used with gas-in to those used with gas-out, typically 25:6 gas-in to gas-out. Due to statistical inconsistencies, i.e. several data points equaling zero, the ratio cannot be used as a simple multiplicative factor for each individual datum point in the background data. Instead, the average value of the background signal must multiply the ratio and then add to the original gas-out data points, thereby raising the average value of the background by the correction factor. This method is legitimate only when a constant background signal is expected and, therefore, applies only after extraction is complete. The analysis windows are chosen to include only data during the peak extraction voltage, thereby ensuring accurate background correction.

The introduction of target gas into the reaction chamber also disperses the potassium beam such that the beam density is reduced and consequently so is the Rydberg atom production rate. Thus, the actual number of background counts is lower with gas-in than with gas-out. To determine the difference from one condition to the other, the hotwire detector is used to monitor the potassium beam density under both conditions. With a C_7F_{14} gauge pressure of $\sim 2.0 \cdot 10^{-5}$ Torr, the hotwire measures a current of 0.875 nA, and with no gas the hotwire detector reads 1.2 nA. The operation of the hotwire has been described previously, but here it is important to remember that the hotwire current is directly proportional to the beam number density. The hotwire measurement overestimates the actual effect, however, since the distance the beam travels through the gas is a crucial factor in how much attenuation occurs. The distance from the beam-defining aperture to the center of the interaction region is significantly less than the

distance to the hotwire. To extrapolate back to the dispersion in the interaction region one must consider the exponential factor for dispersion of a gas.

The isometric expansion of the potassium beam without another gas present relates the number density at the hotwire, n_{HW}, with the number density at the interaction region, n_{IR}.

$$n_{HW}(r_{HW})^2 = n_{IR}(r_{IR})^2 \tag{5.3}$$

where r_{HW} and r_{IR} are distances from a known point to the hotwire and interaction region, respectively. This gives:

$$n_{IR} = \left(\frac{r_{HW}}{r_{IR}}\right)^2 n_{HW} \tag{5.4}$$

The exponential decay due to the dispersion of the beam by a gas is given by:

$$
\begin{aligned}
n'_{IR} &= n_{IR} \cdot e^{-\frac{r_{IR}}{\lambda}} \\
n'_{HW} &= n_{HW} \cdot e^{-\frac{r_{HW}}{\lambda}}
\end{aligned}
\tag{5.5}
$$

The primed variables indicate the values with gas-in, and λ is the mean free path of the potassium atoms. Substitution of equation 5.5 into 5.4 yields:

$$n'_{IR} \cdot e^{\frac{r_{IR}}{\lambda}} = \left(\frac{r_{HW}}{r_{IR}}\right)^2 n'_{HW} \cdot e^{\frac{r_{HW}}{\lambda}} \tag{5.6}$$

Take the ratio of equation 5.6 to equation 5.4 in order to incorporate the two measured values of n_{HW} and n'_{HW}.

$$\frac{n'_{IR}}{n_{IR}} = \frac{\left(\frac{r_{HW}}{r_{IR}}\right)^2}{\left(\frac{r_{HW}}{r_{IR}}\right)^2} \frac{n'_{HW}}{n_{HW}} \cdot e^{\frac{(r_{HW}-r_{IR})}{\lambda}} \tag{5.7}$$

which equals

$$\frac{n'_{IR}}{n_{IR}} = \frac{n'_{HW}}{n_{HW}} \cdot e^{\frac{(r_{HW}-r_{IR})}{\lambda}} \tag{5.8}$$

r_{HW} and r_{IR} are determined from the physical dimensions of the vacuum system.

$r_{HW} = 24.6$ cm
$r_{IR} = 9.5$ cm
$r_{HW} - r_{IR} = 15.1$ cm $= 0.151$ m

Further, the kinetic theory of gases gives:

$$\lambda = \frac{1}{\rho\sigma\sqrt{2}} \tag{5.9}$$

where ρ is the gas density and σ is the molecular collision cross-section. Assuming an ideal gas,

$$\rho = \frac{P}{kT} \tag{5.10}$$

where P is the gas pressure, T the temperature, and k is Boltzman's constant. The density, therefore, of C_7F_{14} at a pressure of $\sim3.1\cdot10^{-6}$ Torr and at room temperature (~300 K) from equation 5.10 equals $\sim9.9\cdot10^{10}$ cm^{-3}. Assuming a molecular radius of ~10 Å, the molecular collision cross-section:

$$\sigma = 4\pi r^2 \tag{5.11}$$

for C_7F_{14} equals $\sim 1.25 \cdot 10^{-13}$ cm^2. Using the values of ρ and σ in equation 5.9 gives a mean free path of ~ 0.57 m. Further substitution into equation 5.8:

$$e^{\frac{(r_{HW} - r_{IR})}{\lambda}} = e^{\frac{(0.151\ m)}{(0.568\ m)}} = 1.3$$

$$\frac{n'_{IR}}{n_{IR}} = \frac{n'_{HW}}{n_{HW}} \cdot e^{\frac{(r_{HW} - r_{IR})}{\lambda}} = \frac{0.875\ nA}{1.2\ nA} \cdot 1.3 = 0.95 \tag{5.12}$$

This becomes a second correction factor for the background counts. The final corrected values are shown in figure 5.1.

Figures 5.1a and 5.1b show graphs of ion signal versus time of flight for the K^+ ions and for the anions/electrons produced in $K(20p)/C_7F_{14}$ collisions, respectively. Both gas-in and corrected gas-out measurements are shown, and the vertical lines indicate the windows used to analyze the data. It is important to explain the representation of the data in figure 5.1 to further clarify the operation of the experiment.

Four important issues affect the presentation seen in figure 5.1: 1) the extraction pulse lasts for ~ 20 μs, 2) the data are taken in coincidence, 3) the Quad Event Timer (QET), which reads the timing of the ions, cannot record events occurring > 40 μs after its initiation, and 4) the time of flight for the K^+ ion must be as long as possible, ~ 27 μs, to see the characteristic features. With these four points in mind, observe the data in figure 5.1a, representing the K^+ signal. It shows a sharp turn on of signal at ~ 27 μs, corresponding to the extraction ramp plus the time of flight, followed by a constantly decreasing signal up to ~ 40 μs, the limit of the QET. The slow decrease in the signal corresponds to the lifetime, τ', of the Rydberg state, which is a function of the radiative lifetime at $n = 20$ and of the decay rate due to interactions with the target gas.

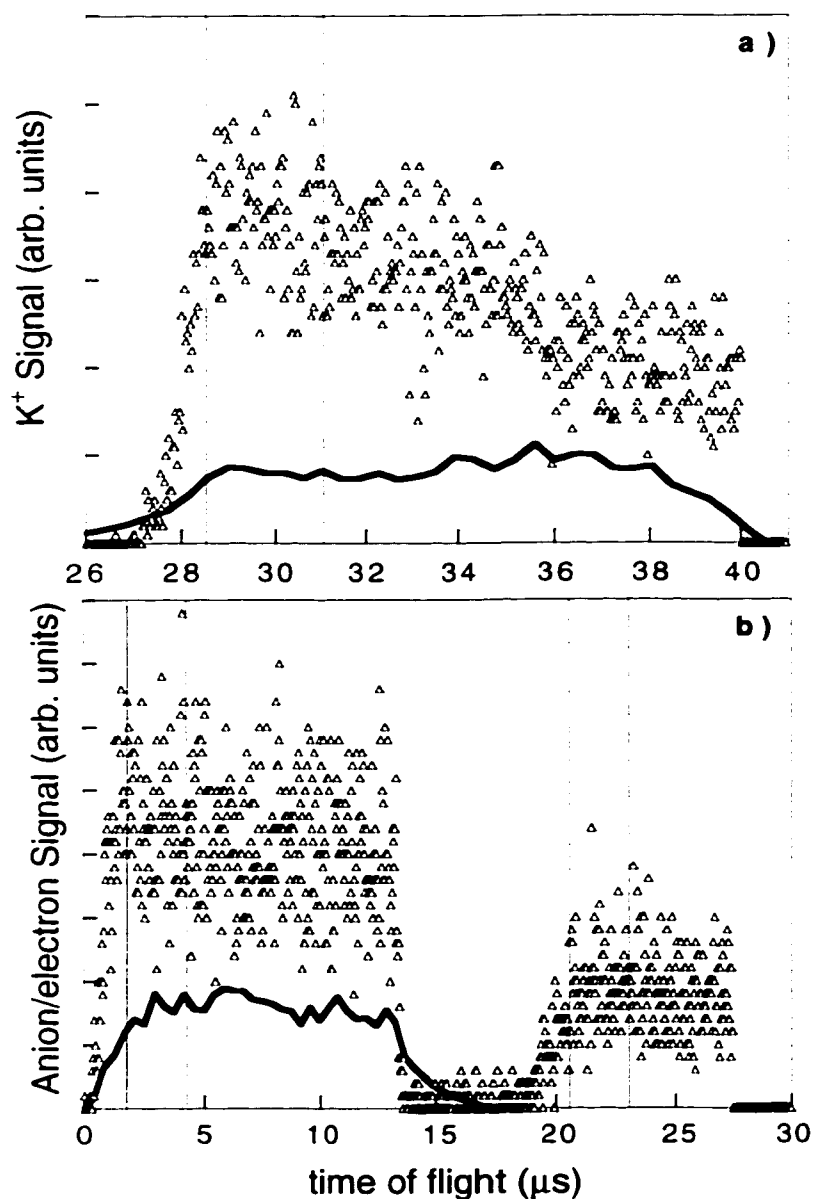**Figure 5.1** Ion signal vs. time of flight for products - (a) K^+, (b) anion - of $K(20p)/C_7F_{14}$ collisions. Δ represents data; solid lines represent corrected and smoothed background signal. Vertical lines represent analysis windows (see text).

Figure 5.1b is a bit more complicated. The first signal from 0 μs to ~13 μs corresponds to free electrons resulting from either blackbody-Rydberg atom interactions or from autodetachment of $C_7F_{14}^-$ ions. Though the extraction pulse lasts for 20 μs, the electron signal is only 13 μs long. This is due to the fact that the data is taken in coincidence and the corresponding K^+ signal can only be recorded for 13 μs due to the QET limitations. The second signal in figure 5.1b represents the long-lived $C_7F_{14}^{-*}$ ions. The mass spectrometer is set up to give the product anions a time of flight of ~20 μs in order to avoid the initial free electron signal as well as to avoid the secondary electron signal produced when the K^+ ions strike the top detector. The analysis windows are chosen such that the signal used does not overlap the secondary electron signal at all. Notice that there is no background signal during the $C_7F_{14}^-$ signal; this is a result of taking data in coincidence as mentioned for dissociative targets.

Analysis requires comparing the experimental position distribution data with distributions obtained using the model described in Chapter 3. The center of interaction for the data, however, does not match that of the model. The model records position data on a 128 x 128 grid, assuming the center to be at the coordinates (64,64). In the actual experiment, the effective center depends on the physical intersection point of the laser beam and the K-beam in relation to the center on the position sensitive detector (PSD). This location changes slightly each time the potassium alkali oven is removed. For analysis, even minute differences of the center location between experiment and model affect the final conclusions. Thus, two separate methods are used to correct the center of the data with respect to the true center of the PSD. Both methods utilize the fact that photoionization occurs immediately and does not perturb the K^+ core ion momentum. This implies

that the distance traveled along the original direction of the K-beam during the ion's flight time is a simple product of the ion's velocity and its time of flight. The velocity transverse to the forward direction of the beam is due to a thermal energy distribution of the beam centered about the interaction location so the center in the laser direction is determined directly from the recorded distributions.

The first method determines the correct interaction location by using the final K^+ position distribution recorded with gas-out. Figure 5.2a shows K^- signal strength vs. position along the K-beam, and 5.2b shows K^+ signal strength vs. position along the laser beam. The positions are shown in channels, assuming the total diameter of the PSD is 128 channels. Also in figure 5.2, the data are normalized and fit with a Gaussian distribution of the form:

$$f(X) = \frac{1}{\sqrt{2\pi\sigma}} e^{-\frac{(X-\bar{X})^2}{2\cdot\sigma}}$$

(5.13)

Because there is no initial velocity in the direction of the laser beam the center of the Gaussian fit represents the transverse position (in the y direction as defined by figure 2.1) within the interaction volume. The initial velocity in the K-beam direction is chosen by velocity selection of the Rydberg atoms, via Doppler tuning, to be 350 m s^{-1} in this experiment. A computer program calculates the time of flight of the ions. It uses the voltages measured from each power supply as parameters and computationally accelerates or drifts the ions through the appropriate series of fields until reaching the detector. The program does not take into account the ramp of the extraction pulse so the values may be slightly smaller than the actual flight time. Such error is, however, quite small in comparison to
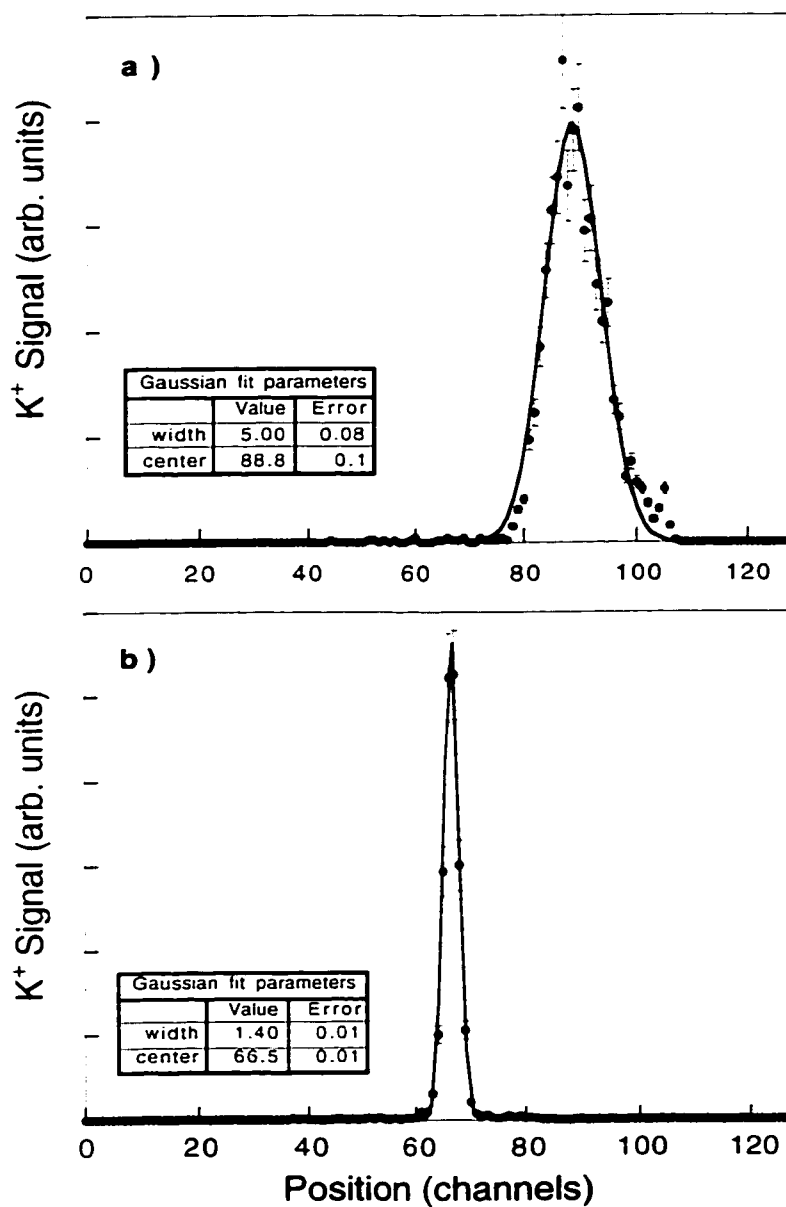
a)

K⁺ Signal (arb. units)

Gaussian fit parameters		
	Value	Error
width	5.00	0.08
center	88.8	0.1

0   20   40   60   80   100   120

b)

K⁺ Signal (arb. units)

Gaussian fit parameters		
	Value	Error
width	1.40	0.01
center	66.5	0.01

0   20   40   60   80   100   120

Position (channels)

Figure 5.2   K⁺ signal vs. position – a) along K-beam, b) along laser beam – for K⁻ ions produced via blackbody photoionization. ● represents data with statistical error bars; solid line is a Gaussian fit to the data with the parameters shown.

the errors in other values; full error propagation will be explained shortly.

The time of flight measured by the QET exceeds the ion's actual flight time, because the QET measures time from initialization until it receives a stop signal, incorporating several electronic delays, which should not be included in this calculation. For the voltages used in this experiment the calculated time of flight equals ~26.8 μs for the K^+ ions. The distance traveled in the x-direction, as defined in figure 2.1, during the time of flight, therefore, equals:

$x = v \times t = 350 \times 26.8 \cdot 10^{-6} = 9.4 \cdot 10^{-3}$ m ≈ 30.1 channels

using a conversion factor of 32 channels = 1 cm. Subtracting this from the center of the Gaussian fit provides the original interaction location:

88.8 channels − 30.1 channels = 58.7 channels

Together, the total center is defined as (58.7, 66.5) — see the fits shown in figure 5.2. Since the model assumes a center at (64,64), the experimental data must be shifted by:

$$\text{data points} = (x + 5.3, y - 2.5) \tag{5.14}$$

where (x,y) are the original experimental data points, for appropriate comparison.

Propagating error through this calculation also summarizes the process nicely.

$$D = 64 - (c - 3200 \cdot v \cdot t) \tag{5.15}$$

$D \equiv$ change in data points
$64 \equiv$ model's assumed center in channels
$c \equiv$ center from Gaussian fit to data
$3200 \equiv$ conversion factor from meters to channels
$v \equiv$ velocity chosen using velocity selection
$t \equiv$ calculated time of flight

Each variable has associated with it some error, i.e. $c \pm \delta c, v \pm \delta v, t \pm \delta t$.

Thus, error propagation gives:

$$\delta D = \sqrt{\left(\frac{\partial D}{\partial c}\delta c\right)^2 + \left(\frac{\partial D}{\partial v}\delta v\right)^2 + \left(\frac{\partial D}{\partial t}\delta t\right)^2} \qquad (5.16)$$

and when applied to equation 5.15:

$$\delta D = \sqrt{(-1 \cdot \delta c)^2 + (3200t \cdot \delta v)^2 + (3200v \cdot \delta t)^2} \qquad (5.17)$$

Error in the center, δc, is found as a parameter in the Gaussian fit. Error in velocity, δv, is determined from the most recent calibration measurements of the apparatus, and any error introduced by the calculated time of flight, δt, cannot be specifically quantified but should be $\lesssim 10\%$. The calculated values do not differ from the experimental values for either non-dissociative target by more than 10%. For C_7F_{14} :

$$\begin{aligned} c &= 88.8 \pm 0.1 \text{ ch} \\ v &= 350. \pm 45 \text{ m/s} \\ t &= 26.8 \pm 2.7 \ \mu\text{s} \end{aligned} \qquad (5.18)$$

giving

$$\delta D = 4.90 \text{ ch}$$

which means that the center of the data for collisions with C_7F_{14} can change by 5.3 +/- 4.9 ch in the K-beam direction. Along the laser beam direction, the center and standard deviation determined by the Gaussian fit seen in figure 5.2b are appropriate since the transverse velocity results only from a Maxwell-Boltzman distribution of the gas molecules at room temperature.

The second method for determining the shift in the experimental center uses the same principles as the first, but it makes a direct comparison between the data and the model calculations rather than backtracking through the data. If the model assumes parameters corresponding to a blackbody interaction with K^+, the peak of the calculated K^+ distribution should coincide with that of the K^+ data taken with gas-out. The parameters specifying such a condition do not differ from those assuming an immediate autodetachment, $\tau = 0$, of an electron from a $C_7F_{14}^{-*}$ ion. In either case, the motion of the K^+ remains unperturbed. Figure 5.3 shows the uncorrected K^+ data and the model calculations for the parameters described. The difference in the centers is obviously ~10 channels, which is within the range of error for the first calculation method. This being true, the data are modified by alignment with the model values, using the second method.

Once the data has been corrected for the background and adjusted for the center, the next step toward analysis is comparison with the model calculations. For correct comparison the model must use the appropriate parameters for the experiment under consideration. In the case of $K(20p)/C_7F_{14}$ collisions, two negative products result from the interaction: $C_7F_{14}^-$ anions and free electrons. A simple electron attachment process with no dissociation mechanism models the ion signal. The free electron signal, conversely, may result from a number of different processes: direct collisional ionization of a Rydberg atom by the C_7F_{14} molecules; collisional excitation to a higher Rydberg state, which is subsequently ionized by the 6 Vcm^{-1} extraction field; or an autodetachment process in which the electron binds to the C_7F_{14} and then detaches after a short period of time. Earlier work indicates that the ionization processes would most likely involve the
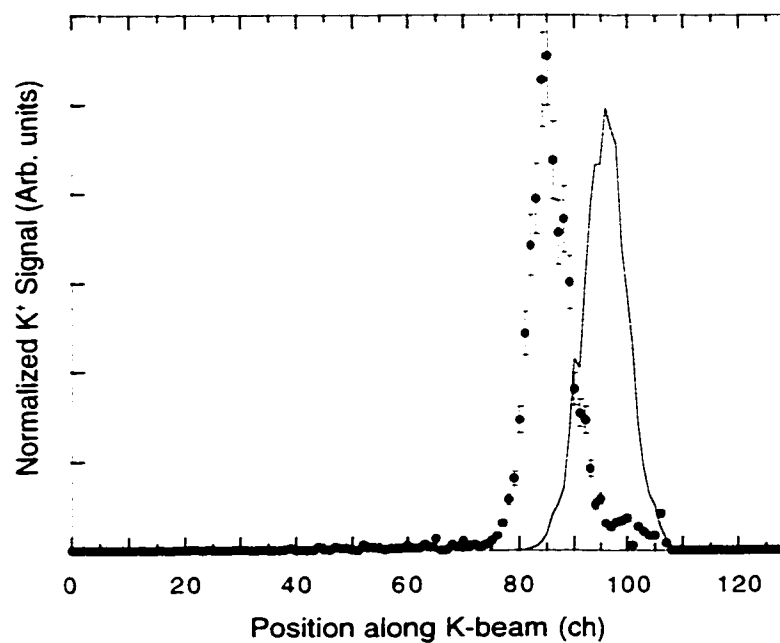
Figure 5.3 K$^+$ signal due to blackbody photoionization vs. position along the K-beam. ● represents uncorrected data with statistical error bars; solid line represents model calculations with parameters described in text.

transfer of rotational energy from the target molecule through a dipole-allowed J→J-1 transition.[28] Also, according to previous studies,

> "...collisions [between potassium Rydberg atoms and C_7F_{14} molecules] do not populate states of higher n at an appreciable rate. Thus it is unlikely that the observed free electron signal results from ionization caused by collision-induced transfer of molecular rotational energy because this process is typically accompanied by collisional population of groups of Rydberg states of higher n." [29]

In order to verify the previous results, and also because the earlier studies were performed at much higher n-values ($30 \leq n \leq 110$), selective field ionization experiments were repeated for both K(20p) and K(30p) atoms. In these experiments, K(np) Rydberg atoms interact with the C_7F_{14} for a period of time before a large ramped field, up to ~800 Vcm^{-1} is applied. This field is sufficient to ionize Rydberg states with $n \gtrsim 28$. Both experiments, for K(20p) and for K(30p), agreed with the previous results. C_7F_{14} produces a small amount of n-changing but not enough to account for the free electron signal observed.

Additional examination of the possibility of rotational energy transfer utilizes calculations based on the local-spin-density approximation of the density functional theory. A molecule must have a permanent dipole moment to exhibit electric-dipole pure-rotation transitions. The calculated dipole moment for C_7F_{14} is ~0.2 Debye, which is in good agreement with other studies that determined a near-zero dipole moment using liquid C_7F_{14}.[30] Though the dipole moment is small, assume that a pure-rotation transition is possible. The calculated moments of inertia are given below, along with the rotational constants, which are related to the moments of inertia by

$$A, B, C = \frac{h}{8\pi^2 I_{a,b,c}}$$

(5.19)

$I_a = 1.02 \cdot 10^3$ AMU Å^2 A=2.05 μeV

$I_b = 1.52 \cdot 10^3$ AMU Å^2 B=1.37 μeV

$I_c = 1.86 \cdot 10^3$ AMU Å^2 C=1.12 μeV

Because A≠B≠C, C_7F_{14} can be considered an asymmetric top. The allowed transitions for an asymmetric top are given by $\Delta J = 0, \pm 1$, and $\Delta M = 0, \pm 1$, because K is not a good quantum number. However, K is split into two unofficial quantum numbers, K_{pr} and K_{ob}, which represent the amount of K quantum number associated with a prolate or an oblate symmetric top respectively. K_{pr} and K_{ob} can change in steps of two, either even or odd depending on the orientation of the dipole. Ray's asymmetry parameter is a further description of the geometry of the molecule and is given by:

$$\kappa = \frac{(2B-A-C)}{(A-C)}$$

(5.20)

This value correlates how the symmetry changes from an oblate top, where A=B≠C and κ=1, to a prolate top, where A≠B=C and κ=-1. For C_7F_{14} $\kappa = -0.457$ which implies that C_7F_{14} can be classified as a nearly prolate symmetric top, for which the most likely transitions are for $\Delta K_{pr} = 0, \pm 1$.

The exact solution of the energy eigenvalues for an asymmetric configuration is extremely complicated, so the exact solution for the case of a prolate top is used instead:

$$E(J, K) = h \cdot \left[B \cdot J(J+1) + (A - B)K^2 \right]$$

(5.21)

where J = 0,1,2,... and K = -J, ..., +J. For a true prolate B=C, so the B used in the case of C_7F_{14} is an average of B and C, (B+C)/2. The energy needed to

ionize the Rydberg state must be equivalent to the difference in energy between the original state of the molecule and the final state.

$$E_{ionization} = E(J, K) - E(J - i, K - i) \qquad (5.22)$$

where i represents the number of levels changed. Substituting equation 5.21 into 5.22 and solving for K gives the following:

$$K = \frac{E_{ion} - i \cdot [B \cdot (2J + 1) - A \cdot i]}{2 \cdot i \cdot (A - B)} \qquad (5.23)$$

Though the most likely transitions occur for i = 1, transitions are possible for any i value up to the total values of J and K. A K(20p) Rydberg atom requires 34 meV of energy for ionization. The rotational constants for C_7F_{14}, shown after equation 5.19, are three orders of magnitude smaller than this value, which implies that ionization will be difficult for small ΔJ transitions. Figure 5.4 plots K as a function of J, assuming several different values of i, for transitions sufficient to ionize K(20p) atoms. Note that ionization occurs for J→J-1 transitions only for states with J $\gtrsim 10^4$. For a J→J-10 transition to lead to ionization requires an initial J>10^3. The J state population distribution, given by a Maxwell-Boltzman distribution of the form:

$$P(J, K) = P_0 \cdot e^{\frac{-E(J,K)}{kT}} \qquad (5.24)$$

for a room-temperature gas peaks at J~100 and falls to only a few percent occupation for J>10^3.

Other than directly ionizing, rotational transitions can excite the Rydberg atoms into an n-state high enough to be ionized by the applied field of ~6 Vcm^{-1}. Only potassium Rydberg atoms in states of n $\gtrsim$ 86 will ionize

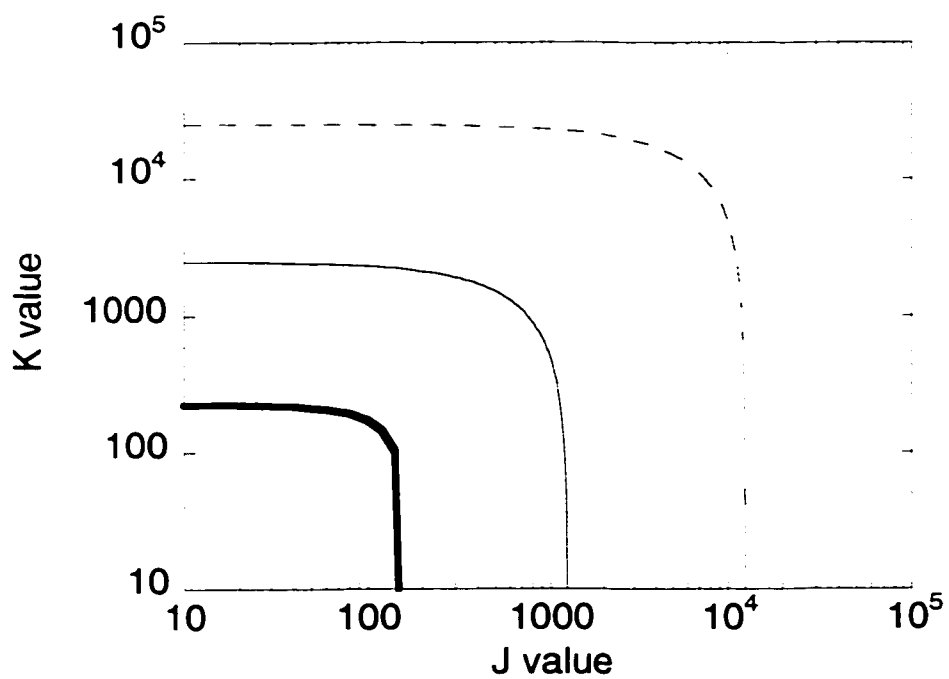**Figure 5.4**   K vs. J for transitions sufficient to ionize K(20p) atoms. The lines represent ----- J → J-1 transition, ——— J → J-10 transition, ▬▬ J→ 0 transition.

in such a small field. An energy of ~32 meV is needed to excite a Rydberg transition from n = 20 to n = 86. As before, the rotational constants are much smaller than this value, and the same arguments suggest that there is little probability of pure-rotational transitions leading to either ionization or to n-changing. Evidence, therefore suggests that the recorded free electron signal must originate in an autodetachment process from the $C_7F_{14}^{-*}$ intermediate ion, and the reaction is modeled as such.

Neither the form of the energy distribution nor the mean energy of the detached electron is known. Assuming an autodetachment process, however, implies that some amount of energy redistribution within the intermediate ion is likely to occur. This process can be represented by an exponential distribution with mean energy, $\bar{\varepsilon}$. Typically, energy redistribution does not occur during instantaneous processes like blackbody photoionization, but even short-lived interactions (τ ~10 ps) are of sufficient length to allow for some of the excess energy to be redistributed among the various vibrational and rotational modes of the molecule. Though the mean energy, $\bar{\varepsilon}$, is unknown, tests indicate that the final K^+ ion arrival position distribution is not sensitive to the exact value, at least for $\bar{\varepsilon} \gtrsim 20$ meV. The mean kinetic energy of the Rydberg electron at n = 20 is ~40 meV, and the target, C_7F_{14}, is at room temperature, which gives it an energy of kT ~26 meV. It is, therefore, reasonable to assume that $\bar{\varepsilon}$ will be greater than 20 meV. The model calculations are run using an exponential energy release distribution with a mean energy, $\bar{\varepsilon} = 30$ meV.

Figure 5.5 shows density plots of the experimental data, corrected for both the background and the interaction/center location, as compared with model calculations covering a range of lifetimes from $\tau = 0$ ps to $\tau =$ infinite. Figure 5.5 demonstrates very clearly the effect of the intermediate ion

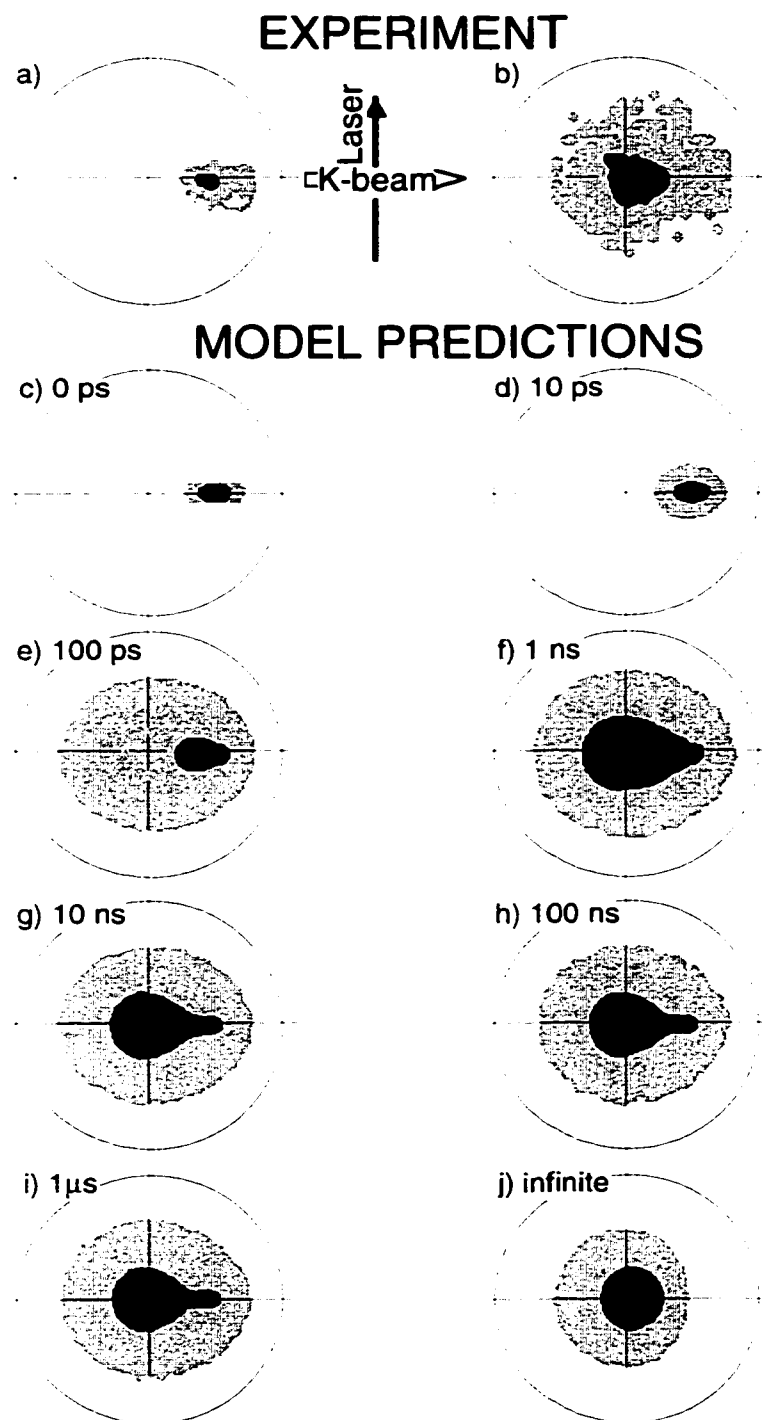**Figure 5.5** Density plots of K^+ ions formed in $K(20p)/C_7F_{14}$ collisions. Density of signal increases from lighter to darker shades. a) K^+ data measured in K^+/e^- coincidence; b) K^+ data measured in K^+/C_7F_{14} coincidence; c)-j) model calculations assuming an exponential translational energy release distribution centered on $\bar{\varepsilon} = 30$ meV and with τ shown.

lifetime on the K^+ arrival position distribution. The top row of figure 5.5 shows experimental data: K^+/free electron coincidence on the left and K^+/C_7F_{14} coincidence on the right. All subsequent distributions are model calculations assuming the lifetimes shown. As described previously, very short-lived intermediates do not significantly perturb the initial K^+ trajectory, and, as is obvious in the model distributions for $\tau \leq 10$ ps, the K^+ ions arrive at the detector well forward (along the direction of the K-beam) of center. As the lifetime increases, the arrival distribution spreads out, and the center of the distribution retreats toward the center of the detector.

Very little changes in the distribution in the range 10 ns $\leq \tau \leq 10$ μs, and the distribution center is even slightly backward of the detector center. The consistency within this time range is not surprising. The orbital period of the intermediate anion/Rydberg core complex is $\gtrsim 100$ ps. Therefore, for intermediate ion lifetimes $\gtrsim 10$ ns, bound ion pairs will orbit several times prior to detachment. This causes the velocity distribution of the K^+ product ions, in the center of mass frame, to become, in essence, isotropic when averaged over numerous interactions. Unbound K^+/intermediate ion pairs, at longer times, will be separated sufficiently to make their remaining electrostatic interactions weak and the scattering complete. In either case, further increases in intermediate lifetime, i.e. $\gtrsim 10$ ns, will not affect the final K^+ distribution. After 10 μs, however, the distribution center begins to move forward following the center of mass of the $K^+/C_7F_{14}^{-*}$ orbiting system. Due to an increased probability for product ions (from bound pairs) travelling backward to escape the electrostatic attraction between the K^+ core and the product electron, the distribution peaks backward of center. Finally, the case of infinite lifetime represents a system where neither dissociation nor autodetachment occurs. The distribution, therefore, consists of only products

from interactions that begin on hyperbolic orbits, i.e. the K^+ and $C_7F_{14}^{-*}$ are never bound.

Comparing experiment to model predictions shows that the autodetachment process leading to the free electron signal is rapid, while the process leading to $C_7F_{14}^{-*}$ involves a long-lived intermediate. Figure 5.6 shows another view of the same data and elucidates the conclusions further. The signal in the plots of figure 5.5 is integrated along the laser beam axis, and the resulting sum is plotted versus distance along the K-beam axis. Figures 5.6a and 5.6b correspond to the K^+ distributions coincident with the free electron and the $C_7F_{14}^-$ signals, respectively, and include several model calculations for comparison. In addition, the detector center is marked on each graph by an arrow. The same characteristics are visible in both figures 5.5 and 5.6. Clearly, the free electron process must have a lifetime greater than 0 ps, for the spread of the data seen in figure 5.5 exceeds that of the 0 ps model. Figure 5.6a shows that the spread is less than that expected for a 15 ps lifetime, however. The longer-lived ion data appears to have the same general isometry as the model calculation for an infinite lifetime. However, upon closer examination, particularly apparent in figure 5.6b, the data are peaked somewhat more in the forward direction than predicted for either an infinite lifetime or lifetimes $\gtrsim 1$ ns.

Additional experiments were performed to investigate the lifetime of the long-lived $C_7F_{14}^-$ product. The ion signal was measured as a function of flight time to the detector. Adjusting the various voltages along the TOFMS varies the flight time; however, care must be taken to ensure that the detection efficiency remains constant for each set of conditions. This is accomplished by maintaining the same ion impact energy on the PSD for each case. Initial studies using SF_6 gas as the target proved the method
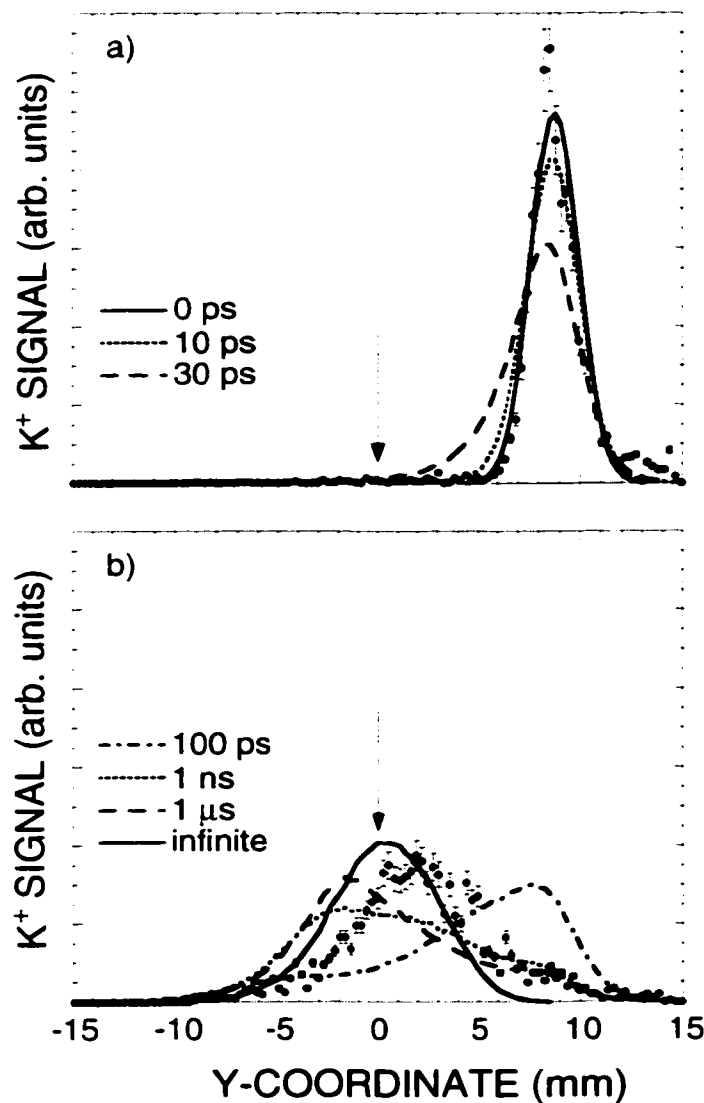
Figure 5.6 K$^+$ signal vs. position for ions produced via K(20p)/C$_7$F$_{14}$ collisions. a) K$^+$ coincident with free electrons b) K$^+$ coincident with C$_7$F$_{14}^-$. • represent data with statistical error bars; lines represent model calculations assuming an exponential translational energy release distribution centered on $\bar{\varepsilon}$ = 30 meV and with τ shown.

reliable. SF_6^{-*} ions formed in Rydberg atom collisions are known to have very long lifetimes ($\gtrsim 1$ ms) against autodetachment.[31] Figure 5.7 shows ion signal versus flight time for both SF_6^- and $C_7F_{14}^-$. The SF_6^{-*} ion signal shows no significant change over the range of flight times from 5 to 35 μs. The results for $C_7F_{14}^-$ also indicate very little change over the same range, and the data point to a lifetime > 100 μs, which is consistent with earlier work using thermal energy free electron attachment and indicating a $C_7F_{14}^-$ lifetime of ~0.8 ms.[8]

Though the excess signal in the forward direction is consistent with the model predictions for 10 ns $\lesssim \tau \lesssim 1$ μs, it is unlikely that the signal results from an intermediate with a lifetime in this range. If autodetachment occurs on this time scale no anion would be detected and the K^+ would be seen in coincidence with a free electron. The inconsistency between the data and the model predictions can be explained by post-attachment interactions in which internal energy of the $C_7F_{14}^-$ ion is transferred to translational motion of the $K^+/ C_7F_{14}^{-*}$ pair. The energy transfer to translation of the system causes a larger number of ion pairs, which would otherwise be bound, to separate. The occurrence of post-attachment energy transfer is consistent with previous studies.[29] This earlier work involved rate constant measurements over a range of principal quantum numbers, $30 < n < 110$, and the rate constant for ion formation was observed to remain constant throughout the entire range. The model, however, suggests a sharp decrease over the same range. Figure 5.8 shows rate constant versus principal quantum number for both the model and the experiment. Obviously, the experimental data demonstrate much higher escape probabilities at lower n than the model predicts. This implies that there is energy transfer occurring, which is more likely at lower n-values where post-attachment interactions

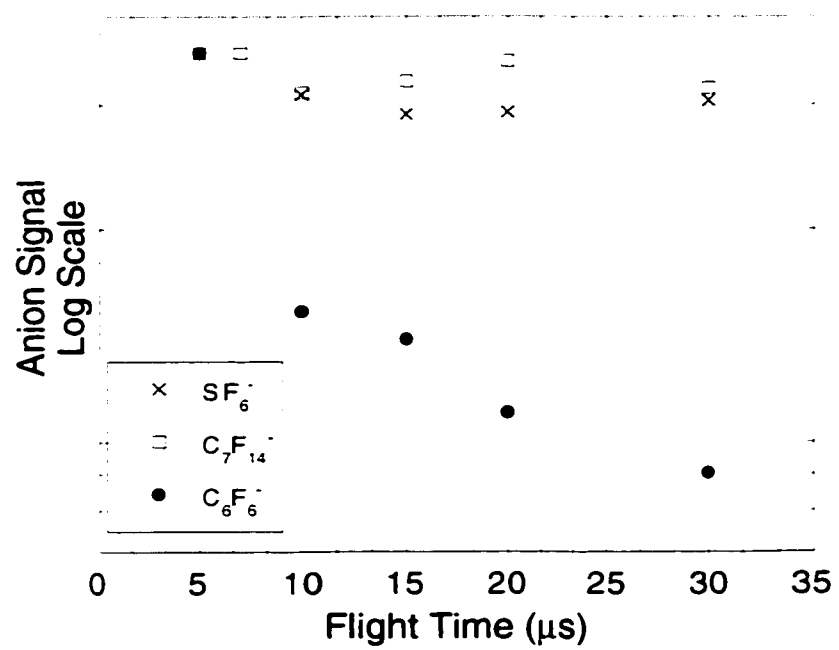**Figure 5.7**   Ion signal vs. flight time for SF_6^-, $C_7F_{14}^-$, and $C_6F_6^-$.
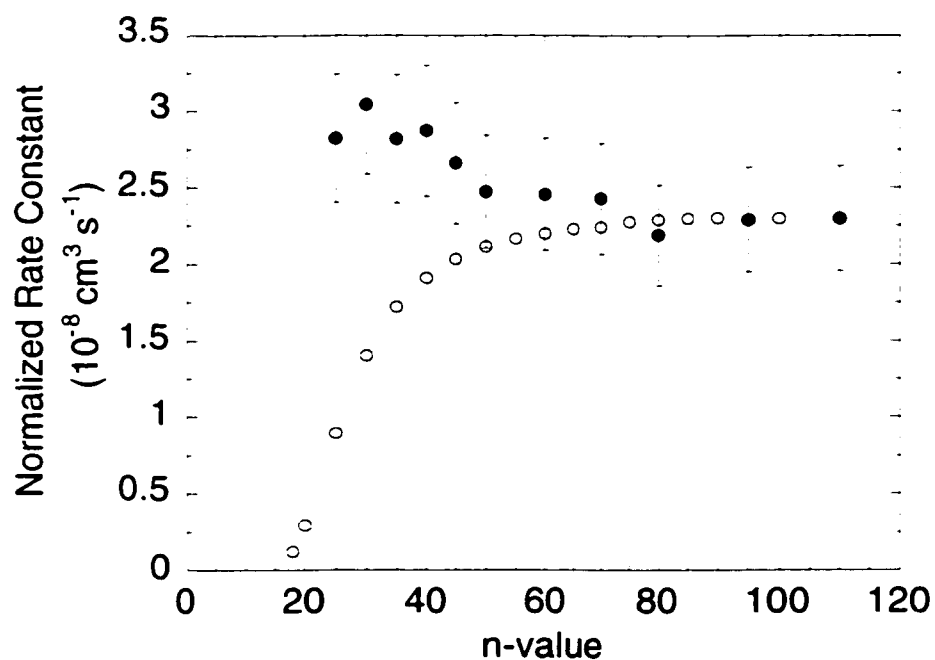
Figure 5.8   Rate constant for $C_7F_{14}^-$ production in $K(np)/C_7F_{14}$ collisions vs. principal quantum number. ● represents data from previous studies including statistical error bars; ○ represents model predictions. The model is normalized to the data at high n, where the escape probability is assumed to be 100%.

dominate. Because the electron and the Rydberg core are closer at lower n, the attachment occurs near enough for the internal energy transfer to take place.

The conclusion that electron attachment reactions involving C_7F_{14} produce two separate products: a free electron signal from a short-lived autodetachment process and a metastable $C_7F_{14}^-$ with a lifetime of at least 100 μs coincides with a simple model describing non-dissociative electron attachment mechanisms for large, polyatomic molecules.[32] The target molecule has numerous vibrational modes but only a few are strongly coupled to the electronic degrees of freedom in the scattering process. The number of active modes, those coupled to the captured electron, depends on the symmetry of the molecule; the selection rules limit the number of available modes for highly symmetric species. For large molecules, however, these few active modes are further coupled to many other vibrational modes, which cannot interact directly with the captured electron and are, therefore, termed inactive modes. This active to inactive mode coupling results in a process called intramolecular vibrational energy redistribution (IVR). IVR occurs when the vibrational energy originally concentrated in the active modes is redistributed among the inactive modes, where it is unavailable for the autodetachment of the electron. IVR, therefore, provides a mechanism to stabilize the intermediate ion for long periods of time. Eventually the energy trapped in the inactive modes will be redistributed into the active modes and cause autodetachment of the electron, but the probability of such a process decreases dramatically as the ratio of active to inactive modes decreases. The current experiment seems to imply that IVR must occur within ~15 ps after attachment occurs since the free electron signal corresponds to an intermediate lifetime of just less than that.

One would expect to see autodetached free electrons up until the competing IVR process takes place.

5.4 C_6F_6 Experiment

Collisions of potassium Rydberg atoms with C_6F_6 molecules result in reactions of the form:

$$K(20p) + C_6F_6 \rightarrow K^+ + C_6F_6^{-*} \rightarrow K^+ + C_6F_6^-$$
$$\rightarrow K^+ + e^- + C_6F_6 \tag{5.25}$$
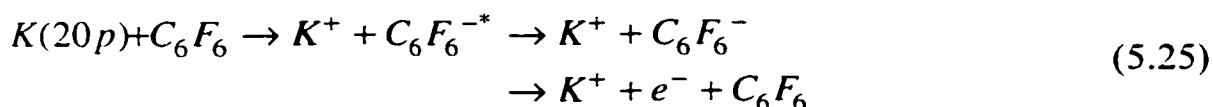
Many of the details described for the C_7F_{14} experiment also apply to the C_6F_6 experiment. Only the differences between the two procedures will be discussed here. The timing of the study differs in that the laser pulse is only 0.5 μs long, followed by a 0.5 μs delay prior to extraction, rather than the 1 μs laser pulse with no delay. As discussed previously, the reduced laser pulse better localizes the reaction volume and can be shorter for C_6F_6 since the rate constant for electron attachment is $\sim 1.2 \cdot 10^{-7}$ cm^3 s^{-1}.[27] The other major difference involves the actual method for recording the data. Unlike C_7F_{14}, this experiment does not record data in coincidence because the $C_6F_6^{-*}$ ion has a broad range of lifetimes. The metastable $C_6F_6^-$ falls apart on the way to the detector, thereby producing electron signals in a range of flight times. Thus, only the K^+ signal is recorded, assuming that all K^+ products result from either interaction with the C_6F_6 or with blackbody radiation. The ions resulting from blackbody photoionization, i.e. background ions, are accounted for by recording data without the presence of target gas. Similar to C_7F_{14}, the background counts are subtracted from the gas-in data, and the remaining distribution is used for analysis.

5.5 C_6F_6 Analysis

The preparation for analysis of the data follows the same methodology as that of C_7F_{14}. The center of the experimental distributions is found in relation to the center assumed by the model using the same two techniques. Figure 5.9 shows the K^+ distribution for blackbody interactions versus position along the K-beam (5.9a) and position along the laser beam (5.9b) used for the C_6F_6 study. Gaussian fits to the data in figure 5.9 determine the center of the distribution, (85.2, 66.6). Following the first method described above for C_7F_{14} and including the error propagation described in equations 5.15 through 5.18, the resulting shift in the center from the assumed (64,64) for the C_6F_6 data is:

$$\text{data points} = (x + 8.9, y - 2.6) \tag{5.26}$$

where (x,y) are the original data points. The C_6F_6 equivalent values to those given in equation 5.18 are given below in conjunction with the final error in the center shift.

$$
\begin{aligned}
c &= 85.2 \pm 0.1 \text{ ch} \\
v &= 350. \pm 45 \text{ m/s} \\
t &= 26.9 \pm 2.7 \ \mu s
\end{aligned}
\tag{5.27}
$$

giving $\delta D = 4.9$ ch and $\Delta x = 8.9 \pm 4.9$ ch. As with C_7F_{14}, the second method agrees within error with the first so the data are corrected to the model calculations. Figure 5.10 shows the experimental K^+ signal, produced in $K(20p)/C_6F_6$ collisions, versus arrival position and also includes several model calculations. The inset shows the corresponding arrival position distribution for visual clarity. The model calculations again assume an
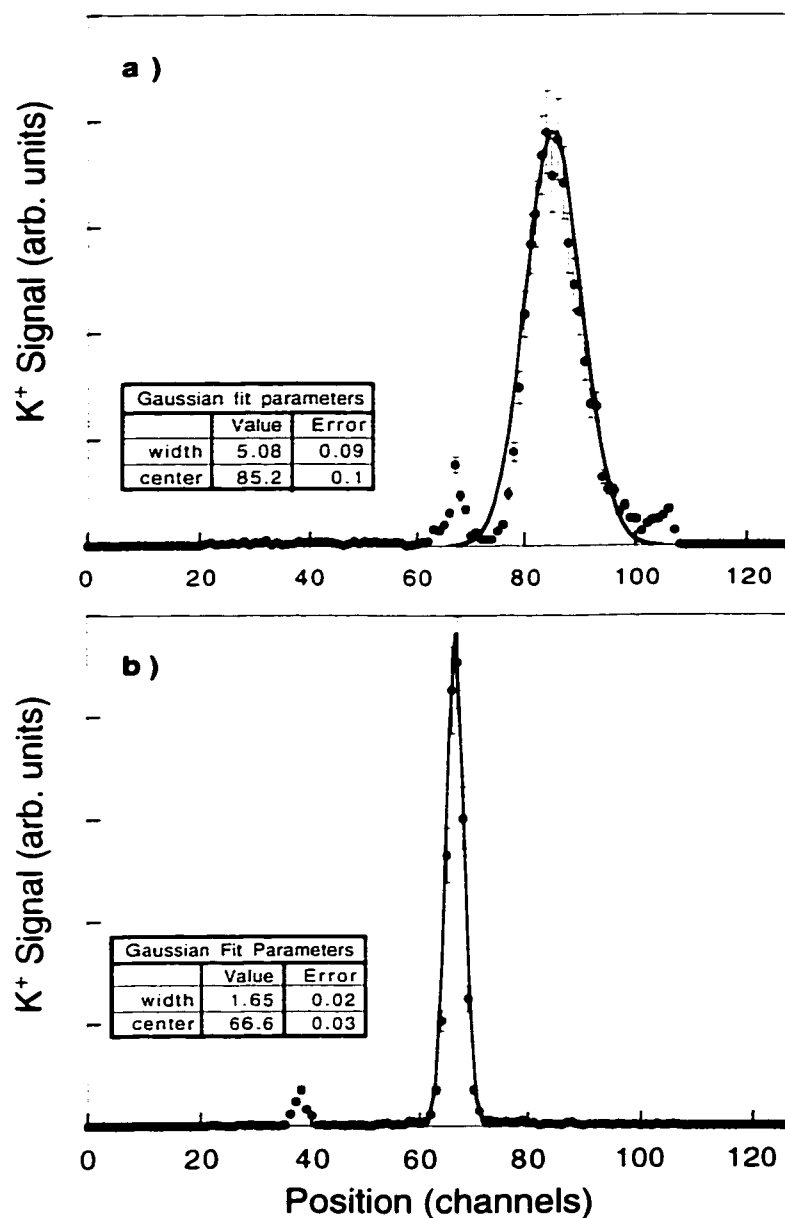
Figure 5.9 K^+ signal vs. position – a) along K-beam, b) along laser beam – for K^+ ions produced via blackbody photoionization in gas-out measurements during C_6F_6 experiment. • represents data with statistical error bars; solid line is a Gaussian fit to the data with the parameters shown.

Figure 5.10 K^+ signal produced in $K(20p)/C_6F_6$ collisions vs. arrival position. • represents data including statistical error bars; lines represent model calculations assuming an exponential translational energy release distribution centered on $\bar{\varepsilon} = 30$ meV and with τ shown. Inset shows corresponding arrival position distribution.

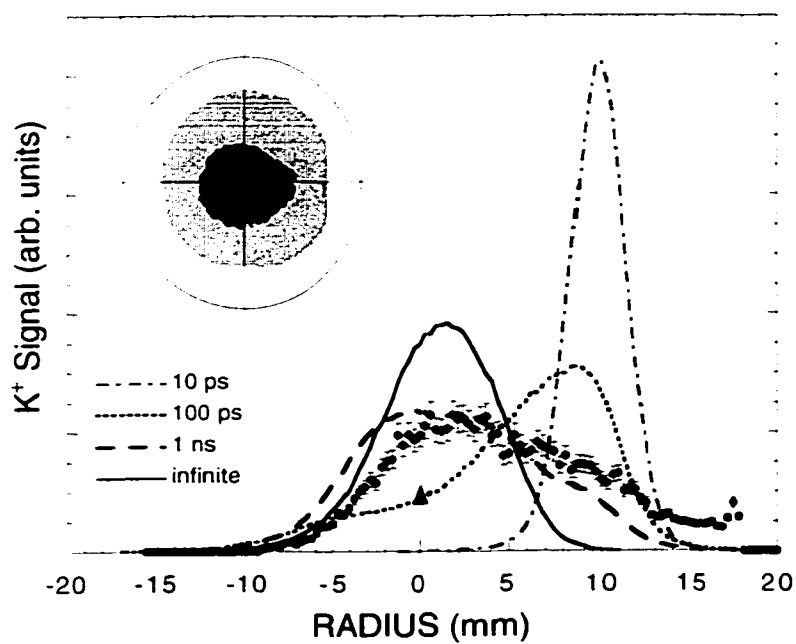exponential energy distribution for the detached electrons with a mean energy of $\bar{\varepsilon} = 30$ meV.

Examination of the data shows some peaking in the forward direction which implies that some fraction of the collisions result in formation of short-lived, $\tau \lesssim 1$ ns, intermediate $C_6F_6^{-*}$ ions. However, many of the K^+ ions appear scattered through large angles indicating the existence of long-lived $C_6F_6^-$ ions. Further examination of the long-lived species was undertaken by measuring $C_6F_6^{-*}$ signal strength versus flight time through the TOFMS, and the results are included in figure 5.7. Over the range of flight times observed, a significant decay of ion signal is apparent. A single exponential, however, does not fit the decay, which implies a distribution of lifetimes extending to values > 50 μs. In other words, $K(20p)/ C_6F_6$ collisions lead to intermediate $C_6F_6^{-*}$ ions with a range of lifetimes against autodetachment. Some internal-to-translational energy transfer may be occurring in bound $K^+/ C_6F_6^{-*}$ pairs and contributing to the production of the long-lived intermediates. However, most of the $C_6F_6^{-*}$ ions decay within a few microseconds of formation, so such a process would be inefficient at best. Further, since the separate K^+ product distributions associated with the free electrons and the $C_6F_6^{-*}$ ions could not be recorded, detailed analysis of the data is not possible.

The C_6F_6 results can again be explained as a competition between autodetachment and intramolecular vibrational relaxation (IVR). For C_6F_6, the total number of available modes is less than for C_7F_{14}, and the higher molecular symmetry of C_6F_6 suggests that fewer active modes will be directly coupled to the electron due to symmetry rules. This implies that IVR may be much less efficient at earlier times, thereby allowing autodetachment to dominate. However, in situations where IVR does occur the scarcity of

inactive modes suggests a high probability for reconcentration of energy back into the active modes, which accounts for the autodetachment observed at the later times.

Chapter 6
Future Work

6.1 Introduction

The current apparatus is limited to performing experiments with flight times $\lesssim 30$ μs for most ions. For slow, heavy ions slightly longer flight times are possible but usually result in significant losses off the edges of the detectors. The physical length of the TOFMS is the limiting factor and cannot be adjusted without completely redesigning the apparatus. Many electron attachment reactions involve processes that occur on a time scale much longer than 30 μs. For example, the metastable ions formed in the non-dissociative electron attachment reactions described previously are only stable for the time scale observable with the current apparatus. Evidence suggests that the ions studied will eventually decay but after a much longer lifetime ($\gtrsim 100$ μs). Another well-known example is SF_6, which readily attaches free electrons forming an ion with a lifetime of several ms.

Studying these and many other "long" processes requires the ability to have ion flight times adjustable over a much broader range. Many different designs were considered to adapt the apparatus for these studies. Initial designs considered extending the TOFMs to the greatest possible length in the available space. These designs retained the same limitation as the current apparatus: though longer, a maximum flight time still existed. A superior approach is to trap the ions as they travel toward the detector and to release them after a predetermined delay. In this way, the flight time equals the time spent in the trap.

Trapping charged particles can be accomplished in several different ways: Paul traps, Penning traps, and Electron beam ion traps, to name a few.

A Penning trap was determined to be the best option, considering the space limitations within the apparatus, the necessary vacuum compatibility, and ease of installation, removal, and operation of the trap. Details of the design and operation of a Penning trap and its important components will be discussed in this section. In addition, a series of possible experiments and the steps already taken toward accomplishing these will be presented.

6.2. Penning Trap

Since the first use of a Penning trap in 1936 [33] to increase the time electrons spent in a discharge many refinements have been made and several different applications have been devised. The motion of particles in a Penning trap can be quite complex and has been studied in detail both experimentally [34] and theoretically [35, 36, 37] including the effects of external influences. The system of a charged particle in a Penning trap has been called a "geonium atom" [35] since the particle is bound to an apparatus residing on the Earth. A single trapped particle is analogous to a one electron hydrogen atom, and the simplicity of this system allows extremely precise measurements of the bound particle's properties. Penning traps have been used to measure the magnetic moment (g-factor) of an electron to a precision unsurpassed using other methods.

A Penning trap uses combined magnetic and electric fields to confine charged particles. Figure 6.1 shows a cross-sectional diagram of an ideal Penning trap. The trap consists of three hyperbolic electrodes: two endcaps separated by a distance of $2z_0$ surrounding a ring of radius r_0. Ideally,
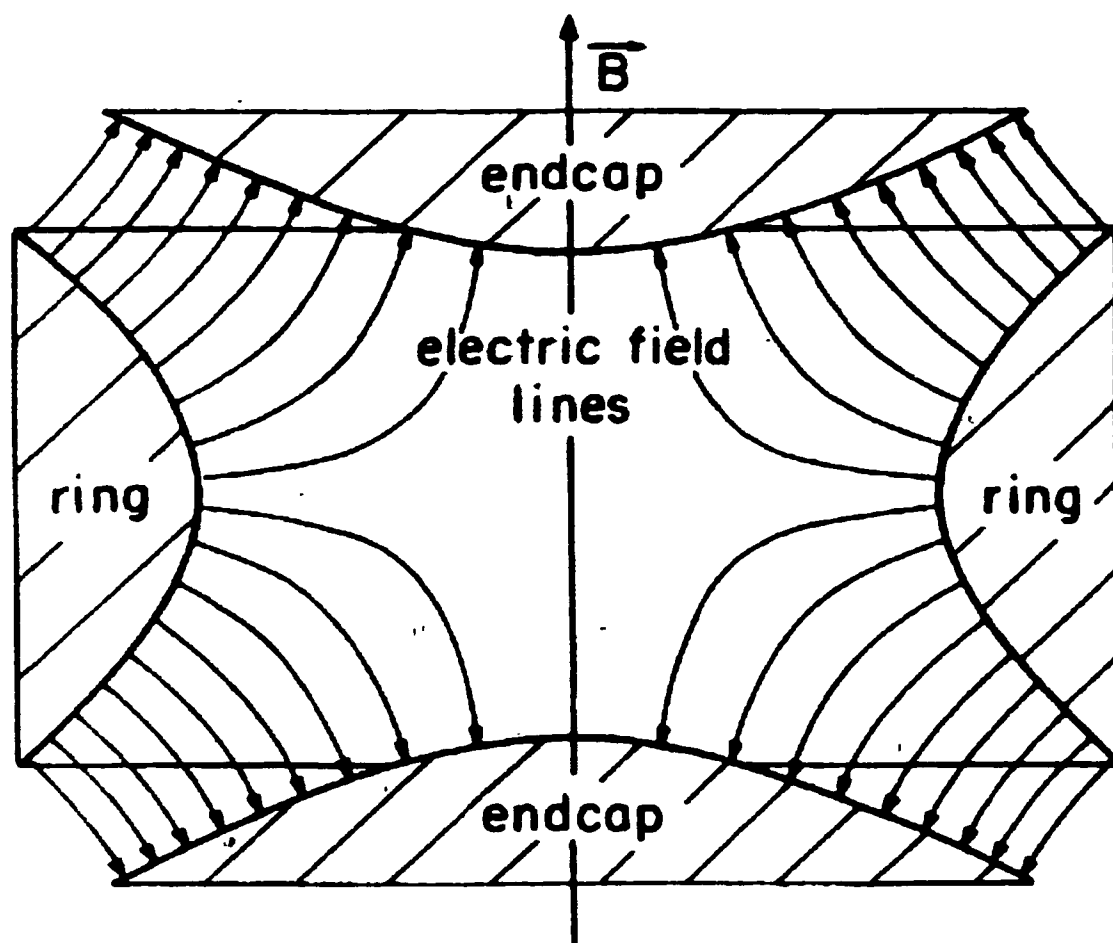
Figure 6.1 Electric and magnetic field configurations of an ideal Penning trap.

$r_0 = \sqrt{2} \cdot z_0$. To trap negative (positive) ions the endcaps are biased negative (positive) with respect to the ring, thereby creating a quadrupole electric field as shown in figure 6.1. Superimposed on the quadrupole electric field is a time-independent, strong, homogeneous magnetic field along the z-axis of the trap, the axis through the center of the endcaps. The resulting fields will confine the ion within the center of the trap for an almost indefinite period of time.

The motion induced by the electric and magnetic fields consists of three independent oscillations, two of which are stable and one that is an unstable equilibrium with a lifetime of years. [38] The electric field repels the ion toward the trap center from either endcap causing the ion to harmonically oscillate among the z-axis parallel to the magnetic field. Moving in only an electric field, an ion travels preferentially along the field lines, which in the case of a quadrupole field are not perfectly parallel to the z-axis. Thus, the ion in the trap tends to move toward the center and continue along the field lines radially outward to the ring electrode. A component of its motion is then perpendicular to the applied magnetic field, which forces the ion into a circular motion. This fast cyclotron motion prevents the ion from striking the ring electrode. The axial oscillations and the fast cyclotron motion provide a stable equilibrium environment for the trapped particle. A third motion, the magnetron motion, results from the interaction of the E × B fields and appears as a slow circular precession on the x-y plane. Figure 6.2 shows a projection of a trapped ion's motion onto the x-y plane. Clearly there is a small orbit cyclotron motion superimposed on a large orbit magnetron motion.

The equations of motion for a trapped particle are obtained by using an appropriate potential, setting up a Lagrangian equation, and using the
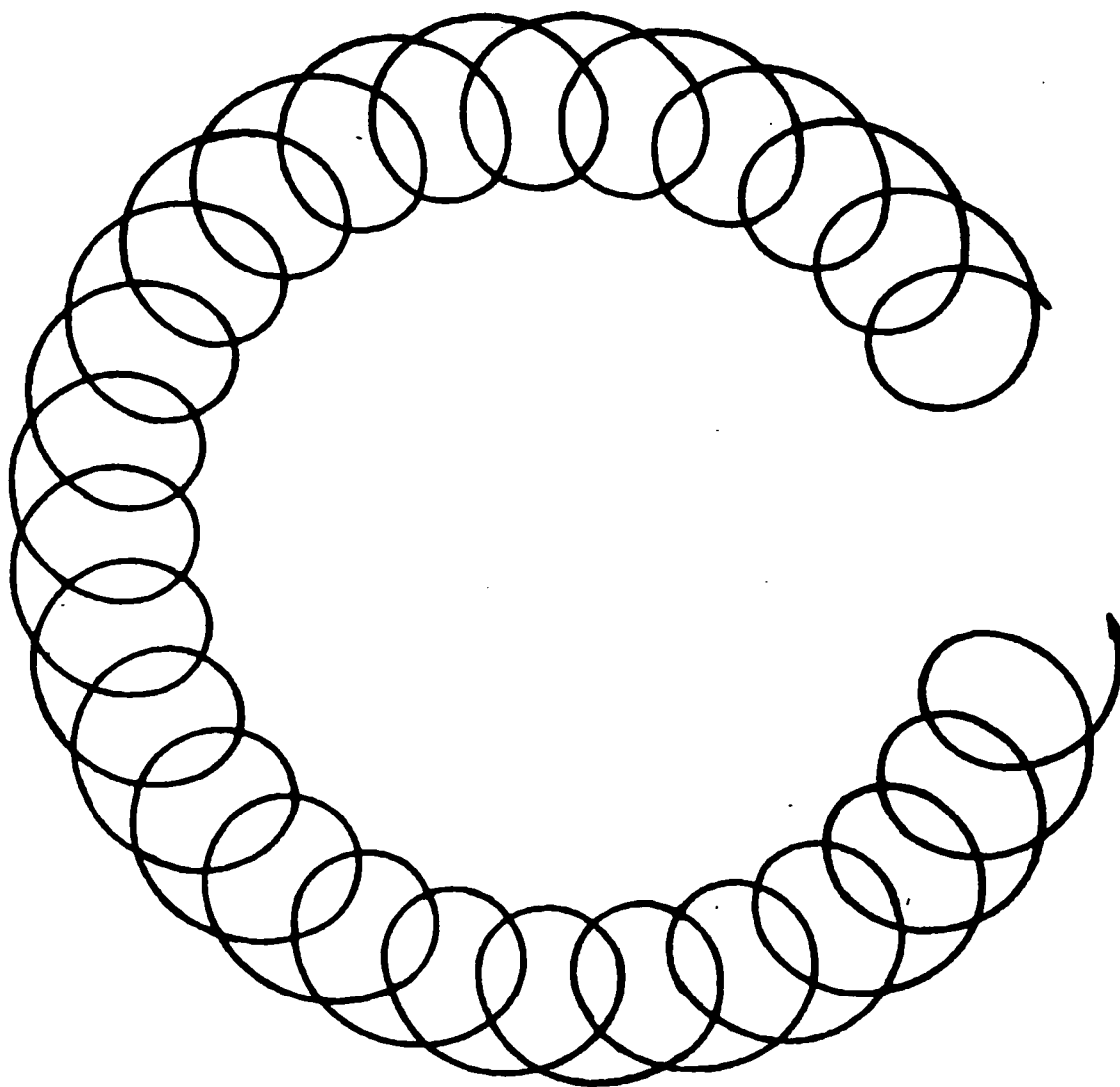
Figure 6.2 Projection of trapped ion motion onto the x-y plane.

Euler-Lagrange equation to solve for the equations of motion. For an electrostatic field the vector potential, $\vec{A}$, and the scalar potential, ϕ, are given by:

$$\vec{A} = 0$$
$$\phi = \phi$$

<div align="right">(6.1)</div>

and for a constant magnetic field

$$\vec{A} = \tfrac{1}{2}\vec{B} \times \vec{r}$$
$$\phi = 0$$

<div align="right">(6.2)</div>

where $\vec{B}$ is the magnetic flux density and $\vec{r}$ is the radial vector of the particle moving in the $\vec{B}$ field. Equations 6.1 and 6.2 yield a potential for the Penning trap of

$$\left(\phi, \tfrac{1}{2}\vec{B} \times \vec{r}\right)$$

<div align="right">(6.3)</div>

The Lagrangian is, therefore, given approximately by:

$$L \approx \tfrac{1}{2}m\dot{\vec{r}}^2 + \tfrac{e}{2c}\left[\vec{r}, \dot{\vec{r}}, \vec{B}\right] - e\phi$$
$$\approx \tfrac{1}{2}m\left(\dot{x}^2 + \dot{y}^2 + \dot{z}^2\right) + \tfrac{e}{2c}\left(x\dot{y} - y\dot{x}\right) - e\phi$$

<div align="right">(6.4)</div>

neglecting the field-free Lagrangian, where m is the mass of the particle and ϕ is given by:

$$\phi = \frac{U}{2z_0^2 + r_0^2}\left(2z^2 - x^2 - y^2\right)$$

<div align="right">(6.5)</div>

with U being the potential applied to the endcap electrodes with respect to the ring electrode. The resulting equations of motion are:

$$\ddot{x} = \omega_c \dot{y} + \tfrac{1}{2}\omega_{0z}^{\,2} x$$
$$\ddot{y} = -\omega_c \dot{x} + \tfrac{1}{2}\omega_{0z}^{\,2} y \qquad\qquad (6.6)$$
$$\ddot{z} = -\omega_{0z}^{\,2} z$$

where ω_{0z} is the axial frequency and ω_c is the cyclotron frequency:

$$\omega_{0z} = \sqrt{\frac{4qU}{m\left(2z_0^{\,2}+r_0^{\,2}\right)}}$$
$$\omega_c = \frac{qB}{mc} \qquad\qquad (6.7)$$

q is the charge on the trapped particle, m its mass, and the other variables are defined previously. Further mathematics, beyond the scope of this work, provide an equation for the radial motion. [39] For a particle to remain trapped the motion must be bound in the radial direction so solutions to the radial equation provide additional frequency restrictions. Defining a frequency:

$$\omega_{01} = \sqrt{\omega_c^{\,2} - 2\omega_{0z}^{\,2}} \qquad\qquad (6.8)$$

the condition $\omega_c^{\,2} - 2\omega_{0z}^{\,2} > 0$ must be satisfied and the solutions to the radial equation can be written:

$$\omega_{0\pm} = \tfrac{1}{2}\left(\omega_c \pm \omega_{01}\right) \qquad\qquad (6.9)$$

The root associated with the positive sign is a modified cyclotron frequency with modifications due to the electrostatic potential. The root frequency associated with the negative sign is the magnetron frequency.

The trapped particle in an ideal Penning trap can be considered a multiperiodic system with three degrees of freedom. The three motions (axial, modified cyclotron, magnetron) are completely independent and uncoupled. However, under usual operating conditions the following relationship must exist for stable confinement:

$$\omega_{0+} \approx \omega_c >> \omega_{0z} >> \omega_{0-} \qquad (6.10)$$

The energy in the cyclotron motion is mainly kinetic, and the axial oscillations alternate between kinetic and potential energy. Thus, reducing the energy in either motion simply reduces its amplitude implying a stable orbit. The magnetron motion is essentially potential energy, however, and is unbound. Dissipative forces reducing energy in the magnetron motion cause the radius to increase until the ion strikes the ring electrode. This damping process is fortunately very slow, typically on the order of years. [35] The ion motion in the trap, therefore, remains adequately stable.

The motion of a trapped particle can also be described quantum mechanically by treating the system as three separate harmonic oscillators. However, for the applications of the trap described herein a classical description will suffice. [39]

A real Penning trap differs from the ideal model, just described, in many ways. The real Penning trap has a finite size; its geometry may differ from ideal; the electrodes or the magnetic field may be misaligned; and other perturbations may exist, like the presence of a buffer gas. Applying perturbation theory to the Lagrangian equation (equation 6.4) the modified frequencies of motion of the trapped particle can be determined in relation to the ideal frequencies, derived above. [35, 39] The change in the frequencies is

very important for precision measurements but should have little effect on the studies proposed here.

The two important components of the Penning trap designed for the current apparatus are the electronics, which control the quadrupole field, and the structure providing the magnetic field. Each of these components is discussed in detail in the following sections.

6.3 Trap Electronics

The simplest design for a Penning trap uses orthogonalized cylindrical symmetry. Flat discs replace the hyperbolic endcaps, and the ring electrode becomes a basic tube. The geometric distortions from ideal change the shape of the electric field lines and, thus, impose some modifications on the trapped particle's motion. The distortions, however, are insufficient to prevent particle confinement. Experiments done using orthogonalized cylindrical Penning traps [40] have taken advantage of the shape of the trap, which approximates a cylindrical microwave cavity, and have studied the interaction between the trapped particle and radiation present in the trap. These studies produced remarkable results considering the drastic simplifications of the trap geometry. Figure 6.3 shows a cross-sectional view of the electrodes designed for the current apparatus. The electrodes are made from oxygen-free-high-conductivity (OFHC) Copper, and the two end discs consist of Cu plates supporting 70 lpi (lines per inch) fine mesh Cu grid material. The ring electrode is a Cu tube with a ~4.2 cm inner radius and a length of ~7.2 cm. The electrodes can be individually biased. Specially designed Teflon spacers electrically isolate the tube from the plates. Four ~4 mm holes 90° apart perforate the Cu tube mid-way down its length. The
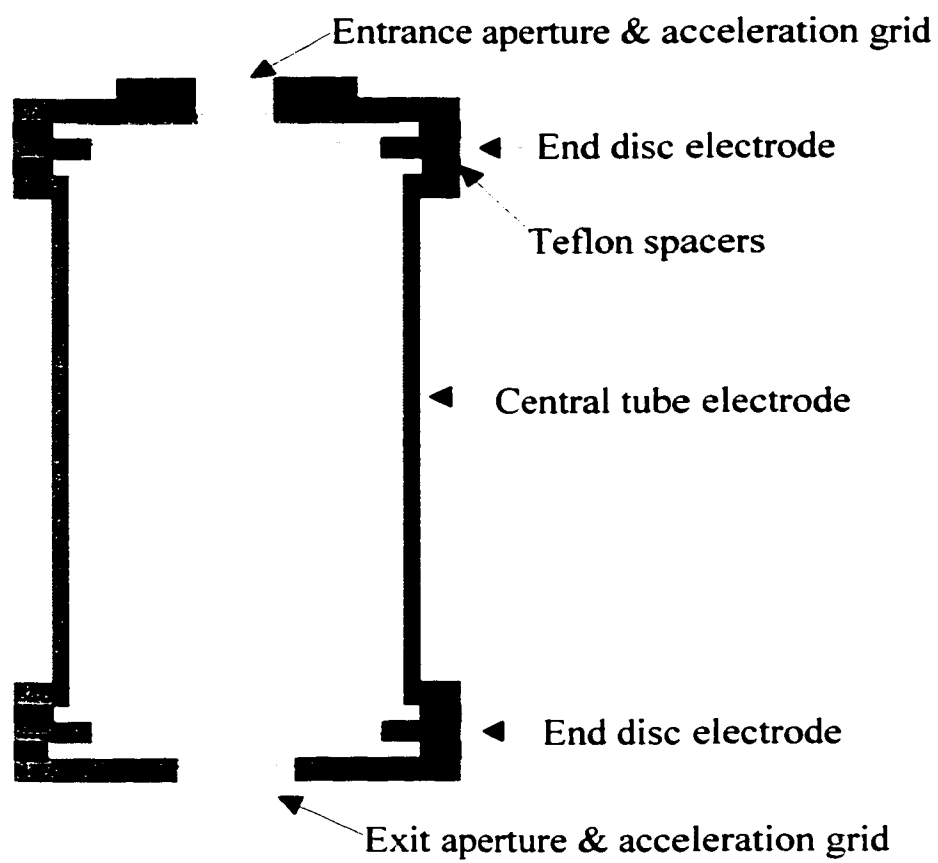
Entrance aperture & acceleration grid

End disc electrode

Teflon spacers

Central tube electrode

End disc electrode

Exit aperture & acceleration grid

Figure 6.3 Cross section of Penning trap electrodes.

holes add flexibility to the system by providing access ports to the center of the trap. Such apertures can be used to admit the potassium and laser beams for studies of Rydberg excitation/negative ion formation at the trap's center.

For studies in which Rydberg excitation/ion formation does not occur at the center of the trap, an electronics module has been designed and built to allow the injection of ions formed in the interaction region into the trap during flight through the TOFMS. The end grids can be used as gates, which are opened or closed via a fast voltage switch from an attractive potential to a repulsive potential with respect to the ion in flight. Assuming a negative ion, a positive potential on the first grid admits the ion into the trap. A negative potential on the second grid prevents its escape through the bottom. Meanwhile, the potential on the first grid is switched to negative, thereby enclosing the ion within the trap. The ion can be released by simply switching the bottom electrode to positive and accelerating the ions from the trap. A diagram of the electronics circuit needed to accomplish this task is shown in figure 6.4.

The circuit operates off a ± 24 V power supply, which is regulated by two 3-terminal adjustable regulators, one for the positive and one for the negative. The regulated voltages are used to power the two ADG436 Analog switch chips. The switch chips accept two input voltages and a trigger, which causes the output of the chip to switch from one input voltage to the other with a turn on time of ≤ 200 ns. The output voltage of each switch chip is sent directly to the end plates of the trap, one switch for each end. The circuit shown in figure 6.4 has three input reference voltages — one for injection, one for trapping, one for ejection — and two triggers. The external triggers can be provided by a computer controlled pulser to allow precise timing. The entire cycle of trapping ions formed external to the trap and then
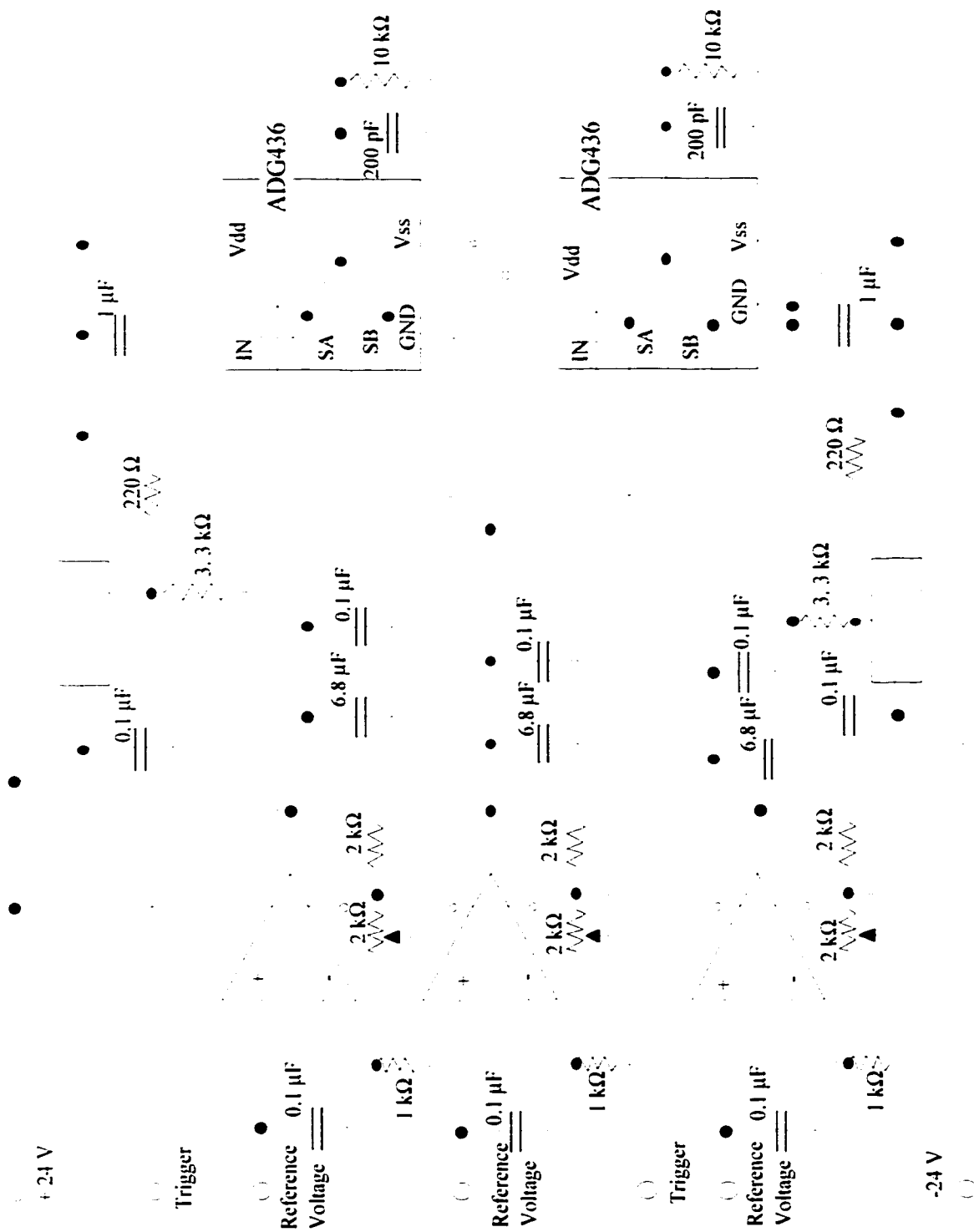
Figure 6.4 Electronic circuit diagram for Penning trap switching circuit.

releasing them works as follows. The switch for the entrance plate is set to the injection reference voltage, and the switch for the exit plate is set to the trapping reference voltage. After a time sufficient to allow the ions to enter the trap, the entrance plate switch is triggered to output the trapping reference voltage. With both the exit and entrance plates at the same voltage, the ion is trapped. To release the ion, the exit plate switch is triggered to output the ejection voltage.

The voltages applied to the end plate electrodes must be carefully monitored and controlled. A critical voltage does exist at which the electric field provided by the applied potential overcomes the confining force of the magnetic field ($q\bar{v} \times \bar{B}$). This critical voltage for singly ionized atoms (or electrons) is given by:

$$V_c \cong \frac{1200B^2\left(r_0^2 + 2z_0^2\right)}{M} \tag{6.11}$$

where V_c is in volts, B in Tesla, M is the particle mass in AMU, and the dimensions of the trap are in cm. Similarly, space charge limits the achievable densities in a Penning trap. [38] Table 6.1 gives the values and dimensions appropriate for the current trap, assuming a trapped SF_6 particle, an applied voltage of 10 V, and two different magnetic fields, 0.15 T and 0.25 T. (The magnetic field of the current trap has been predicted to be 0.25 T using PC-Opera, a finite element analysis program distributed by Vector Fields Corporation. Considering possible discrepancies between the calculation and the actual field, the minimum field likely within the trap is 0.15 T.)

Table 6.1

Property	Value	
z_0	0.072 m	
r_0	0.042 m	
q	1.602e-19 C	
m	146 AMU	
U	10 V	
V_c	22 V	
B	0.15 T	0.25 T
ω_c	$9.9 \cdot 10^4$ rad s^{-1}	$1.6 \cdot 10^5$ rad s^{-1}
ω_{0z}	$4.7 \cdot 10^4$ rad s^{-1}	$4.7 \cdot 10^4$ rad s^{-1}
ω_{0-}	$1.3 \cdot 10^4$ rad s^{-1}	$6.9 \cdot 10^3$ rad s^{-1}

The magnetic field strength required to trap ions with a wide range of masses is quite large. Further, the field must be time-independent and spatially homogeneous. Such a magnetic field is typically produced using an electromagnet, but for the current apparatus an electromagnet introduces a number of complications. An electromagnet requires significant currents, which generate heat. The PSDs cannot operate at high temperatures, and thus a cooling system would be necessary. In addition, physical space constraints prevented the use of a bulky electromagnet system. Fortunately, recent advances allow generation of high fields using permanent magnet materials.

6.4 Permanent Magnets

The advent of a new generation of permanent magnet materials has completely redefined the possible structures and applications of permanent magnets. The properties of rare earth permanent magnets (REPM) allow production of magnetic field geometries that were previously unattainable. The remarkable characteristics of REPMs originate from two fundamental attributes: 1) large intrinsic magnetic moments per unit volume; 2) extremely high resistance to demagnetization by external or internal fields. Consequently, REPMs can be formed into shapes that would easily cause demagnetization in a different material.

Permanent magnets have generally been used in applications which convert electrical energy to mechanical energy or vice versa; for example, motors, audio speakers, generators, computer disc drives, etc. Those types of applications undoubtedly will remain the dominant uses for permanent magnets. Certain applications, requiring complicated or very specific magnetic fields, are usually achieved using electromagnets, which are effective at producing high fields. However, they can be somewhat unwieldy to use due to their large size, high currents, and the cooling system often needed to dissipate the heat produced by such high currents. The ability to produce a permanent magnet structure that provides a constant field at room temperature within a small volume may revolutionize and simplify many types of experiments. REPMs may prove to be the necessary ingredient for such an achievement.

After a brief review of magnetism, Maxwell's equations, and the important magnetic properties considered when designing a structure, the ceramic magnets of the past will be compared with REPMs. Thereafter, a discussion of the four approaches to magnetic design will lead to a

presentation of more applications of permanent magnets, including those structures relative to this work.

6.5 Review of Magnetism, Maxwell's Equations, etc.

"The magnetization of a piece of ferromagnetic material has its origin in the spin and orbital magnetic moments of the atomic electrons, . . . but if the ferromagnetic sample can be prepared in a metastable state where it retains some net magnetization more or less independently of external magnetic fields, it is then known as a permanent magnet." [41] The fundamental, microscopic alignment of the magnetic moments produces several macroscopic, measurable traits, which comprise the basis of Maxwell's magnetic equations. These macroscopic qualities include: the flux density of the magnet, $\bar{B}$; the magnetic field strength, $\bar{H}$; and the magnetization of the material, $\bar{M}$, which is directly proportional to the polarization, $\bar{J}$. The relationship among these quantities differs depending on location (inside or outside the magnet) and on the presence of external fields, conduction currents, etc. In free space, outside the magnet, $\bar{B}$ is parallel to $\bar{H}$ and they are related by:

$$\bar{B} = \mu_0 \bar{H} \qquad (6.12)$$

where μ_0 is the permitivity of free space and has a value of $4\pi \cdot 10^{-7}$ Tm/A. Inside the magnet the two quantities need not be parallel. The alignment of the magnetic moments within the magnet determines the magnetization of the material, which affects the orientations and magnitudes of $\bar{B}$ and $\bar{H}$.

$$\bar{B} = \mu_0 (\bar{H} + \bar{M}) \qquad (6.13a)$$

or

$$\vec{B} = \mu_0\vec{H} + \vec{J} \qquad (6.13b)$$

since $\vec{J} = \mu_0\vec{M}$. The relationship between $\vec{B}$ and $\vec{H}$ within a magnet is more complicated; but a simple use of Maxwell's equations shows that in an isolated magnet, in the absence of any external fields, $\vec{B}$ and $\vec{H}$ tend to be antiparallel.

To compare the direction of $\vec{B}$ and $\vec{H}$, the projection of $\vec{B}$ onto $\vec{H}$ is used (i.e. $\vec{B}\cdot\vec{H}$). Integrating over the relevant volume gives the resultant angle between the vectors. We already know the relationship between the flux density and the field strength outside the magnet and are interested in the relationship inside the magnet. Therefore, break the integral over all space into two parts:

$$\underset{\text{all space}}{\int\vec{B}\cdot\vec{H}d\tau} = \underset{\text{empty space}}{\int\vec{B}\cdot\vec{H}d\tau} + \underset{\text{magnet}}{\int\vec{B}\cdot\vec{H}d\tau} \qquad (6.14)$$

Assuming no external fields or conduction currents, Maxwell's equations give:

$$\nabla\cdot\vec{B} = 0 \qquad (6.15a)$$

$$\nabla\times\vec{H} = 0 \qquad (6.15b)$$

And $\vec{B}$ can be written as $\nabla\times\vec{A}$, where $\vec{A}$ is the vector potential and satisfies $\nabla\cdot\vec{A} = 0$. Thus:

$$\underset{\text{all space}}{\int\vec{B}\cdot\vec{H}d\tau} = \underset{\text{all space}}{\int(\nabla\times\vec{A})\cdot\vec{H}d\tau} \qquad (6.16)$$

using the vector identity:

$$(\nabla \times \bar{A}) \bullet \bar{H} = \nabla \bullet (\bar{A} \times \bar{H}) + \bar{A} \bullet (\nabla \times \bar{H}) \tag{6.17}$$

equation 6.16 becomes:

$$\int (\nabla \times \bar{A}) \bullet \bar{H} d\tau = \int \left\{ \nabla \bullet (\bar{A} \times \bar{H}) + \bar{A} \bullet (\nabla \times \bar{H}) \right\} d\tau \tag{6.18}$$

From equation 6.15b the second part of the integral on the right hand side equals 0. Using the divergence theorem, the first part of the integral on the right hand side of equation 6.18 can be rewritten as:

$$\int_{\text{all space}} \nabla \bullet (\bar{A} \times \bar{H}) d\tau = \int_{\text{closed surface}} (\bar{A} \times \bar{H}) dS \tag{6.19}$$

Assuming the closed surface is a very large sphere, $S \propto r^2$, $\bar{H} \propto \frac{1}{r^3}$, $\bar{A} \propto \frac{1}{r^2}$. For a point far away from the magnet the field can be considered that of a dipole, which implies $\bar{H} \propto \bar{B} \propto \frac{1}{r^3}$ and, therefore, $\bar{A} \propto \frac{1}{r^2}$. Combining these proportions shows that this integral also goes to zero. Therefore, equation 6.16 becomes:

$$\int_{\text{all space}} \bar{B} \bullet \bar{H} d\tau = 0 \tag{6.20}$$

from which automatically follows

$$\int_{\text{empty space}} \bar{B} \bullet \bar{H} d\tau + \int_{\text{magnet}} \bar{B} \bullet \bar{H} d\tau = 0 \tag{6.21}$$

giving

$$\int_{\text{empty space}} \bar{\mathbf{B}} \bullet \bar{\mathbf{H}} d\tau = - \int_{\text{magnet}} \bar{\mathbf{B}} \bullet \bar{\mathbf{H}} d\tau \qquad (6.22)$$

From equation 6.12

$$\mu_0 \int H^2 d\tau = - \int_{\text{magnet}} \bar{\mathbf{B}} \bullet \bar{\mathbf{H}} d\tau \qquad (6.23)$$

This suggests that the right hand side must be positive which implies that within the magnet $\bar{\mathbf{B}}$ and $\bar{\mathbf{H}}$ tend to be antiparallel. [41, 42]

6.6 Comparison of Magnet Materials

The preceding review of magnetism presents the fundamental quantitative values associated with permanent magnets in the absence of external fields, but comparing various classes of magnet materials requires inclusion of external fields and a few other associated quantities. By definition, a permanent magnet must maintain an oriented field even in the presence of an external demagnetizing field of some strength. The net magnetization depends on the relationship between $\bar{\mathbf{M}}$, the intrinsic polarization a material retains versus the demagnetizing field strength, $\bar{\mathbf{H}}$. A graph of $\bar{\mathbf{M}}$ versus $\bar{\mathbf{H}}$ illustrates the relationship, and from the $\bar{\mathbf{M}}$ vs. $\bar{\mathbf{H}}$ graph the more common $\bar{\mathbf{B}}$ vs. $\bar{\mathbf{H}}$ graph is derived using equation 6.13a. Physicists interested in magnetism tend to measure $\bar{\mathbf{M}}:\bar{\mathbf{H}}$ loops, while $\bar{\mathbf{B}}:\bar{\mathbf{H}}$ loops apply more to engineering applications.

Figure 6.5 shows a typical example of an $\bar{\mathbf{M}}:\bar{\mathbf{H}}$ loop (6.5a) and a $\bar{\mathbf{B}}:\bar{\mathbf{H}}$ loop (6.5b) for a permanent magnet. The hysteresis loops shown describe the magnetization/ demagnetization cycle of a material. For a sufficiently large value of the external field, $\bar{\mathbf{H}}$, the polarization of the medium reaches saturation, as shown by the line from the origin to the maximum value of $\bar{\mathbf{H}}$.
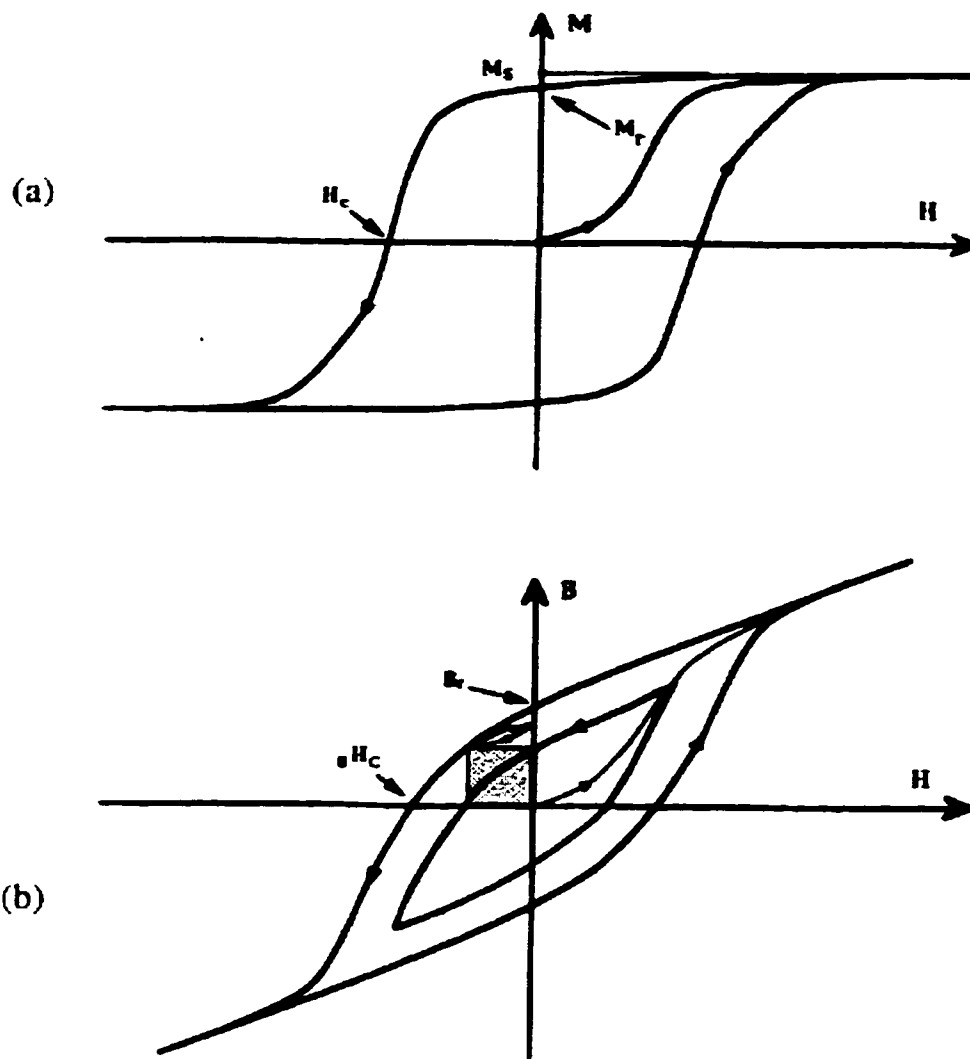
Figure 6.5 Magnetization/demagnetization loops for permanent magnet materials. (a) $\bar{M}:\bar{H}$ loop; (b) $\bar{B}:\bar{H}$ loop.

Then, as the external field is reduced to zero, the magnetization, $\bar{M}$, follows the upper path in quadrant I. The value of $\bar{M}$ remaining at $|\bar{H}| = 0$ represents the remenance of the magnet, M_r seen in figure 6.5a. The corresponding residual flux density, B_r, (figure 6.5b) is just $\mu_0 \bullet M_r$, again using equation 6.13a. This is the point where the magnetizing/demagnetizing field, $\bar{H}$, equals zero.

As the direction of the external field is reversed, $\bar{M}$ decreases following the curve in quadrant II. The abscissa of the point, H_c, where the curve crosses the H-axis (figure 6.5a) represents the value of the magnetic field intensity required to cancel the magnetic induction within a material. This is called the coercive force or the intrinsic coercivity. The word intrinsic is somewhat misleading, however, because H_c is not an intrinsic property of the ferromagnetic phase; H_c depends on a magnet's size, shape, crystalline structure, etc. The corresponding point in figure 6.5b, $_BH_c$ is often referred to as simply the coercivity. As shown by the graphs, the intrinsic coercivity is typically much higher than the coercivity. In other words, a much stronger reverse field is required to demagnetize the material than is necessary to cancel its flux density.

The remainder of the hysteresis loop describes the magnetization of the material in the direction opposite its original magnetization (quadrant III) followed by demagnetization in that direction (quadrant IV). Finally, the cycle is completed by remagnetization in the original direction (quadrant I). The $\bar{M}:\bar{H}$ and $\bar{B}:\bar{H}$ loops are reproducible provided the applied field is sufficient to achieve saturation within the material in each direction.

Another important material characteristic is the maximum energy product, BH_{max}. The $\bar{B}:\bar{H}$ loop represents the energy that can be delivered by a permanent magnet, and each point represents the potential energy $\bar{B} \bullet \bar{H}$.

The operating point at which this product is maximized provides the greatest potential energy from the magnet and, in terms of manufacture, means that the minimum volume of material is needed to supply a given energy. [43]

Typically, only the second quadrant of the $\bar{B}:\bar{H}$ loop is used for comparison of magnet materials. The demagnetization curve, as it is called, describes the field produced by a permanent magnet in the presence of an external field oriented in the opposite direction. This situation illustrates the properties of a permanent magnet under normal operating conditions. However, certain external influences like temperature, pressure, or applied field can change the magnetic characteristics of a material after manufacture and cause deviation from the B-H operating curve. Three types of deviations occur: permanent changes, which remain after the external condition is removed and cannot be corrected without completely retempering and remagnetizing the material; irreversible changes, which also persist after the removal of the external influence, but the original properties can be restored by total remagnetization alone; and reversible changes, which exist only in the presence of the external condition, returning to normal after its removal.

The net effect of external conditions depends highly on the composition of the magnet and, therefore, must be considered when comparing magnetic materials. Many properties define the limits of the external influence on magnets. For example, the Curie temperature is the temperature at which the elementary magnetic moments in a given magnet material are randomized, causing complete demagnetization and permanent changes. Though the Curie temperature establishes an upper limit, the maximum operating temperature is significantly lower for most magnets and depends on the magnet shape. Maximum operating temperature represents

the maximum practical operating temperature in air without irreversible changes occurring in the material. [44, 45]

Other practical issues also must be considered when determining the most appropriate magnetic material for an application. The cost of the materials varies widely as does the machinability. Thus, the volume and shape of the final magnet assembly influences the material choice as much as does the environment in which the assembly is to be operated.

Many references provide detailed descriptions of each of the four main magnetic materials: ceramic or ferrite, Alnico, SmCo, and NdFeB. Campbell [44] chapter 2 and McCaig [45] chapter 4 both describe the crystalline structures and explain why the four have such different properties. Further, the authors detail the manufacturing processes for each magnet type and note that the properties of each are influenced by the exact manufacturing procedure. This work is concerned more with how the characteristics differ among the materials and less with why they differ. Within each class of material, however, there is a wide range of properties, which is a direct result of both the crystalline structure and the manufacturing process. The range varies so much within a single class that taking an average is not a legitimate means of comparison.

Figure 6.6 illustrates the range covered by each material for several of the properties discussed previously. The bar graphs shown provide comparison among the four materials for each property. It is important, however, to remember that some of the values depend on the size and shape of the magnet. The values depicted by figure 6.6 are for comparable shapes and sizes of the materials. It cannot be assumed that a grade of material having the lowest value for one characteristic has the lowest value for all. Figure 6.6 indicates only basic trends among the four classes of materials.
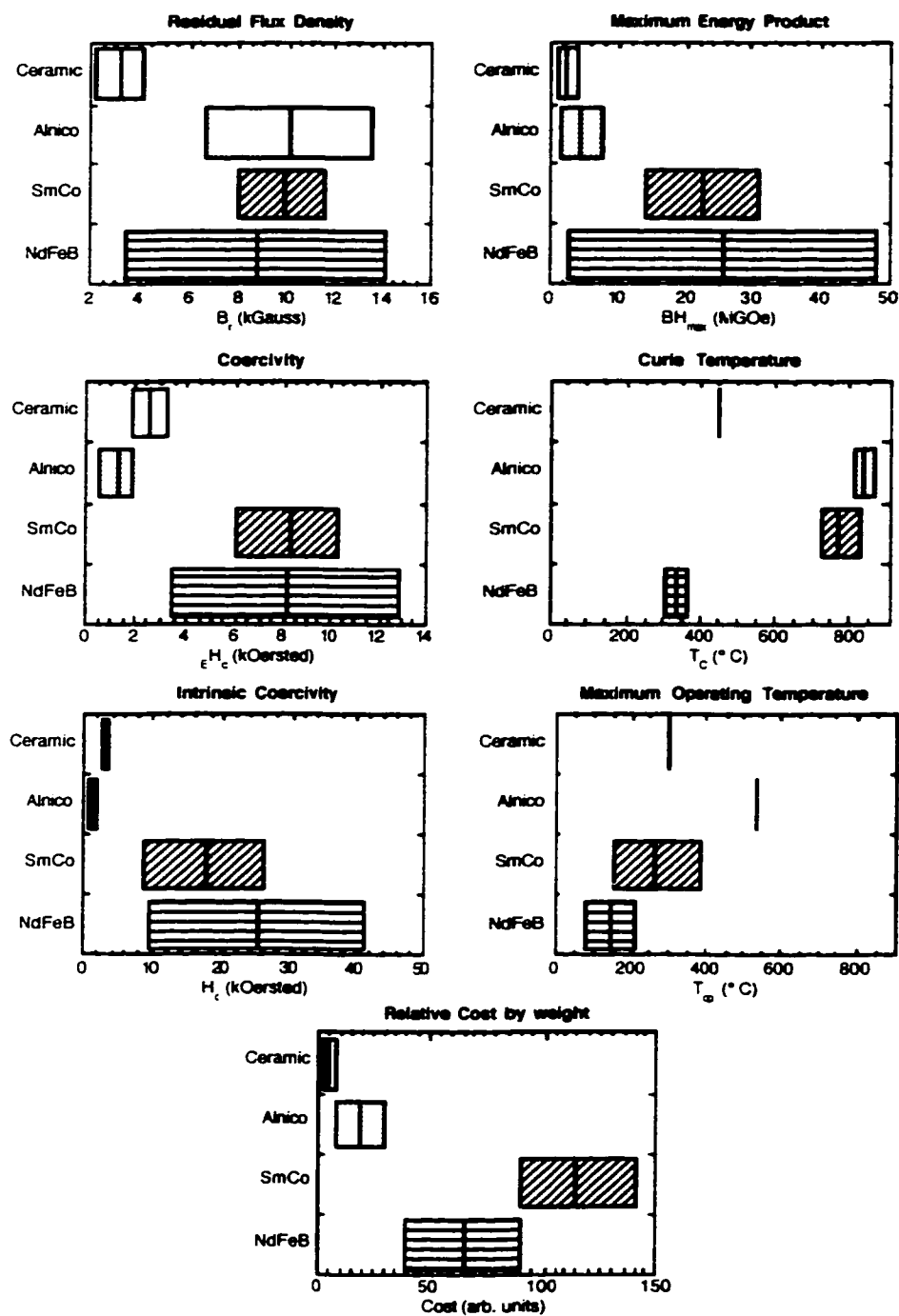
Figure 6.6 Comparison of various properties of permanent magnet materials.

Comparison of the demagnetizing curves of each material would be another way to visualize the similarities and differences among the four. The huge variance within each material, however, eliminates this as a useful exercise. It would be unfair to choose one grade of material over another to compare; and for the highest grades of each material, the demagnetizing curves all have a similar shape.

It is obvious from figure 6.6 that no single material dominates every characteristic. The REPMs, SmCo and NdFeB, surpass the older magnet types in most areas, except for the Curie and maximum operating temperatures. Alnico appears to be the best choice for operation at higher temperatures, but it has little energy storage capability and a low coercivity. Though REPMs are much more expensive, their high remanence and coercivity allow for much more complicated designs. The presence of a reverse field has little effect on REPMs and, thus, magnet assemblies can incorporate several magnets with fields oriented in many directions. Determining the exact magnet shape necessary to create the desired field is the next step after choosing the material.

6.7 Magnet Assembly Design

With older magnet materials, magnetic circuit design is essentially trial-and-error. The magnetization of ceramic and Alnico magnets depends strongly on the geometry of the field structure surrounding them. In addition, the flux densities of those materials are extremely low for all but the most ideal conditions. Exact analytical solutions are, therefore, very difficult if not impossible even for simple configurations. Design then relies on numerical approximations, physical models, or rules of thumb.

The properties of REPMs simplify the design process, and expand the range of traditional approaches to magnetic design. These approaches can be divided into four basic categories: 1) the analogy of magnetic configurations with electrical circuits; 2) analytical solutions using Maxwell's equations; 3) the reduction of permanent magnets to equivalent distributions of pole densities or current sheets, which can be used in Coulomb's law or the Biot-Savart law; 4) numerical solutions using finite element analysis. In this work, the first category is predominantly used in conjunction with the fourth to obtain the optimal configuration for our applications.

Magnetic configurations can be related to electrical circuits through a magnetic analog of Ohm's Law. The electric current I correlates with the magnetic flux Φ, the electromotive force V with the magnetomotive force F, the electric conductance G with the magnetic permeance P, and the resistance R with the reluctance R. The magnetic Ohm's law becomes:

$$\Phi = PF = \frac{F}{R} \tag{6.24}$$

Corresponding to

$$I = GV = \frac{V}{R} \tag{6.25}$$

Permanent magnets then equate to magnetic *batteries*. Materials like iron or permalloy, which have high permeability, can be considered near perfect *conductors* of magnetic flux, analogous to copper, a near perfect electrical conductor. In addition, air gaps or materials with low permeability become magnetic *resistors*.

Though the magnetic circuit analogy seems satisfyingly simple, two significant discrepancies limit its usefulness. First, while electric currents

follow the systematic, controllable paths provided by wires, magnetic fluxes have no limits and fill virtually all space. This issue is surmountable by breaking the space immediately surrounding permanent magnets into flux paths with planar, cylindrical, or spherical boundaries. Provided the surfaces are chosen wisely, standard formulas return amazingly accurate values of the flux densities emanating from the chosen surfaces. The second problem exists only for the older magnetic materials. Ceramic and Alnico magnets do not produce a constant magnetomotive force (mmf). Their mmfs change as a direct result of the circuit in which they are used. Conversely, REPMs emit the same mmf regardless of their surroundings, thereby simplifying the analysis of magnetic designs that use them. [46]

References Leupold [46] and Coey [41] both derive a much more detailed equation of the magnetic analog to Ohm's law beginning from Ampere's equation. They also describe in detail an example of a magnetic gap field calculation using the electric circuit analogy. These in depth calculations are beyond the scope of this work but may be useful to the reader for a more thorough understanding.

In most magnetic circuits a majority of the flux density from the permanent magnets does not contribute to the field within the small area of interest. The flux spreads through all space and, therefore, much of the deliverable power is wasted. The solution to this problem is found using the electric circuit analogy. In electrical circuits, insulation or the use of compensating potentials constrains the electric current to the desired paths. The magnetic analog to insulation requires using superconductors with sufficiently high lower critical fields, which is impractical at room temperature conditions. However, magnetic compensating potentials have proven quite successful in circuits containing REPMs. The compensating

potentials in a magnetic circuit are referred to as cladding, and the following example illustrates how they work.

Figure 6.7 shows a basic magnetic circuit and its corresponding electric analog. The two magnetic poles are represented by batteries, and the flux paths through air by wires with resistors in the circuit. The discrepancy introduced by representing the magnetic flux by discreet paths does not affect the illustration of cladding. The area of interest in the magnetic circuit is the air gap directly between the two magnets. Obviously, much of the flux is lost to areas surrounding the direct path. In the electric analog, current can be prevented from flowing through the upper wires by the introduction of additional batteries, as shown in figure 6.8. Batteries with the appropriate EMF values will completely eliminate current through those branches. To suppress the magnetic flux, permanent magnets, analogous to batteries, with the appropriate shapes and field strengths surround the original structure. In order to determine the appropriate configuration for the cladding magnets, assume that the goal of flux suppression has been accomplished, and then work backwards.

Hypothetically, assume the total flux from the magnets flows only through the cross section of the structure and is given by the magnetic Ohm's law:

$$\Phi = \frac{F}{R_t} = -\frac{2L_m H_{Bc}}{(R_m + R_g)} = \frac{2L_m B_r}{(R_m + R_g)} \tag{6.26}$$

where L_m is the length of one magnet, B_r is the remanence, R_m and R_g the reluctances of the magnets and the gap respectively, and $_B H_c$ the coercivity, which approximately equals $-B_r$ for REPMs. To attain total flux
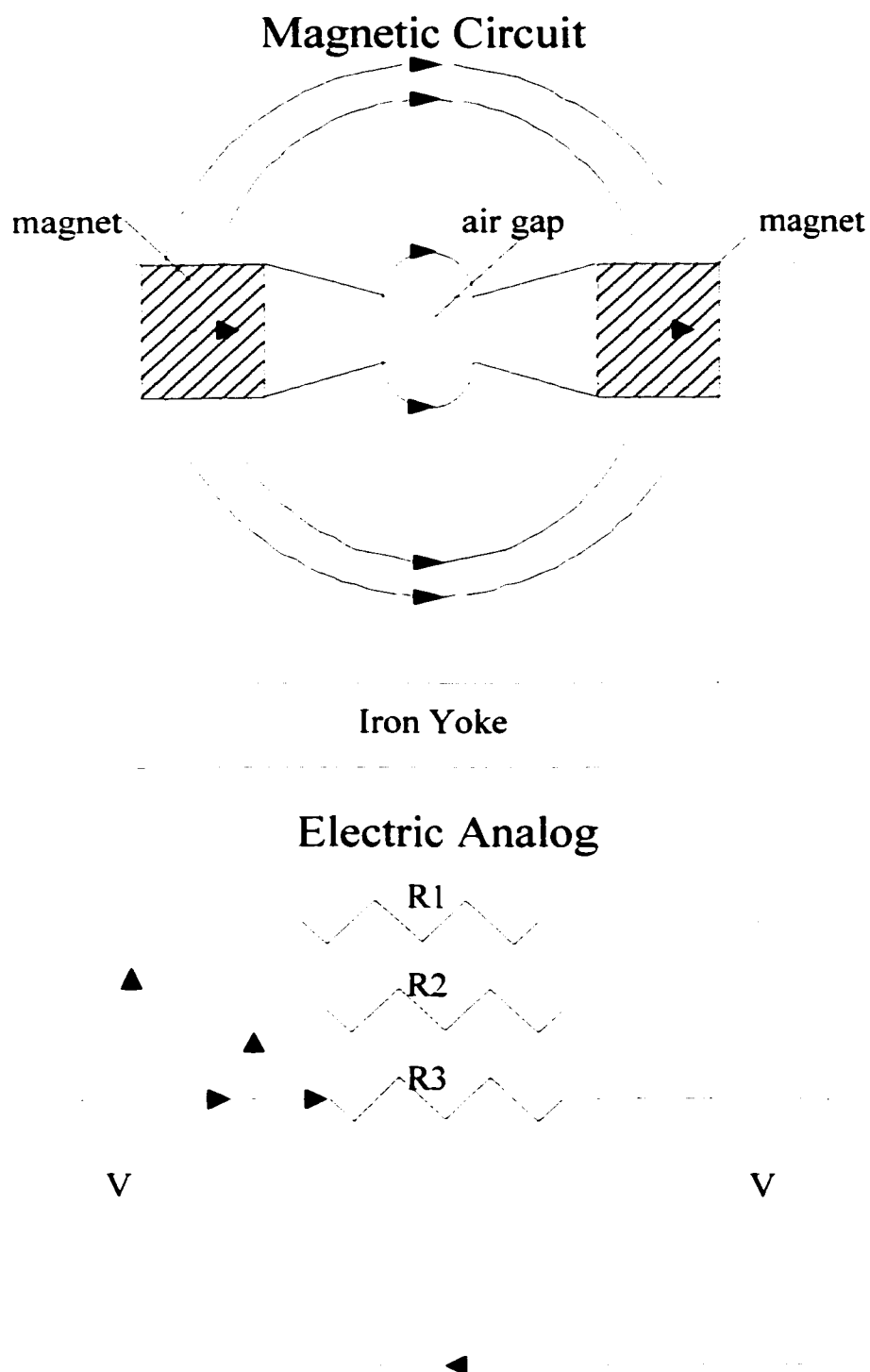
Magnetic Circuit

magnet   air gap   magnet

Iron Yoke

Electric Analog

R1

R2

R3

V   V

Figure 6.7 Basic, unclad magnetic circuit and its electric circuit analog.

Clad Magnetic Circuit

Cladding magnets

magnet

magnet

air gap

Iron Yoke
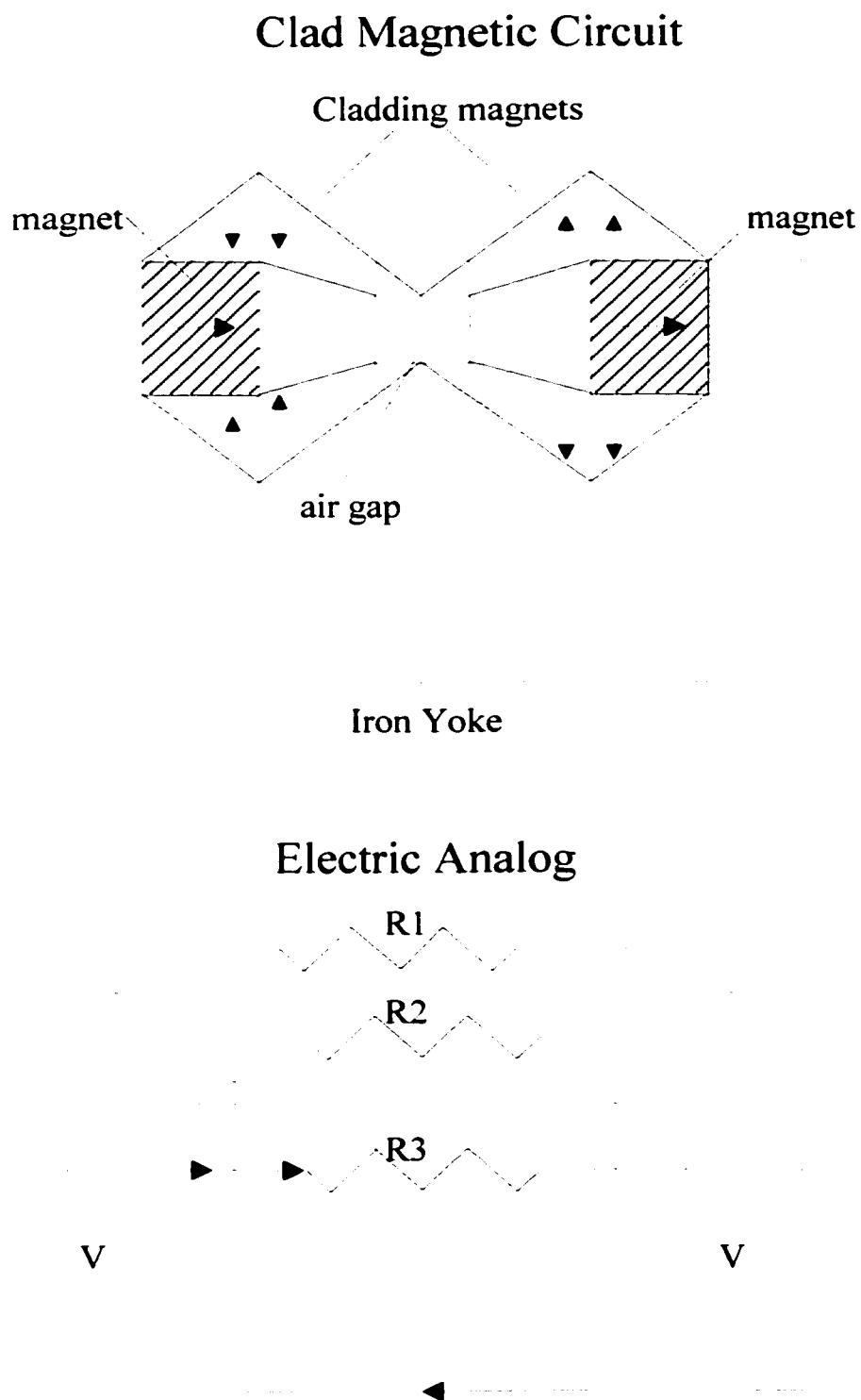
Electric Analog

R1

R2

R3

V

V

Figure 6.8 Clad magnetic circuit and its electric circuit analog.

confinement every point external to or on the surface of the magnet structure must have the same potential. The surface of the yoke connecting the magnets is an equipotential and thus fulfills the requirement. Cladding is only necessary around the magnets and the air gap such that all the external surfaces are at the same potential as the iron yoke. In other words, the potential difference between any point C on the surface of the cladding and any point A on the yoke must equal zero, regardless of the path connecting A and C. Consider path ABC shown in figure 6.9, a close up of the magnet structures shown in figures 6.7 and 6.8. If the potential difference between A and C equals zero then the MMF along the path must equal zero, giving:

$$F_{ABC} = F_{AB} + F_{BC} = 0 \qquad (6.27)$$

Given that:

$$F_{AB} = \frac{F_m x_B}{2L_m}$$

$$F_{BC} = H_d \cdot y_{BC} \qquad (6.28)$$

where F_m is twice the MMF across one of the magnets, H_d the radial magnetic field in the cladding, and y_{BC} the cladding thickness at point B, equation 6.27 becomes:

$$\frac{F_m x_B}{2L_m} + H_d \cdot y_{BC} = 0 \qquad (6.29)$$

From magnetic Ohm's law:

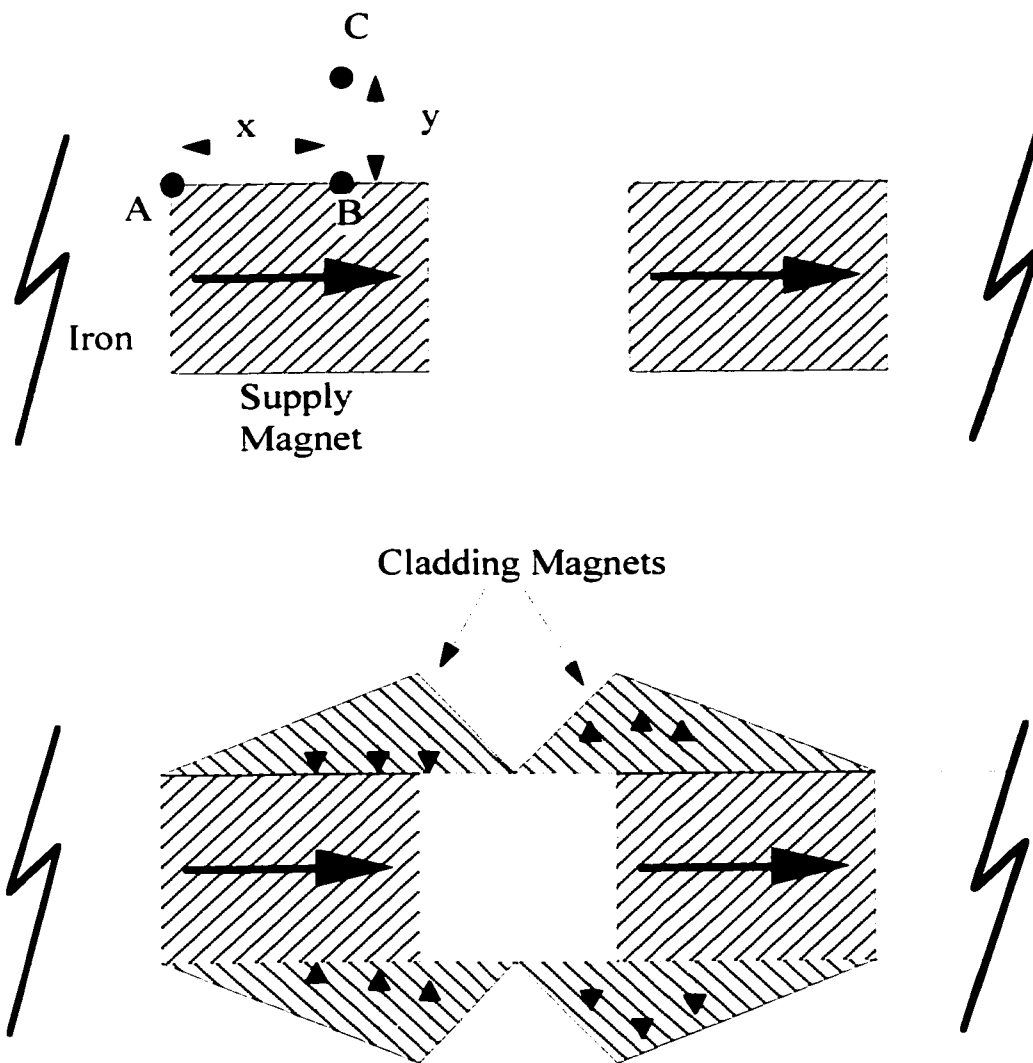$$F_m = \Phi \cdot R_m \qquad (6.30)$$

Figure 6.9 Close up of magnetic circuits shown in figure 6.7 (top) and figure 6.8 (bottom).

and substitution of equation 6.30 into equation 6.29 yields:

$$y_{BC} = \frac{F_{BC}}{H_d} = \frac{-F_{AB}}{H_d} = -\frac{\Phi R_m x_B}{2L_m H_d} \tag{6.31}$$

From the original assumption, no flux flows to the exterior, which implies that the radial flux density in the cladding must equal zero. For a REPM, which is magnetically rigid, the field equals the coercivity, $_BH_c = -B_r$, at zero flux density. Substituting equation 6.26 into equation 6.31 and using the fact that $H_d = {_B}H_c = -B_r$ yields:

$$y_{BC} = \frac{2L_m B_r R_m x_B}{2L_m H_{Bc}(R_m + R_g)} = \frac{R_m x_B}{(R_m + R_g)} \tag{6.32}$$

This relationship indicates that the surface of the cladding is a truncated cone with half angle $\arctan\left(\frac{R_m}{(R_m + R_g)}\right)$.

Figure 6.9 shows the cross sectional shape of the cladding magnets. The thickness y_{BC} reaches a maximum at the magnet's edge and declines beyond the edge since the field in the gap, H_g, is opposite that in the magnet, H_m. The potential decreases linearly with distance from the magnet end as:

$$\Delta F = -zH_g = zB_m = \frac{z\Phi}{A_m} \tag{6.33}$$

where A_m is the cross sectional area of the gap. Substituting equation 6.26 into equation 6.33 yields:

$$\Delta F = -\frac{2zL_m B_r}{A_m(R_m + R_g)} \tag{6.34}$$

At midgap the net MMF is zero so the cladding thickness is minimal. The potential becomes negative from the midgap to the far magnet, and cladding of opposite polarity compensates for it. The shape of the cladding is symmetric about the center of the air gap.

To further illustrate the effectiveness of cladding, consider the basic circuit in figure 6.7 versus the clad structure in figure 6.8. The gap field of the latter is ~2 T as compared with only 0.8 T for the basic, unclad circuit. To obtain a field of 1.6 T in an unclad configuration would require 55 kg of material versus only 7 kg of material in the clad configuration of figure 6.7 producing ~2 T. Such high fields usually require electromagnets many times larger with powerful current sources.

The magnetic structure designed to create the fields used in the current Penning trap is shown as a cross-section in figure 6.10. The magnet design consists of seven different magnet pieces and two iron discs; an arrow shows the direction of magnetization of each piece. The magnet pieces were manufactured and assembled by Magnet Sales and Manufacturing, a company in CA. This combination creates an enclosed cylindrical cavity with small entrance and exit apertures. The magnetization of the central tube magnet is along the axis of the cavity, and the other 6 magnet pieces create the cladding. The iron discs provide a return path for the field created by the central tube. Cladding discs outside the iron discs are magnetized to oppose and, therefore, to confine the central tube field. The two tapered, conical shaped cladding magnets surrounding the central tube further confine the field, and finally the rings surrounding the cladding discs oppose diagonal, corner fields leaking from the central tube field. The resultant magnetic field from the seven pieces, according to calculations, is homogeneous from endcap to endcap along the length of the cylinder, and has a strength of
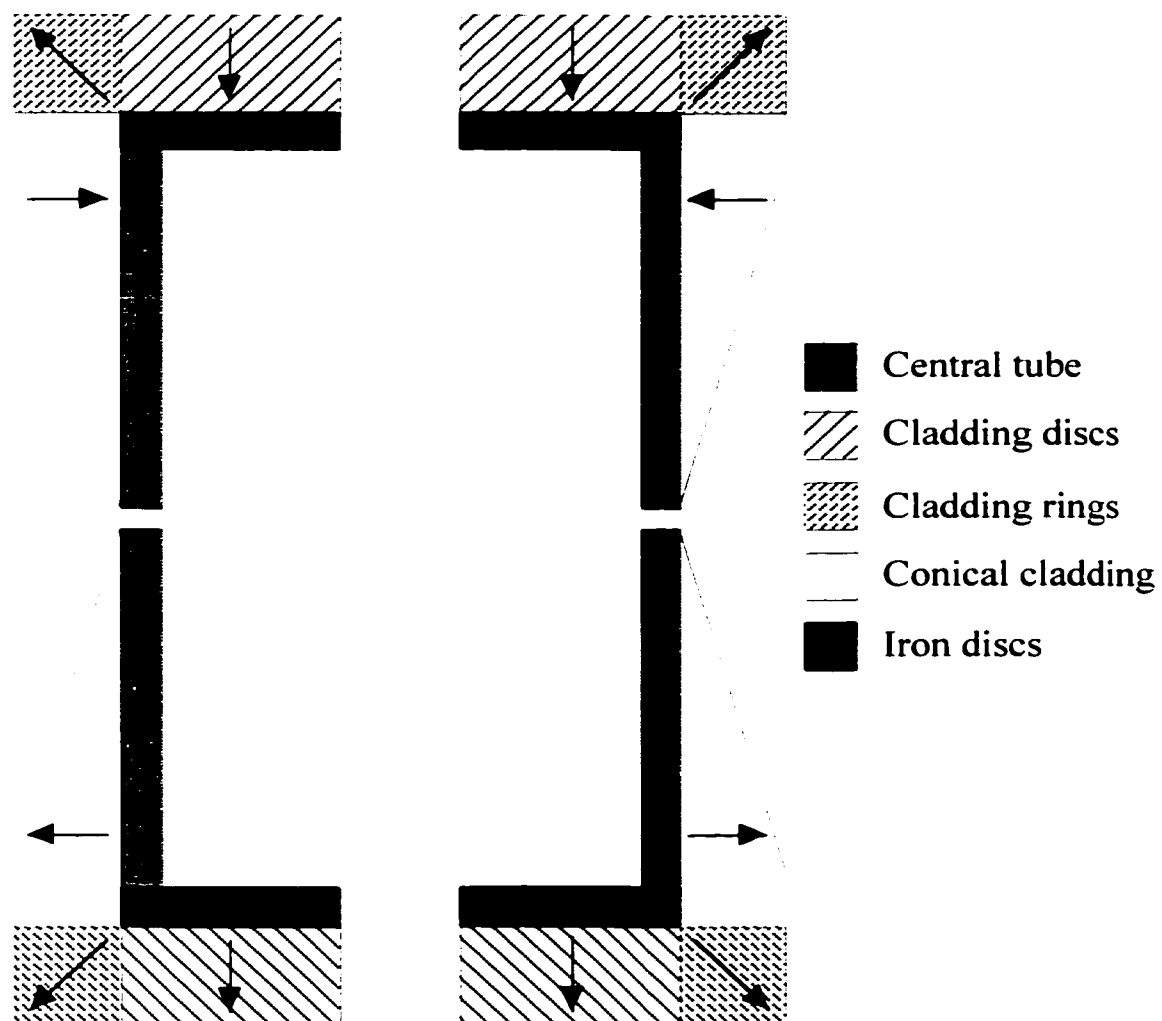
Figure 6.10 Cross section of magnet assembly.

~2.6 kG. Further, the magnetic field outside the magnetic structure drops to near zero within ~1 cm of the endcaps.

The repulsive magnetic force on the cladding magnets requires an external support structure surrounding the assembly. Mechanical force supplied by several screws on each end of the aluminum support structure keeps the cladding magnets in contact with the central tube magnet. It is extremely important that future students working with this assembly respect the repulsive forces present. Calculations suggest that there is > 90 lbs of force repelling each of the two cladding end discs. The actual repelling force may be twice as large according to measurements made by Magnet Sales and Manufacturing during the assembly process. Should it ever be necessary to disassemble the structure (i.e. to access the electrode structure which is placed inside the magnet assembly) the entire assembly should be returned to Magnet Sales and Manufacturing. Figure 6.11 shows a full assembly drawing of the Penning trap incorporating the electrode structure, the magnet structure, and the support structure in addition to the μ-metal shield external to all else.

6.8 Experimental Possibilities

Initial experiments will involve testing the parameter space of the Penning trap. Either potassium Rydberg core ions or SF_6^- could be trapped, and the possible range of trapping voltages and trapping times could be explored. The current background pressure in the chamber may limit the trapping time due to collisions between background gas and the trapped ion. Efforts to decrease the background pressure may be necessary to perform experiments with long trapping times. After determining the parameter
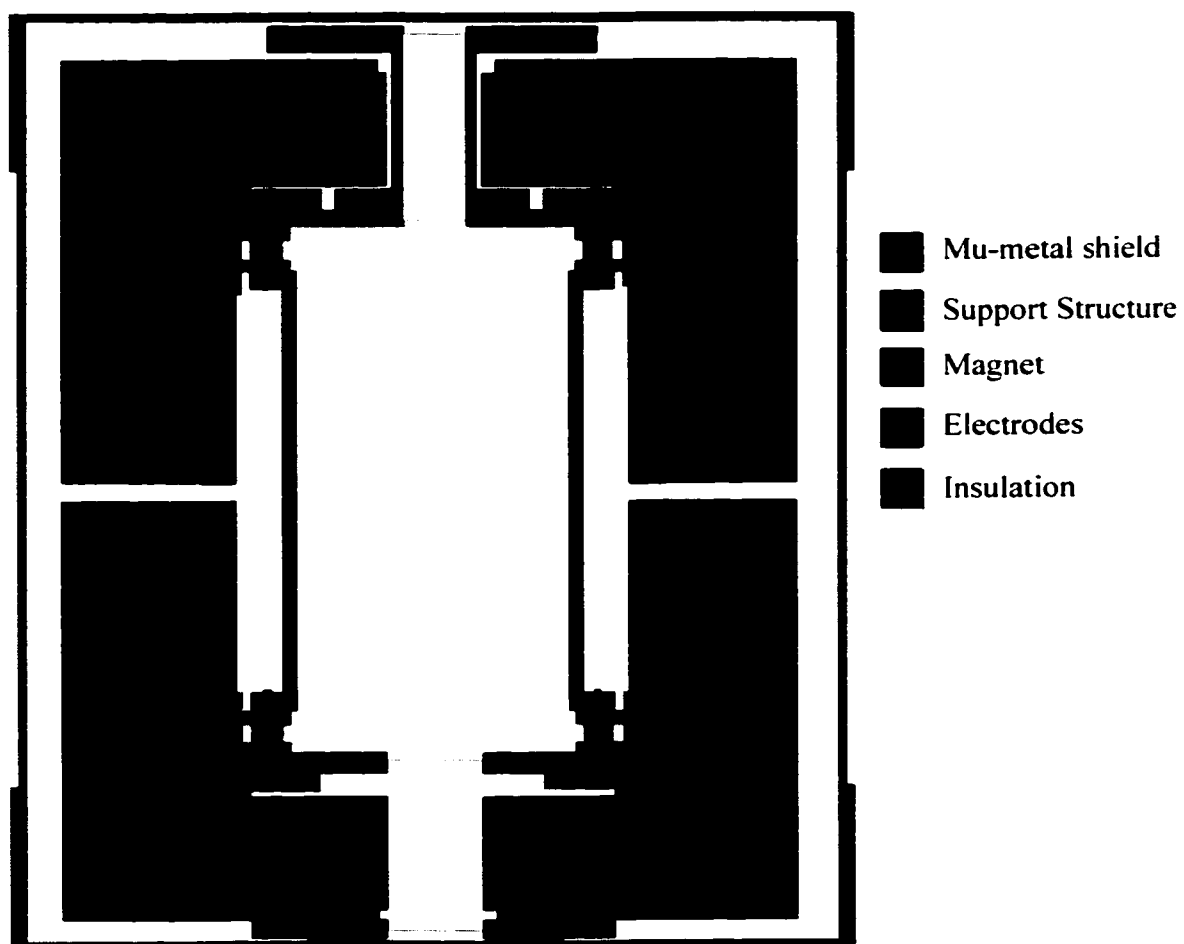
Figure 6.11 Cross section of entire Penning trap assembly.

space, basic experiments determining the lifetimes of long-lived negative ions can be performed using for example, as mentioned previously, SF_6^-, which is known to have a lifetime of a few ms, or the metastable $C_7F_{14}^-$ ions observed here with lifetimes $\gtrsim 100$ μs.

Other possible studies involve the trapping of dipole bound negative ions. As described previously, a dipole bound negative ion forms when a target molecule with a large dipole moment, $\gtrsim 2$ Debye, attaches an electron in a diffuse orbital about the molecule's more positive end. A theory has been proposed that dipole binding is a "doorway" state leading to stable negative ion formation after some lifetime. [47] There is, however, no experimental confirmation of this theory. Using the Penning trap in combination with a region of the TOFMS producing extremely high fields, ~ 10 kV cm^{-1}, it may be possible to determine the amount of time necessary for stabilization to occur. Dipole bound states can be distinguished from stable negative ion states because it is possible to strip the electron from a dipole bound state through application of a large field. Thus, by trapping a dipole bound negative ion and then expelling it from the trap into the high field region, it is possible to determine whether the ion expelled remains in a dipole bound state of if it has stabilized. By trapping for a range of times it could be determined when stabilization occurs, if at all.

Chapter 7
Conclusion

Molecules with a high electron affinity readily attach low-energy free electrons, and such molecules have become of great interest in environmental, biological, and chemical studies. Electron attachment to target molecules occurs via formation of negative ion resonance states (NIRS). The resulting intermediate ion formed by electron attachment can subsequently undergo a variety of processes, depending on the characteristics of the target molecule. There are many experimental methods available to study electron attachment processes, but few are applicable for thermal energy electron attachment. Methods using free electrons, such as crossed-beam experiments and FALP experiments, can rarely achieve the precision necessary to produce monoenergetic thermal energy electron-target collisions. However, as shown in this work, using Rydberg atoms as a source of essentially-free low energy electrons provides a novel and powerful method for studying such attachment processes.

The unique properties of Rydberg atoms make them useful tools. The large separation of the core ion from the Rydberg electron allows the Rydberg atom to be viewed as two independent scatterers in collisions with target molecules. The low binding energy of the Rydberg electron makes it appear as a very low energy, essentially-free electron. Further, the long radiative lifetime of Rydberg atoms provide stability for longer experimental studies.

The target molecules studied here represent a number of the possible post-electron attachment processes. $CBrCl_3$ attaches an electron to form an

intermediate ion that dissociates into a neutral and an anion. Both Br^- and Cl^- are observed as products of the reaction between potassium Rydberg atoms and $CBrCl_3$. Br^- is produced via two separate reaction channels. The intermediate ion in one case is long lived with a lifetime of ~ 5 ps, allowing complete redistribution of the excess energy of reaction into internal motions of the molecule. The other reaction channel has a short-lived intermediate, which implies that most of the excess energy of reaction appears in translation of the product ion. Cl^- appears to be produced via a single reaction channel, but whether the associated intermediate ion dissociates immediately or after a few vibrational periods is unclear. Complete redistribution of the energy does not occur, but some redistribution is possible. For thermal energy collisions the ratio of Br^- to Cl^- is 3 to 1, but previous studies suggest that the product ratio will change as the internal energy of the parent molecule is increased.

Non-dissociative electron attachment occurs for C_7F_{14} and C_6F_6. The products observed in $K(20p)/C_7F_{14}$ collisions are free electrons and $C_7F_{14}^-$ ions. The free electron signal results from an autodetachment process in which a short-lived $C_7F_{14}^{-*}$ intermediate ion expels the attached electron after ≤15 ps. Another process, Intramolecular Vibrational Relaxation (IVR), competes with the process of autodetachment to form the long-lived $C_7F_{14}^-$ ions. In IVR the excess energy of reaction is redistributed among inactive vibrational modes of the molecule, thereby stabilizing the $C_7F_{14}^-$ anion on the time scale of the experiment. The observed $C_7F_{14}^-$ signal has a lifetime of > 100 μs. $K(20p)/C_6F_6$ collisions also produce free electrons in addition to $C_6F_6^-$ ions. Studies show that the $C_6F_6^{-*}$ intermediate ions have a range of lifetimes against autodetachment. Most of the $C_6F_6^{-*}$ intermediate ions decay

within a few μs of formation, but the range of lifetimes extends to > 50 μs. Again, autodetachment explains the free electron signal, and IVR explains the $C_6F_6^-$ ions that are stable on the time scale of the experiment.

The Rydberg atom technique of studying thermal and subthermal energy electron attachment processes has been shown to be powerful and effective. Information about the energetics and the intermediate ion lifetimes of a wide variety of processes was obtained. The future work in this area should continue to be exciting and useful with the addition of the heated interaction region and the Penning trap.

References

1] J.D. Skalny, S. Matejicik, A. Kiendler, A. Stamatovic, T.D. Mark, *Chem. Phys. Letters*, vol. 255, p. 112, 1996.

2] G. Bakale, R.D. McCreary, *Mutagenesis*, vol. 7, no. 2, p. 91, 1992.

3] J.J. Kaufman, W.S. Koski, S. Roszak, K. Balasubramanian, *Chem. Phys.*, vol. 204, p. 233, 1996

4] A.R. Goushcha, A. R. Holzwarth, V.N. Kharkyanen, *Phys. Rev. E.*, vol. 59, n. 3, p. 3444, 1999.

5] Ding, 25th annitversary IEEE Conference Record, IEEE, NY, 1998, p. 309

6] L.A. Pinnaduwage, M.V. Buchanan, G.B. Hurst, "Novel Analytical Techniques Based on an Enhanced Electron Attachment Process," http://www.osti.gov/em52/1998posters/id55328/poster174.htm

7] L.G. Christophorou, D.L. McCorkle, A.A. Christodoulides, *Electron Attachment Processes*, Electron-Molecule Interactions and their Applications, vol. 1, Academic Press, 1984, p. 477.

8] L.G. Christophorou, *Adv. Electronics Electron Phys.*, vol. 46, p. 55, 1978.

9] J.B. Hasted, Physics of Atomic Collisions, American Elsevier Publishing Company, Inc., New York, 1972, p.112.

10] D. Smith, P. Spanel, *Swarm Techniques*, Atomic, Molecular, and Optical Physics: Charged Particles, vol. 29A, ed. F.B. Dunning, R.G. Hulet, Academic Press, 1995, p.273.

11] D. Smith, P. Spanel, *Studies of Electron Attachment at Thermal Energies using the Flowing Afterglow-Langmuir Probe Technique*, Advances in Atomic, Molecular, and Optical Physics, vol. 32, Academic Press, 1994, p. 307.

12] T.F. Johnston, Jr., *Tunable Dye Lasers*, Encyclopedia of Physical Science and Technology, vol. 14, p. 96,1987.

13] L.I. Schiff, Quantum Mechanics, McGraw-Hill Publishing Co., New York, 1968, p.92.

14] R.A. Popple, <u>Determination of Transient Negative Ion Lifetimes Using Rydberg Atoms</u>, Ph.D. dissertation, Rice University, Houston, TX, 1996.

15] A.H. Alajajian, M.T. Bernius, A. Chutjian, *J. Phys. B*, vol. 21, p. 4021, 1988.

16] E.P. Grimsrud, S.H. Kim, *Anal. Chem*, vol. 51, p. 537, 1979.

17] P. Spanel, D.Smith, S. Matejcik, A. Kiendler, T.D. Mark, *Int. J. Mass Spectrom. Ion Processes*, vol. 167/168, p.1, 1997.

18] T. Sunagawa, H. Shimamori, *J. Chem. Phys.*, vol. 107, p. 7876, 1997.

19] N.G. Adams, D. Smith, C.R. Herd, *Int. J. Mass Spectrom. Ion Processes*, vol. 84, p. 243, 1988.

20] R.O. Jones, O. Gunnarsson, *Rev. of Mod. Phys.*, vol. 61, no. 3, p. 689, 1989.

21] R.S. Mulliken, *J. Chem. Phys.*, vol. 23, no. 12, p. 2343, 1955.

22] C.E. Klots, *J. Chem. Phys.*, vol. 41, p. 117, 1964; *J. Chem. Phys.*, vol. 75, p. 1526, 1971; *Z. Naturforsch A*, vol. 27, p. 553, 1972.

23] P.J. Robinson, K.A. Holbrook, <u>Unimolecular Reactions</u>, Wiley, New York, 1972.

24] C.D. Finch, R. Parthasarathy, H.C. Akpati, P. Nordlander, F.B. Dunning, *J. Chem. Phys.*, vol. 106, p. 9594, 1997.

25] R.A. Popple, C.D. Finch, K.A. Smith, F.B. Dunning, *J. Chem. Phys.*, vol. 104, p. 8485, 1996.

26] P. Spanel, D. Smith, S. Matejcik, A.Kiendler, T.D. Mark, *Int. J. Mass Spectrom. Ion Processes*, vol. 167/168, p. 1, 1997.

27] F.J. Davis, R.N. Compton, D.R. Nelson, *J. Chem. Phys.*, vol. 59, no. 5, p. 2324, 1973

28] F.G. Kellert, K.A. Smith, R.D. Rundel, et al., *J. Chem. Phys.*, vol. 72, p. 3179,1980.

29] C.W. Walter et al., *J. Chem. Phys.*, vol. 91, p. 4284, 1987.

30] N.V. Lifanova et al., *Russ. J. Phys. Chem.*, vol. 66, p. 125, 1992.

31] R.A. Popple et al., *Phys. Rev. A.*, vol. 45, p. 247, 1992. plus references therein

32] M. Thoss, W. Domcke, *J. Chem. Phys.*, vol. 109, no. 16, p. 6577, 1998.

33] F.M. Penning, *Physica (Utrecht)*, vol. 3, p. 873, 1936.

34] K. Hubner, H. Klein, C. Lichtenberg, G. Marx, G. Werth, *Europhysics Letters*, vol. 37, no. 7, p. 459, 1997 and references therein.

35] L.S. Brown, G. Gabrielse, *Reviews of Modern Physics*, vol. 58, no. 1, p.233, 1986.

36] M. Kretzschmar, *Physica Scipta*, vol. 46, p. 544, 1992.

37] G. Li, G. Werth, *Int. J. Mass Spectrom. Ion Processes*, vol. 121, p. 65, 1992.

38] D.J. Wineland et al., *Adv. Atom. Mol. Physics*, vol. 19, p. 135, 1983.

39] P.K. Ghosh, Ion Traps, Clarendon Press, Oxford, 1995.

40] J.Tan, G. Gabrielse, *Phys. Rev. A48*, p. 3105, 1993.

41] J.M.D. Coey, ed., Rare Earth Iron Permanent Magnets, Clarendon Press, Oxford, 1996.

42] A.F. Kip, fundamentals of electricity and magnetism, McGraw-Hill, New York, 1969.

43] P. Campbell, Permanent Magnet Materials and Their Application, Cambridge University Press, Cambridge, 1994.

44] M. McCaig, Permanent Magnets in Theory and Practice, Halsted Press. John Wiley & Sons, NY, 1977.

45] Magnet Sales & Manufacturing publication about magnet properties.

46] H.A. Leupold, E. Potenziani II, A Permanent Magnet Circuit Design Primer, Army Research Laboratory, ARL-TR-946, July 1996.

47] P. Mikulski, Th. Klahn, P. Krebs, *Phys. Rev. A*, vol. 55, no. 1, p. 369, 1997.